MODELING LUNG STRUCTURE IN RODENTS

MODELING LUNG STRUCTURE IN RODENTS

By
WILLIAM B. COUNTER, M.Sc.

A Thesis
Submitted to the School of Graduate Studies
In Partial Fulfillment of the Requirements
for the Degree
Doctor of Philosophy

McMaster University

DOCTOR OF PHILOSOPHY (2012) McMASTER UNIVERSITY
(Medical Physics) Hamilton, Ontario

TITLE:	Modeling Lung Structure in Rodents
AUTHOR:	William B. Counter, M.Sc.
SUPERVISOR:	Dr. N. Renee Labiris
COMMITTEE MEMBERS:	Dr. Troy Farncombe Dr. Mike Noseworthy Dr. Mark Inman
NUMBER OF PAGES:	xii, 153

Abstract:

Pre-clinical imaging has provided pulmonary researchers with a number of valuable tools for studying both the lung and lung disease. A greater understanding of the structure/function relationships within the rodent lung would help to bridge the gap between functional images of the lung and its underlying anatomy.

The objectives of this work were to visualize and measure the components of rodent lung anatomy. Contrast-enhanced microCT images were used to visualize the airways and major blood vessels from both the Sprague-Dawley rat and the BALB/c mouse. These observations and measurements were used in the development of a pulmonary lung model containing both the conducting airways and blood vessels. The model can be applied to unenhanced images of the rodent lung to facilitate the regionalization of functional imaging data (SPECT/PET). The model has been used to simulate bronchoconstriction and deposition patterns of inhaled particles. Extensive validation revealed that the model was unable to fully reproduce the rodent lung and that further refinement is necessary.

The finer structure of the rodent lung, which could not be resolved using our microCT system, was measured using histological sections of the rodent lung. Software was developed and validated to automatically quantify the increases in airspace size that are associated with several respiratory conditions.

Together, this work sheds light on the underlying anatomy of the rodent lung that is present in both anatomical and functional images. The knowledge will help researchers to understand some of the structural changes that are occurring with the development of lung disease.

Acknowledgments:

I would first like to thank my supervisor Dr. Renee Labiris for all of the invaluable guidance over the course of this project. I would like to thank my committee members, Dr. Troy Farncombe, Dr. Mark Inman, and Dr. Mike Noseworthy for all their helpful insight along the way. Thanks to Dr. Luke Janssen for his insights into airway constriction and smooth muscle deposition. I'd like to thank Iris Wang for all her help with the animal work. I would also like to thank Rod Rhem, who provided invaluable support using MatLab, without which I would still be lost between vast lines of computer code. I would like to thank Chantal Saab and the McMaster Centre for Pre-Clinical and Translational Imaging (MCPTI) for the acquisition of all imaging data and for answering my many questions regarding the devices being used. I would also like to thank my fellow lab members, Brain Jobse, Kristi Lindsay, and Cory McCurry, for all their help in and outside the lab. I would like to thank everyone in the nuclear medicine department at the McMaster University Medical Centre for the continued support and lively Christmas parties. Thank you to Dr. Tom Farrell and all the medical physics office staff for keeping me somewhat on track during stressful times. Lastly, I would like to thank the Firestone Institute for Respiratory Health (FIRH) for financial support and for providing a forum to present and discuss my work.

Table of Contents

List of Figures

List of Tables

List of Abbreviations

APD	avalanche photodiode
BGO	bismuth germanate
CFD	computational fluid dynamics
CMOS	complimentary metal oxide semiconductor
CsI	cesium iodide
CT	computed tomography
CZT	cadmium zinc telluride
ERV	expiratory reserve volume
ET	emission tomography
FDG	fluorodeoxyglucose
FEV	forced expiratory volume
FEV_1	forced expiratory volume in 1 second
FOV	field of view
FRC	functional residual capacity
FWHM	full-width at half-maximum
GSO	gadolinium oxyorthosilicate
HRCT	high-resolution computed tomography
IC	inspiratory capacity
IRC	inspiratory reserve capacity
LSO	lutetium oxyorthosilicate
MAA	macro aggregated albumin
MDCT	multi-detector computed tomography
MIP	maximum intensity projection
MR	magnetic resonance
MRI	magnetic resonance imaging
NaI	sodium iodide
PAH	pulmonary arterial hypertension

PET	positron emission tomography
PFOB	perfluorooctyl bromide
PMT	photomultiplier tube
PPE	porcine pancreatic elastase
SPECT	single photon emission computed tomography
RV	residual volume
TGF	transforming growth factor
TLC	total lung capacity
TV	tidal volume
VC	vital capacity
VLA	volume of low attenuation
US	ultrasound
µCT	micro computed tomography
µSPECT	micro single photon emission computed tomography
µPET	micro positron emission tomography

1 Introduction

The central focus of this thesis is an investigation of the rodent lung and the ways that medical imaging technology can be used to investigate its structure and function. The thesis is being presented in a "sandwich" format and is built around three manuscripts which are submitted and under review. To provide context for the manuscripts, an introductory section is provided. It includes background information on both the human and rodent lung, medical imaging technology and its application to the lung, and techniques for lung image analysis and lung modeling.

The lung is one of the most essential organs in the human body because it provides the gas exchange required for complex life. Studying the lung often utilizes small animals to help researchers understand various aspects of structure, function, development, and disease. Medical imaging has provided several extremely valuable tools for investigating the lungs of small animals. This work focuses on imaging lung anatomy and using that knowledge to increase our understanding of how structure and function are related in the lung. A model of the rodent airways and pulmonary vasculature has been created to facilitate the analysis of both anatomical and functional images of the lung. Additionally, the model has been used to simulate the effects of different parameters (particle size, flow rate, etc.) on both the deposition of inhaled particles and the resulting airway constriction patterns. The finer elements of rodent lung anatomy were measured using histological techniques and an automated method was developed and validated to quantify these images.

As mentioned, chapters 2, 3, and 5 are in manuscript form. In the first paper (Chapter 2), the pulmonary airways and vasculature of two rodent species are visualized and measured using contrast-enhanced micro-CT. In the second paper (Chapter 3), a model of the rodent lung has been developed for image analysis and the simulation of certain respiratory diseases. Chapter 4 details an extended validation of the mathematical rodent lung model. In the third paper (Chapter 5), a method for quantifying airspace enlargement in histological lung sections has been developed. Following the 3 main manuscripts is an additional chapter (Chapter 6) focusing on the use of the model to simulate particle deposition and bronchoconstriction.

1.1 Pulmonary Physiology

1.1.1 Lung Anatomy

The primary role of the lungs is gas exchange; carbon dioxide, a metabolic waste product, is exchanged for the atmospheric oxygen required for many biological processes occurring in the body. The lung is essentially comprised of two major components: airways and blood vessels, and in general, both components direct gases towards and away from the sites of gas exchange. These gas exchange centres, known as alveoli, are the functional units of the lung and are surrounded by a vast network of capillaries. Oxygen in the inspired air diffuses across the alveolar surface into the blood while carbon dioxide diffuses in the opposite direction, from blood to alveoli, where it is then expired [1].

The structure of the lung represents an evolutionary development which attempts to maximize the alveolar surface area within a finite volume, therefore maximizing the potential for gas exchange. The idea is analogous to the way a tree maximizes its potential for photosynthesis by maximizing the total surface area of its leaves. Utilizing successive branching, the concept, known mathematically as fractal geometry, is characterized by self-similarity at different levels of scale [2-5]. Consider, for example, the way the branch of a tree resembles a scaled-down version of the tree itself. Mathematically, however, the branching process can continue indefinitely, while in nature the process only continues down to some limiting functional unit (leaves for a tree, alveoli for a lung). This branching pattern in the airways of the lung allows a single main airway, the trachea, to eventually divide into millions of alveoli, maximizing the potential for gas exchange. The pulmonary blood vessels, like all blood vessels in the body, also exhibit fractal-like properties which maximize the surface area available for gas exchange [5-7].

The airways in the human lung branch approximately 23 times before reaching the alveoli. The concept of generation, introduced by Weibel in 1963 [8], is commonly used to characterize hierarchy in the airway branching pattern. Starting from the trachea, assigned a generation of zero, generation is increased by one at each branch point, or bifurcation. Gas exchange begins to occur after about the 16^{th} generation [1]. Airways above this are known as conducting airways and include the trachea, bronchi, bronchioles, and terminal bronchioles. Airways below generation 16 are known as transitional and respiratory airways and include respiratory bronchioles, alveolar ducts and alveolar sacs.

The components of airway structure vary considerably from the trachea to the alveoli [1]. The larger airways are surrounded by cartilage for support; by the time the bronchioles are reached cartilage is no longer present. The trachea is surrounded by C-shaped rings of cartilage but as the bronchi enter the lung, the cartilage rings are replaced by irregularly shaped cartilage plates which become less prevalent as the airways get smaller. A layer of smooth muscle surrounding the airways becomes more prevalent as one approaches the terminal bronchioles; this layer then becomes thinner again as one transitions from the terminal bronchioles to the alveoli [1]. Although not completely understood, the presence of smooth muscle helps regulate airway tone and may be a defense mechanism against foreign particles [9]. The conducting airways are lined with ciliated cells interspersed with mucus-secreting goblet cells and other secretory cells [1]. These cells constitute an important defense mechanism for the lungs. Foreign particles are trapped in the excreted mucus and pushed upwards towards the trachea and pharynx via the oscillatory movement of cilia [10].

As the pulmonary airways transport air to the sites of gas exchange, the pulmonary vasculature supplies blood. Unlike the airways however, which use the same structure to move gas towards and away from the alveoli, the pulmonary vasculature is divided into two distinct components: deoxygenated blood is transported to the gas exchange centres by the pulmonary arteries and the oxygenated blood is transported away by the pulmonary veins. This represents a major difference between the pulmonary airways and vasculature. Air moves in both directions through the airways, while blood only moves in a single direction through the vasculature. Deoxygenated blood is returned from systemic use to the heart, where it is pumped into the lung via the right ventricle and pulmonary arteries [11]. Following oxygenation, the blood is returned to the left atrium of the heart via the pulmonary veins; oxygenated blood is then pumped systemically via the left ventricle. The branching structure of the pulmonary arteries and veins are similar to that of the airways [12]. The two vascular trees are connected by a vast network of capillaries where gas exchange occurs. Additional blood vessels, known as supernumerary vessels, branch off the larger vessels to supply the lung tissue with oxygen. Blood vessels in the lung have been categorized for both the human [12] and the rat [13] lung using the ordering system used by Horsfield. In this ordering system, the smallest, most terminal segments are assigned an order of 1 and parent segments are assigned an order 1 greater than the highest ordered daughter [14]. These blood vessels, known collectively as the pulmonary circulation, carry blood towards and away from the sides of gas exchange and supply the lung parenchyma; the airways are supplied with oxygenated blood via the bronchial circulation [15]. The bronchial circulation is considered part of the systemic circulation; bronchial arteries branch off the aorta to supply the airways before draining primarily back into the pulmonary arteries [15].

The lung is also divided into several distinct compartments known as lobes. The human lung consists of five lobes: two on the left and three on the right. In many species of quadrupeds, including rodents, the lobes of the lung are organized in a slightly different configuration. In most species of rodents, the lung is comprised of a single lobe on the left and 4 lobes on the right [16]. The four lobes comprising the right lung are commonly referred to as the cranial, middle, caudal, and accessory lobe [11]. The lobes of the Sprague-Dawley rat are illustrated in Figure 1.1.1.

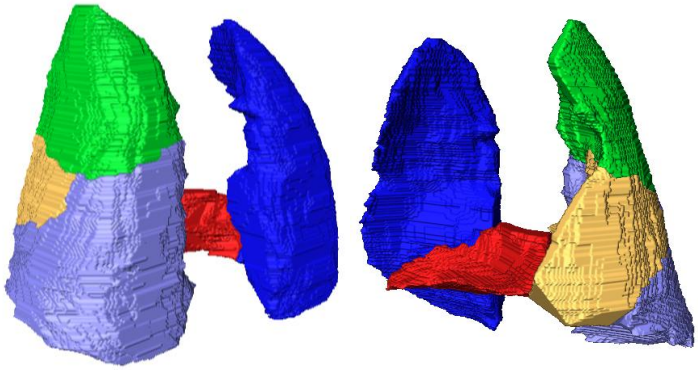

Figure 1.1.1: Lobes of the rat lung (Sprague-Dawley). Left lobe (blue), Cranial lobe (green), Middle lobe (yellow), Caudle lobe (mauve), Accessory lobe (red).

1.1.2 Lung Function

Air, like other gases, moves from areas of high pressure to areas of lower pressure. In order to move air into and out of the lungs, there must be a difference between the atmospheric pressure at the mouth and the alveolar pressure. Under normal conditions, air is moved into the lung by creating alveolar pressures beneath that of the atmospheric pressure [1]. This pressure gradient is created using the respiratory muscles: the diaphragm and intercostals muscles. As these muscles contract, the diaphragm drops and the chest wall expands, increasing the thoracic volume and distending the alveoli. The resulting increase in alveolar volume causes a drop in alveolar pressure, dropping it below atmospheric pressure. In order for air to flow into the lung, this pressure gradient must be great enough to overcome the impedance of the lung. Two factors contribute to this impedance: resistance and elastance. Resistance is caused by the frictional force of air moving through the airways. Elastance is caused by a restoring force within the alveolar walls. A simple analogy involves the inflation of a balloon through a straw. In order to inflate the balloon, the pressure gradient caused by blowing must overcome both the frictional force of the air traveling through the straw (resistance) and the tendency of the balloon to resist being stretched (elastance). Exhalation proceeds in a similar fashion, although it is passive under normal resting conditions. As the respiratory muscles relax,

alveolar pressure is raised above atmospheric pressure. The elastance of the lung, instead of impeding airflow as in inhalation, creates this gradient and drives air out of the lung. The pressure gradient must be great enough to overcome the resistance of the air traveling through the airways. Under exercise conditions and during forced exhalations, the internal intercostal and abdominal muscles are contracted to reduce the volume of the chest, increasing the pressure gradient even further [1].

The total lung volume, or total lung capacity (TLC), is about 6 L for an average adult human (~70 kg) and can be divided into four standard lung volumes [1]. They are known as tidal volume, residual volume, expiratory reserve volume, and inspiratory reserve volume (Figure 1.1.2).

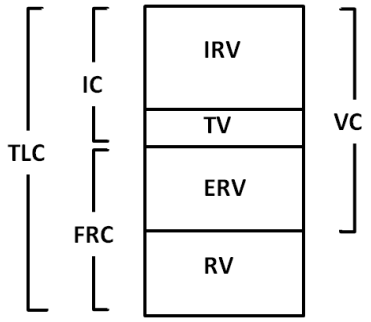

Figure 1.1.2: Lung volumes and capacities [1].

The tidal volume (TV) is the volume of air that is breathed in and out during normal, quiet breathing. It is typically about 0.5 L for a healthy 70 kg standing adult [1]. The residual volume is the volume of air remaining in the lungs following maximal exhalation (typically about 1.5 L). The expiratory reserve volume (ERV) is the maximum volume of gas that can be forcibly expelled from the lung following a normal exhalation (about 1.5 L). The inspiratory reserve volume (IRV) is the maximum volume that can be inspired following a normal inhalation (about 2.5 L). The residual volume (RV) is the volume of air remaining in the lungs following a full exhalation. The inspiratory capacity (IC) is the sum of inspiratory reserve volume and the tidal volume. The functional residual capacity (FRC) is the sum of the expiratory reserve volume and the residual volume. The vital capacity (VC) is equal to the total lung capacity (TLC) minus the residual volume, essentially the volume of gas that can be moved in and out of the lungs.

Tolnai et al. determined the FRC, TLC, and RV of 14 week old Sprague-Dawley rats to be about 3, 19, and 1 ml, respectively [17]. Hantos et al. determined the RV and TLC of 33 g CBA/Ca mice to be 0.20±0.10 and 1.48±0.20 ml, respectively [18]. Lai-Fook et al. determined the FRC and TV of 20-24g BALB/c mice to be 0.58±0.20 and 0.33±0.06 ml, respectively [19].

Once the alveoli have been filled with inspired air, gas exchange can occur across the alveolar-capillary boundary. Gas exchange occurs passively by diffusion; gases flow from areas of high partial pressures to areas of low partial pressures. The partial pressure of oxygen (Po_2) in inspired air is about 159 mmHg (760 mmHg x 20.93%) [1]. Alveolar Po_2 is reduced to about 100 mmHg due to it being humidified and mixed with exhaled gases. The partial pressure of carbon dioxide (Pco_2) in the alveoli is about 40 mmHg. In the deoxygenated blood surrounding the alveoli, Po_2 and Pco_2 are about 40 mmHg and 45 mmHg, respectively. The pressure gradients between alveolar and pulmonary arterial blood for Po_2 and Pco_2 permit the diffusion of oxygen into the blood and the diffusion of carbon dioxide out of the blood. After passing through the capillary bed, Po_2 and Pco_2 are about 100 mmHg and 40 mmHg, respectively [1].

1.1.3 Lung Disease

There are many different diseases which affect the lungs ability to undergo gas exchange. Some diseases, like asthma and chronic bronchitis, cause a narrowing of the airways making it more difficult to move inspired air into the alveolar regions [1]. Other diseases, such as emphysema, characterized by a destruction of the alveoli, and pulmonary fibrosis, characterized by a stiffening of the lung tissue, can also decrease the efficiency of gas exchange [1]. These diseases represent a considerable health burden on human populations worldwide [20-22].

Asthma is characterized by a reversible narrowing of the airways and is treated using inhaled corticosteroids and bronchodilators [20,23]. Although not completely understood, the disease is believed to be related to the action of the smooth muscle layer surrounding the airways. Contraction of smooth muscle is usually preceded by inflammation within the lung, resulting in increased mucus production, and eventually remodeling of the airways, where the amount of smooth muscle surrounding the airway is increased [24]. Asthmatic patients often exhibit a hyper-responsiveness to the inhaled muscarinic receptor agonist Methacholine. Although constriction of the smooth muscle layer does occur in normal individuals following exposure to Methacholine, asthmatics have been shown to exhibit a greater deal of bronchoconstriction for a given concentration of agonist (hyper-reactivity) and also to exhibit bronchoconstriction at doses that would not cause bronchoconstriction in normal subjects (hyper-sensitivity) [25].

Chronic obstructive pulmonary disease (COPD) is a condition encountered mainly in patients with a history of cigarette smoke exposure [21]. The disease is characterized by both chronic bronchitis and emphysema. Bronchitis, or inflammation of the bronchi,

reduces the luminal diameter of the airways and makes it more difficult to move air into and out of the lungs [26]. Emphysema is a non-reversible breakdown of alveolar structure; its main effects are two-fold. Due to the break-down of their structure, emphysematous alveoli are larger than healthy alveoli, decreasing their surface area to volume ratios and resulting in a decreased potential for gas exchange [27,28]. In damaged alveoli, a smaller percentage of the gas that it contains is in contact with the alveolar wall where gas exchange occurs. The destruction of alveolar structure also makes the lung less elastic, making it harder to expel inhaled gases and resulting in air being trapped in the lung.

Pulmonary fibrosis results from the deposition of excessive amounts of fibrous connective tissue within the lung [22]. This deposition of collagen results in increased scar tissue within the lung and is often referred to as lung scaring. Pulmonary fibrosis can be idiopathic or result from injury to the lung tissue caused by infection or certain inhaled particles [29]. Fibrosis is usually preceded by inflammation, causing cells known as fibrocytes to migrate to the lung, eventually resulting in collagen deposition [30]. Fibrotic tissue is less compliant then healthy lung tissue, resulting in a stiffer lung and making it more difficult to move air into and out of the lung. The increased quantities of fibrotic tissue also increase the distance that gases need to traverse between the air and the blood. Patients with pulmonary fibrosis suffer from chronic and progressive exertional dyspnea and cough [31].

The effective treatment of these diseases is an ongoing challenge in pulmonary medicine. Understanding the underlying mechanisms of these diseases is critical to being able to treat them effectively in humans. Research utilizing small animals represents the first step towards this goal.

1.2 Medical Imaging

1.2.1 Computed Tomography (CT)

Computed tomography (CT) is an imaging methodology based on the attenuation of an x-ray beam through a subject. As in a conventional x-ray, denser materials such as bone stop a greater percentage of incoming photons than less dense materials such as soft tissue [32]. Detectors placed opposite the beam quantify the number of transmitted photons passing through the subject to produce anatomical images based on photon attenuation, approximately equivalent to tissue density [33]. In CT, the x-ray source and detectors are rotated around the subject yielding a set of 2-dimensional x-ray images, or

projections. In a process known as tomography, these 2D projections are back-projected to create a 3-dimensional image of tissue density within the subject [34]. Different tissues in the body have different photon attenuations [35] and thus CT provides an excellent tool to create maps of subject anatomy; it is therefore generally considered an anatomical imaging technique.

The x-ray beam is created by accelerating electrons into a metal target, typically made of Tungsten. The number of electrons hitting the target and the resulting x-ray fluence are dependent on tube current; the distribution of x-ray energies is dependent on the tube voltage [34]. Most x-ray detectors are composed of a scintillator crystal coupled to a photodiode [36]. Scintillators are materials that emit visible light following the absorption of a high energy photon such as an x-ray or γ-ray [37].

Image reconstruction is accomplished using techniques such as backprojection and filtered backprojection [33]. In backprojection, values from the projected data are traced back across the image matrix to obtain an approximation of the original object. Filtered backprojection attempts to reduce or eliminate the blurring inherent in normal backprojection using a deconvolution operation [33]. Iterative reconstruction algorithms can also be used to reconstruct projection data, but this method is computationally expensive and requires fast computer hardware [33]. A reconstructed CT image contains voxels which have values equal to the CT attenuation value at the equivalent position within the subject. Because CT attenuation values vary depending on scan parameters such as the voltage, the images must be standardized based on the attenuation values of air and water. Images are therefore converted to Hounsfield units (HU) where air is assigned a value of -1000 and water a value of 0 [38].

Clinical CT technology has improved considerably since its introduction in the 1970s [33]. CT scanners have evolved from single-slice axial systems, which acquire slices sequentially as the subject is moved stepwise through the gantry, to helical acquisitions, where the subject is moved continuously through the gantry [33]. The introduction of multi-detector CT systems has increased the amount of data collected, yielding higher image resolutions and reduced scan times [34]. These technological steps forward have also allowed larger portions of the human body to be imaged.

The spatial resolution of a CT system is dictated mainly by the size of its source, its detector resolution, and the system geometry; the reconstruction algorithm used can also affect resolution [33].

1.2.2 Single Photon Emission Computed Tomography (SPECT)

Single Photon Emission Computed Tomography (SPECT) is one of two types of emission tomography [39]. In emission tomography, a radioisotope is injected into a patient and its eventual localization inside the body is determined by detecting the gamma-rays emitted from its decay. SPECT utilizes gamma-emitting radioisotopes such as ^{99m}Technetium. Collimators placed in front of the detectors ensure that when a photon is detected, the approximate direction that it came from is known. These collimators block photons coming from all but a small range of directions; it is estimated that only about one in ten thousand photons penetrates the collimator [39]. The photons that do pass through the collimator are collected using detectors that are either rotated or positioned around the subject. The most common detector type is a scintillator crystal coupled to a photomultiplying device. Numerous types of scintillator crystals can be utilized in SPECT applications, each with its own advantages and disadvantages [40]. The most common scintillator crystal used in SPECT imaging is thallium-doped sodium iodide (NaI). Photomultiplier tubes (PMT), used in early SPECT systems, are now beginning to be replaced by smaller and more efficient solid state detectors such as avalanche photodiodes (APD) [37]. The main advantages of these detectors versus traditional PMTs are their compact size and insensitivity to magnetic fields [37]. Another possibility for photon detection involves the replacement of the combined scintillator and photon transducer with a semiconductor. These detectors provide a direct conversion of absorbed γ-ray energy into an electronic signal [37]. The most promising of these semiconductor detectors is cadmium zinc telluride (CZT).

Utilizing the collimated detection of emitted γ-rays and by collecting data from around a subject, a three-dimensional distribution of the radioisotope within the subject can be determined. Many molecules of biological interest can be tagged with a radioactive atom and hence can be tracked in the body [37]. SPECT therefore provides an excellent means of tracking biological processes in the body and is thus considered to be a functional imaging technique.

1.2.3 Positron Emission Tomography (PET)

Positron Emission Tomography (PET) represents the second type of emission tomography. As opposed to SPECT, which utilizes single-gamma emitting isotopes, PET utilizes positron emitting isotopes [41]. A positron, or anti-electron, is released following the decay of certain atoms such as ^{18}F and ^{11}C. The positron travels a small distance before interacting with an electron in what is known as an annihilation; a process where

the positron and electron are converted into two 511keV photons traveling away from the annihilation site in approximately opposite directions [42,43]. When two photons are detected in a small time window, they are considered to have originated from the same annihilation event and a line of response can be drawn between the two detectors. The annihilation event is then deemed to have occurred somewhere along that line. Surrounding a subject with detectors and measuring many lines of response allows the original deposition of the radioisotope to be determined. Because each detected annihilation event results in a line of response, no physical collimators are need. This gives PET a much higher sensitivity compared to SPECT, allowing smaller amounts of radioactivity to be detected [39].

PET utilizes instrumentation similar to that of SPECT. Both technologies involve the detection of γ-rays. The high photon energies (511keV) involved in PET require detectors with greater stopping power than what is required in SPECT applications; common scintillator crystals used in PET include bismuth germinate (BGO), gadolinium oxyorthosilicate (GSO), and lutetium oxyorthosilicate (LSO) [44]. Unlike SPECT, which can use a single array of detectors rotating around the subject, PET requires detectors to be positioned on opposite sides or, more commonly, in a ring surrounding the subject.

1.2.4 Magnetic Resonance Imaging (MRI)

Unlike CT, SPECT, and PET, Magnetic Resonance Imaging (MRI) does not utilize ionizing radiation. Instead it relies on the fact that certain atoms possess nuclear spin, resulting from unpaired nucleons in their nucleus [45]. In the presence of a magnetic field these spins align along the field and precess at different rates depending on their electronic environment [46]. Radio-frequency (RF) pulses are used to flip the spins away from the direction of the main magnetic field and an RF signal is received as the spins slowly realign with the main field. Various types of materials therefore produce different signals, allowing for the creation of an image. .[46]. Positional information is obtained using a set of gradient coils that create position-dependent magnetic fields. MRI is extremely versatile. Proton (^{1}H) MR is the most common due to is overwhelming presence within the body, but atoms such as ^{13}C and ^{23}Na also possess nuclear spin, permitting their utility in certain MR applications. Different anatomical imaging techniques are possible with MR (T1-, T2-, Proton-weighted) based on the scan parameters [47]. In addition, MR offers a range of functional imaging techniques making it one of the most versatile imaging techniques. The main strengths of MRI include its versatility, its excellent soft tissue contrast, and the absence of potentially harmful ionizing radiation.

1.2.5 Ultrasound (US)

High-frequency sound waves, known as ultrasound (US), can penetrate body tissues and hence be utilized as an imaging modality [48]. The sound waves are created by a transducer, which converts electrical energy into mechanical energy. The sound waves penetrate the tissue and as the wave transitions between different tissue types, small amounts of its energy are deflected back to the transducer [48]. The transducer transforms this reflected sound wave, or echo, back into an electronic signal which can be measured. Most diagnostic ultrasound units operate between 2 and 25 megahertz [49]. Higher frequency waves provide better resolution, but do not penetrate as deeply into the body as low frequency waves. Ultrasound is useful for imaging soft tissue, but is much less useful for imaging bone and air [49]. US waves are almost completely blocked by bone and, in order to eliminate the air gap between the transducer and subject, an acoustic coupling gel is applied to the subject.

A major advantage of ultrasonic imaging is that it permits real-time imaging of moving structures at 15-30 frames per second [48]. Additional strengths of this modality compared to others include its portability, it cost-effectiveness, and its relative safety [48].

Utilizing the Doppler Effect, ultrasounic waves can be used to examine blood flow within the body. Blood flowing towards the transducer causes the reflected wave to have an increased frequency while blood flowing away from the transducer causes the reflected wave to have a decreased frequency. The technique is particularly useful for imaging directional blood flow within the heart.

1.2.6 Pre-Clinical Imaging

Imaging of small animals is important not only for evaluating novel imaging methodologies, but also for answering a wide variety of research questions across a broad range of fields. The need to image small animals presents a unique problem in imaging because clinical technologies must be scaled down to provide an equivalent resolution for imaging of both anatomy [50] and function [51]. The large size difference between mice and men, for example, does not permit an adequate mouse image to be acquired on a system designed to image human subjects. The increased resolution required to adequately image small animals comes from a decreased source size, detectors with increased resolution and by decreasing the distances between source and detector [50]. Micro-CT (μCT), micro-SPECT (μSPECT), and micro-PET (μPET) therefore scale down the technology used in their clinical equivalents to allow high-resolution images of much

smaller subjects. As detector technology continues to improve and geometry is optimized, image resolution will continue to increase for CT [50,53], SPECT [51,53], and PET [41].

The McMaster centre for pre-clinical and translational imaging (MCPTI) has a hybrid µCT/µSPECT system (*X-SPECT, Gamma-Medica*) and a stand-alone µPET system (*MOSIAC PET, Philips*), both of which are pictured in figure 1.2.6.

Figure 1.2.6: Gamma-Medica X-SPECT/CT system (left), Philips Mosaic-PET system (right)

The µCT component utilizes a cesium iodide (CsI) scintillator coupled to a CMOS (complementary metal oxide semiconductor) photodiode. The µSPECT component utilizes a sodium iodide (NaI) scintillator couple to a photomultiplier tube (PMT). The SPECT system uses two detector arrays positioned on opposite sides of the subject. The µCT components of the scanner are positioned perpendicularly to the SPECT detectors. The µPET system uses a ring of gadolinium oxyorthosilicate (GSO) crystals coupled to PMTs, positioned in a ring around the subject. The µCT system has a resolution of approximately 50 µm. The µSPECT and µPET systems both have resolutions of approximately 2-3 mm. The hybrid nature of the µCT/µSPECT system allows both anatomical CT and functional SPECT images to be acquired without having to move the subject and facilitates image fusion, where functional images are overlaid onto anatomical images.

1.3 Pulmonary Imaging

1.3.1 Imaging Structure

The lungs present a particularly interesting case with regards to imaging; it is a unique structure in the body and presents its own set of imaging challenges. Despite its excellent soft tissue contrast and absence of ionizing radiation, conventional MRI has

failed to surpass CT in the realm of thoracic imaging [54]. The lung, a structure composed largely of air, does not create a great signal using conventional MR techniques and it is typical for the lung to appear as a dark signal-less void in most MR images [55]. Techniques utilizing specialized RF coils and hyperpolarized gases such as ^{3}He and ^{129}Xe have been used to visualize the pulmonary airways [56]. Pulmonary vascular structure can be investigated using both contrast-enhanced CT and contrast-enhanced MRI (discussed in section 1.3.3). Ultrasound is not commonly used for lung imaging due to difficulties caused by the large and sudden changes in tissue densities surrounding the lungs.

X-ray and CT remain the gold standard for anatomical lung imaging based on their ability to provide contrast within the lung and due to their greater availability over MRI. High-resolution CT (HRCT) scanners used in the clinical arena provide excellent images of lung anatomy and are fast enough to capture an image of the lung during a single breath-hold [57]. This largely eliminates the motion artifacts associated with thoracic imaging caused by both respiratory and cardiac motion. Montaudon et al. used CT to compare bronchial morphometry between smokers and non-smokers; they found significantly decreased luminal diameters in generation 4-10 airways in smokers [58]. Emphysema has also been quantified using CT; emphysematous regions of the lung showed decreases in density due to the presence of trapped air [57]. James Hogg and colleagues used microCT to study excised lungs from human subjects with and without COPD; they reported a 10-fold reduction in the number of terminal bronchioles and a 100-fold reduction in cross-sectional luminal area [59]. Sung et al. demonstrated that HRCT could be a valuable tool to use in the diagnosis and treatment of patients with pulmonary fibrosis [60]. Excessive deposition of fibrotic tissue results in increased densities within the lungs of thoracic CTs.

Pre-clinical lung imaging techniques to image lung anatomy in small animals continues to improve with increases in system resolutions [56]. In the pre-clinical arena, where breath holds are difficult to achieve, other methods must be employed to reduce motion artifacts. Gating, either respiratory, cardiac, or both, is possible by sorting projections into their appropriate stage in the respiratory or cardiac cycle. Gating can be done by monitoring external triggers such as breathing or heart rate or alternatively, can be applied after image acquisition by monitoring the position of the diaphragm (in the case of respiratory motion) within the projection images [61]. Respiratory gating has also been done in mice that are connected to a mechanical ventilator by utilizing computer-controlled breath holds [62].

Thiesse et al. used micro-CT to compare the airway structure of several inbred strains of mice; marked differences were noted between several of the murine strains [63]. Johnston et al. also used micro-CT to examine the airway structure from fixed and

excised mouse lungs [54]. Several groups have used micro-CT to study animal models of pulmonary fibrosis [54,64]. Johnson used micro-CT to quantify pulmonary fibrosis in rats; rats exposed to bleomycin, a rodent model of pulmonary fibrosis, showed increased lung densities [54]. Ask et al. used a replication deficient adenovirus carrying active TGF-β1 to induce fibrosis in rats and found that micro-CT derived lung densities were increased in fibrotic animals [64]. Froese et al. showed significant decreases in lung density measured by micro-CT in a mouse model of emphysema [65]. The decreases in lung density seen using micro-CT were highly correlated with measurements of airspace size, suggesting that the micro-CT system was capable of quantifying changes in lung structure. Jobse et al. used microCT to quantify inflammation levels in a rat model of allergic lung inflammation [66]. Inflamed animals showed significant increases in density within the lungs. The areas of increased density were found to be primarily around the major airways. Lederlin et al., used microCT to study airway remodeling in a mouse asthma model; animals challenged with ovalbumin were found to have greater densities surrounding the major airways and this was correlated with histological data showing increased smooth muscle deposition [67].

Axial, coronal, and sagittal slices of a representative CT (un-gated) of a healthy rat lung acquired using the X-SPECT system is displayed in Figure 1.3.1.

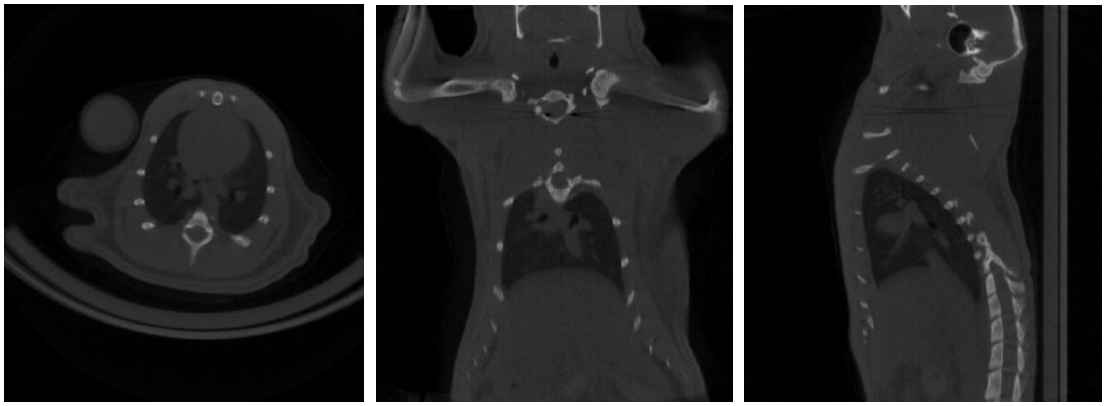

Figure 1.3.1: Axial, coronal, and sagittal micro-CT of a healthy rat thorax

1.3.2 Imaging Function

Lung function can be imaged using several of the previously mentioned modalities. Emission tomography is a very useful tool for studying both ventilation and perfusion within the lung. Jose Venegas and colleagues have used $^{13}N_2$, a positron-emitter used in PET imaging, to evaluate both ventilation and perfusion in the lung [68-70]. They used inhaled $^{13}N_2$ gas to measure regional specific lung volume changes in

sheep [68]. In another study, a $^{13}N_2$-saline solution was injected to first measure pulmonary perfusion and then ventilation in patients with and without COPD [69]. The low solubility of nitrogen in body fluids and tissues causes all of it to move into the alveolar airspaces at first pass through the lungs; areas that are poorly ventilated will retain $^{13}N_2$ gas for longer than healthy regions. They found that COPD patients had greater perfusion heterogeneity and that ventilation gradients were only observable in healthy individuals [69]. Pulmonary blood flow can also be imaged using $H_2{}^{15}0$, another PET tracer [70].

In SPECT imaging, ^{99m}Technium is commonly used as a radiolabel. Ventilation has been assessed using inhaled carbon particles labeled with ^{99m}Tc, a compound called Technigas [71]. To measure perfusion, ^{99m}Tc-labeled macro-aggregated albumin (MAA) is injected into the venous blood and is trapped in the capillary beds of the lung, showing which areas of the lung are perfused and which are not [72]. Examples of ventilation and perfusion images obtained in rats with ^{99m}Tc and SPECT, overlaid onto their CTs, are shown in Figure 1.3.2

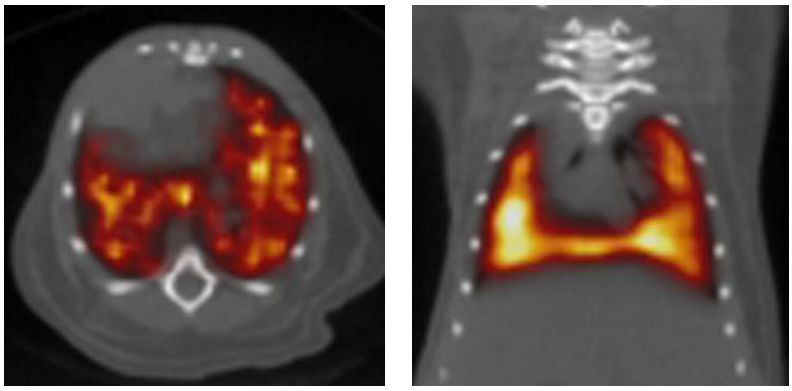

Figure 1.3.2: Functional SPECT images overlaid on CT. Axial ventilation SPECT (left), coronal perfusion SPECT (right) [Courtesy of the Labiris Research Laboratory]

The relationship between ventilation and perfusion in the lung is a vital aspect of lung function [72]. In healthy individuals, the lung diverts blood flow away from areas which are not being ventilated in order to maximize gas exchange efficiency. Although primarily an anatomical imaging technique, CT can be used to assess ventilation by utilizing inhaled xenon gas [73]. Vascular CT contrast-agents, discussed in section 1.3.3, can be used to examine the distribution of blood flow with the lung.

In MRI, hyperpolarized gases such as ^{3}He and ^{129}Xe represent the best ways to assess pulmonary ventilation [55,74,75]. These hyperpolarized techniques, however, are more costly and less accessible than techniques which utilize emission tomography. They require a system for hyperpolarizing gases and specially tuned RF coils. Using these

hyperpolarized techniques, obstructive lung diseases such as COPD and asthma can be assessed [55,76]. Contrast-enhanced MR, discussed in section 1.3.3, provides another method for studying pulmonary perfusion.

Many other biological processes in the lung can be observed using emission tomography. ^{18}FDG can be used as a marker of tumours and neutrophilic inflammation [77,78] and ^{18}F-labelled proline can be used as a marker for fibrosis [79]. Mucocilary clearance can be studied by tagging large particles such as sulphur colloid which become trapped in mucous and are removed from the lung by the action of beating cilia [80].

1.3.3 Contrast Agents

Contrast agents can be used to make certain anatomical areas stand out more from the surrounding tissue. In x-ray and CT applications, materials that increase photon attenuation are typically used. Hislop et al., in 1976, injected a barium sulphate gelatine mixture into the pulmonary arteries of excised rat lungs [81]. The presence of the contrast agent within the arteries gives the structure a bright appearance within x-ray images and allowed measurements of the structure to be acquired. In modern clinical CT, iodine-based contrast agents are widely used to increase contrast between the pulmonary blood supply and the surrounding tissue [82]. This increased contrast provides greater information regarding vascular abnormities in the lung. Iodine-based contrast agents have also been used in μCT imaging applications [83,84]. Figure 1.3.3 illustrates the use of iodine-based contrast agents being used to visualize vascular anatomy in the rat.

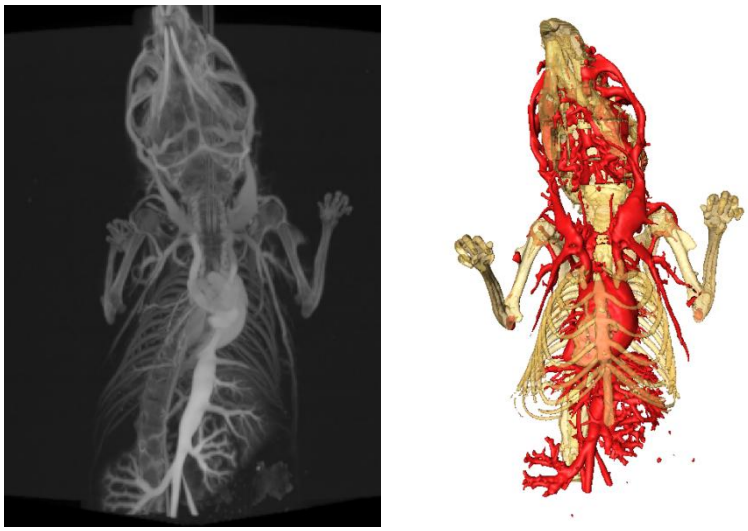

Figure 1.3.3: Contrast-enhanced vasculature in a rat using Omnipaque

Unlike clinical CT, pre-clinical CT research has investigated the use of several contrast agents which do not require subject survival. Lead based contrast agents have been utilized to image vasculature in both rats [85,86] and in mice [87]. Molten et al., in a series of studies, used perfluorooctyl bromide (PFOB) as a vascular contrast agent to visual the pulmonary arteries of rats [88-90].

In MRI, vascular contrast agents based on gadolinium are used to highlight vascular structure [55]. Some patients, however, can experience adverse effects using gadolinium contrast agents due to potential renal toxicity. Gadolinium-based contrast agents can also be utilized in CT applications [91].

1.3.4 Histology

Although medical imaging technology has provided a number of tools for imaging both lung structure and function, limitations in system resolutions still prevent a complete analysis of the lung. Even μCT, which provides one of the highest resolution techniques for imaging lung structure (resolving powers down to about 10 μm), still lacks the ability to resolve the microstructure of either the human or the rodent lung [92].

The cellular structure of the lung can be studied through histological processing of lung tissue [93]. Tissue samples from the lung are first fixed (typically using formalin), cross-linking proteins to maintain tissue dimensions and prevent tissue breakdown. They are then embedded in a semi-solid medium such as paraffin before being sectioned extremely thin (typically 5 μm thick) using a microtome. These slices are then treated with various stains to target and highlight certain types of cells [93]. The most common type of stain, haematoxylin and eosin (H&E), is used to examine cellular structure. Haematoxylin stains the nuclei of cells and several other structures blue. Eosin stains eosinophilic structures various shades of red, pink, and orange. The tissue is then examined at high magnification under a light microscope. These high magnification histology images can have resolving powers that are approximately an order of magnitude higher than the highest resolution micro-CT systems [92]. Lung histology images are used to study a number of different phenomena and disease-related changes within the lung. The changes in alveolar size which accompany emphysema and several other diseases of the lung are typically assessed using histological analysis [93]. Figure 1.3.4 shows an example of lung histology from a mouse at both low and at high magnification.

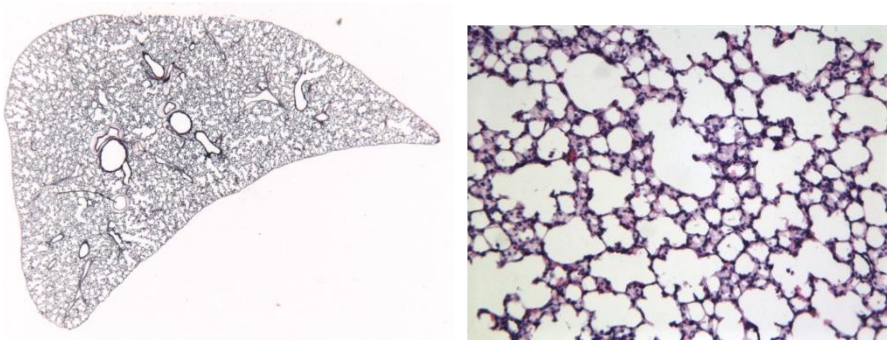

Figure 1.3.4: Histology from a healthy mouse lung. Low magnification (x16) image with 6.9 μm pixels (left). High magnification (x100) image with 0.98 μm pixels (right).

Histology is an extremely useful technique for examining the micro-structure of the lung. Most imaging techniques, including most μCT systems, do not have the resolution to study lung parenchyma or airway tissues. Histology, therefore, allows alveolar structure to be observed and measured, allowing the progression of lung disease to be studied. A large disadvantage of this technique as compared to medical imaging techniques, however, is that it requires sacrifice of the animal and hence represents only a snapshot in time.

1.4 Image Processing

1.4.1 Image Format

In two dimensions, an image is comprised of a number of picture elements, or pixels. The essence of any image is contrast; the ability to differentiate parts of the image based on different pixel values. Binary images contain two possible pixel values: 0 and 1 (or on and off). As the number of possibilities for any given pixel value increases the amount of size required to store the image increases. In three dimensions, an image is said to be comprised of a number of volume elements, or voxels. A three dimensional image can be thought of as a stack of two dimensional images. These three-dimensional matrices can be sliced in virtually any plane for two-dimensional visualization.

1.4.2 Image-Segmentation

A great deal of interest has been dedicated to the segmentation of structures from medical images [94-109]. Segmentations allow structures from within an image to be visualized in three dimensions. A segmentation is essentially a group of pixels or voxels within an image that satisfy a certain criteria. This is represented as a binary image with the selected voxels being on and the unselected voxels being off. The simplest example would involve the selection of all voxels within an image falling into a certain range of values. Selecting all voxels around 1000 HU in a typical CT image, for example, would isolate the voxels belonging to the skeleton. Alternatively, selecting voxels below -250 HU would isolate the lungs, any gas in the bowels, and the air surrounding the subject. More complicated schemes can be used to isolate more complicated parts of the anatomy such as fat, which is becoming popular in obesity research.

The segmentations mentioned above, based on density values, contain no criteria for connectivity and thus volume-growing (also called region growing) techniques have been introduced. A volume-growing algorithm starts with a single voxel that is usually selected manually by a user. Although a voxels value is still critical to its inclusion or exclusion from the segmentation the concept of connectivity now comes into play. The algorithm therefore begins with the initial voxel (or seed point) and adds neighboring voxels if they fall into the specified value range. Once a neighbouring voxel is added to the segmentation, its neighbours are checked to see if they fall into the specified value range. The process continues until no more voxels can be added to the segmentation. By selecting a seed point within the lung, it therefore becomes possible to segment just the lungs without segmenting any other low density areas within the image. Various segmentations based on different thresholds are displayed in Figure 1.4.2

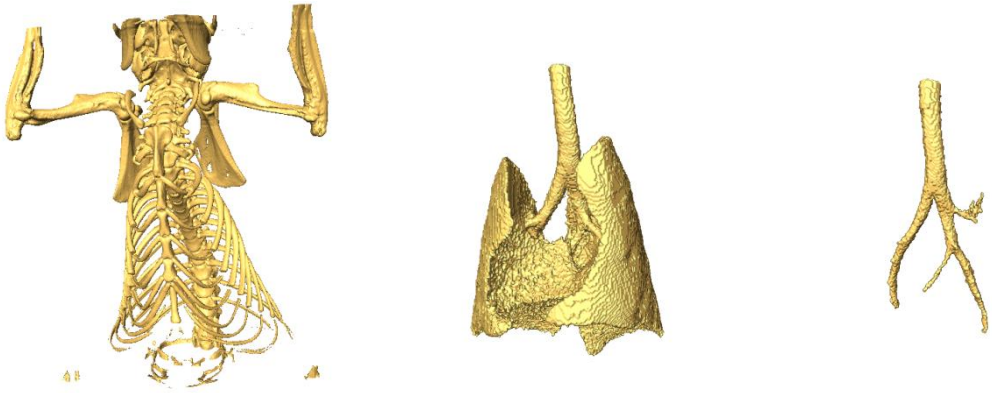

Figure 1.4.2: Segmented volumes from a micro-CT image of a rat. Left: segmentation of skeleton obtained by selecting all voxels above 500HU. Middle: lung segmentation using region-growing (seed point in trachea selected manually) with an upper threshold of -250 HU. Right: airway segmentation using region-growing (seed point in trachea selected manually) with an upper threshold of -550 HU.

Alternative lung segmentation methods also exist that are not based on voxel values [66]. These include regions that are drawn by a user. An example is a thoracic segmentation used by Jobse et al., created using the ribcage to manually outline the thorax, including the lung and heart [66]. Similar methods have also been used to draw regions of interest around the main airways [67].

1.4.3 Centre-Line Extraction

Certain two- and three-dimensional structures can be represented by their centre-line. A process known as skeletonization, or centre-line extraction, is used to reduce a segmented volume into a single path of connected voxels that is representative of the original structure [110-116]. The skeleton of a segmented volume can be acquired using a number of different algorithms. In this work, skeletonization was accomplished using two coded maps of the segmented volume. In the first map, known as the seed map, each voxel is assigned a value equal to the iteration of the volume growing algorithm that captured that voxel. The seed point is first assigned a value of 1. Voxels neighbouring the seed point that are included in the first round of volume growing are assigned a value of 2. The process continues so that every voxel added to the growing volume is assigned a value one greater than that of the voxel that was added previously. Figure 1.4.3.1 illustrates axial and coronal slices of the seed map within the trachea.

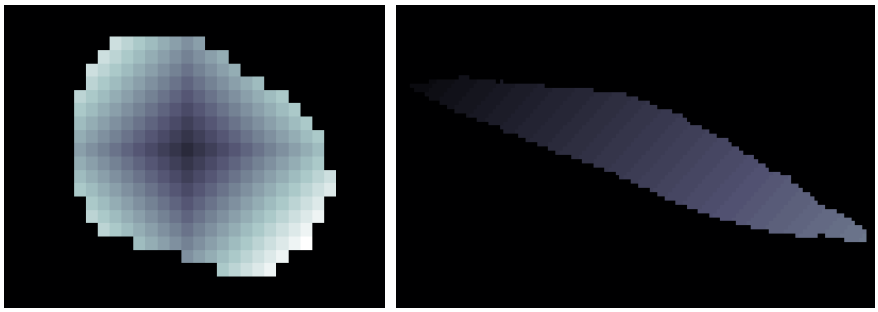

Figure 1.4.3.1: Seed Map; axial and coronal slices of the trachea

The second coded map of the segmented volume, known as the distance map, reflects each voxel's distance from the nearest background voxel (i.e. A voxel not contained in the segmentation). Voxels closer to the segmentations centre therefore have values greater than voxels closer to the periphery of the segmented volumes. An axial and coronal view of the distance map within the trachea is illustrated in Figure 1.4.3.2.

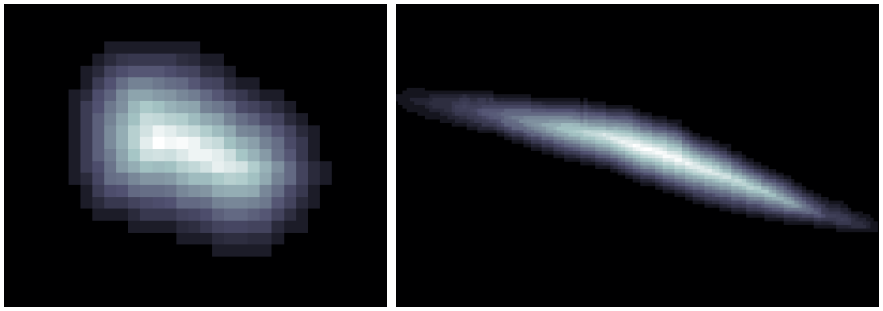

Figure 1.4.3.2: Distance Map; axial and coronal slices of the trachea

The first step in extracting the centre-line of an object is to identify its endpoints. Endpoints are found by detecting local maximums in the seed map. The size of region defining a local maximum will affect the concentration of endpoints detected for the object. If the region is too large then too few endpoints will be detected, while if the region is too small, then too many endpoints will be detected. The concept is illustrated in figure 1.4.3.3 (left) using a 7x7x7 voxel neighbourhood for determining local maximums in the seed map. After acquiring a list of the structure's endpoints, each can be traced back to the initial seed map through the segmented volume. This is done using both the seed map and the distance map. The seed map drives each endpoint back to the original seed point while the distance map drives its path towards the centre of the segmented volume. This concept is illustrated in Figure 1.4.3.3 (right).

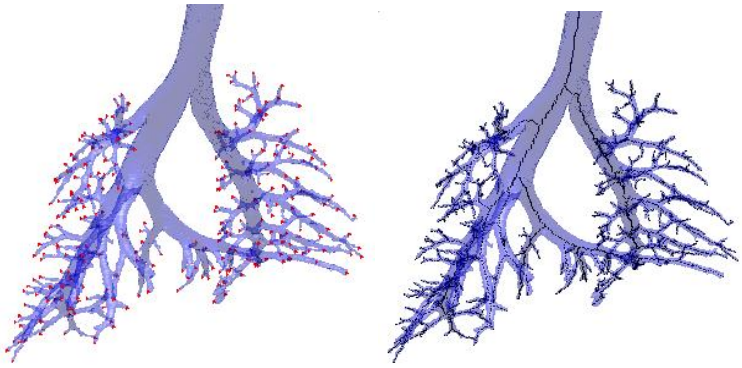

Figure 1.4.3.3: Endpoint detection (left), centre-line extraction (right)

This concept is used in chapter 2 to characterize the segmented lung structures from CT images. Using this technique the location of branching points can be determined and measurements of diameter can be made.

1.4.4 Dilation/Erosion

Dilations and erosions represent two important operations in image processing. When an object is dilated it becomes larger and when an object is eroded it becomes smaller. The degree to which an object becomes larger or smaller is dependent on the structuring element, which determines the pattern of pixels (or voxels) that are included in the dilation or erosion operation. The simplest structuring element in two dimensions is a single pixel surrounded by its four face neighbours. During a dilation, the structuring element is centered on each of the pixels comprising the original shape. If any pixels of the structuring element do not already belong to the original shape, then they are added in the dilation. During an erosion, the structuring element is centered on each of the background pixels (pixels not belonging to the original shape). If any pixels of the structuring element belong to the original shape, then they are removed during the erosion. An example of a simple dilation and erosion is shown in Figure 1.4.4.1.

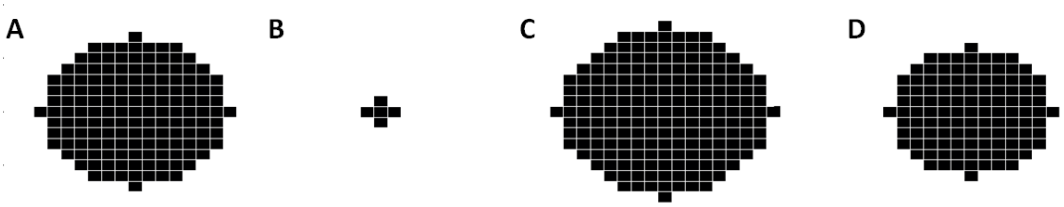

Figure 1.4.4.1: Dilation and Erosion. A) Original shape. B) Structuring Element. C) Dilated shape. D) Eroded Shape

Dilations and erosions are opposite operations. A dilation followed by an erosion, both using the same structuring element, is known as a closing operation and will return an object similar to the original shape, although small holes and indentations within the shape will be filled. An erosion followed by a dilation, known as an opening operation, will return an object similar to the original shape, provided the original shape was large enough to survive the erosion. During this opening operation, small extrusions on the original shape will be removed. Closing and opening operations are illustrated in Figure 1.4.4.2.

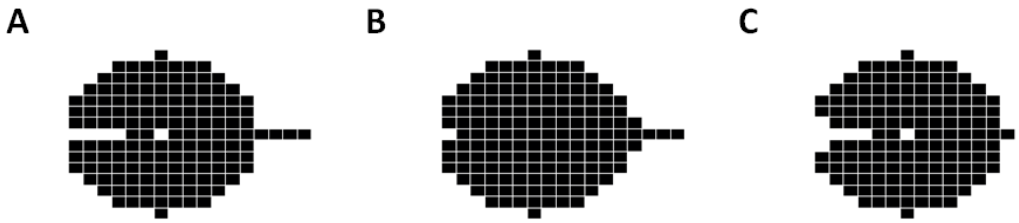

Figure 1.4.4.2: Closing and Opening. A) Original shape. B) Closed Shape. C) Opened Shape.

Equivalent results can be obtained either by using a larger structuring element or by using a smaller structuring element multiple times. The process works the same in three dimensions, although the possibility for structuring elements of different shapes is increased.

1.5 Pulmonary Modeling

1.5.1 Conceptual Lung Models

In general, a model is a something that represents something else. Usually this entails simplifying assumptions which allow specific questions to be answered regarding the object being modeled. The lung is modeled most simply as an elastic balloon at the end of a rigid tube [117]. In this model, the balloon represents the elastic alveolar structure where gas exchange occurs and the rigid tube represents the conducting airway tree supplying the alveolar region with inhaled gases. Although this model is infinitely more simplistic than the structure it represents, it does facilitate understanding of how the lung works. A more complicated version of the balloon and tube model is the single-compartment linear model of the lung [117]. In this model, the balloon is replaced with a pair of telescoping canisters connected to each other by a spring which becomes stretched as the volume is increased. This model sheds light on the relationships between volume, pressure, and flow.

1.5.2 Anatomical Lung Models

The first anatomical models of the lung were created using casts of the airways and pulmonary vasculature. In the 1870s, the Swiss anatomist Theodor Aeby created casts of the human bronchial tree [10]. In the 1980s, Ewald Weibel and Dimingo Gomez

made measurements from vinyl acetate casts of both the human airways and pulmonary vasculature created by Liebow et al. [118]. Following in the footsteps of Weibel and Gomez, numerous other researchers have created casts of either the airways or pulmonary vasculature of other mammalian species, most often those used for research purposes [16,119-122].

With the advent of computers and medical imaging technology, the door has been opened for innovative ways of visualizing airway and vascular structure. Volumetric images of lung anatomy were made available using several modalities, the most notable being CT. Following image acquisition, digital casts of the lung can be extracted, or segmented, from the reconstructed images [63,85,100]. Going further, these digital casts can then be modeled as networks of interconnected cylinders or using non-rational uniform b-splines (NURBS) [123].

Schmidt et al. first segmented the airways from high-resolution CT images, essentially creating a digital cast of the human airways, before creating a tube-like representation of the segmented airways [124]. This airway model was specific to the individual CT from which it was created. Gemci et al. used the Schmidt airway model for computational fluid dynamics (CFD) to study the distribution of airflows [125]. Anatomical models of both human and ovine airways, similarly to those of Schmit et al, were created by Tschirren et al [100,126].

These anatomical models are specific not only to the individual being imaged but also to individual images of the same individual acquired at different time points. Anatomical models only contain the anatomical features that are visible and measureable within the image.

1.5.3 Mathematical Lung Models

Mathematical lung models use a series of mathematical rules to generate lung structure and can be applied to different individuals. Unlike anatomical models, mathematical models are not specific to a given subject but look to reproduce trends that are common to a group. They are valuable because they can potentially be applied to different individuals and across multiple species.

The concept of fractal geometry, a new branch of mathematics introduced in 1982 by Benoit Mandelbrot, has contributed to the understanding of lung anatomy [10]. Mandelbrot modeled the airways as a continually branching structure exhibiting self-similar properties, basically a pattern that repeats itself over and over on increasingly smaller scales. Fractal-based mathematical models of the lung, developed by several

research groups, have added increasing levels of complexity to Mandelbrot's fractal lung model.

Bates used a set of repeating rules to generate the radii and lengths of 10 generations of airways; the model was used to investigate how bronchoconstriction patterns affected overall airway resistance [127]. Glenny et al. used a highly simplified fractal-based model of the pulmonary vasculature to simulate perfusion within the lung [128]. Venegas et al. used a two-dimensional Mandelbrot-like bronchial tree model to study the effects of bronchoconstriction heterogeneity in asthma [129]. Martonen et al. developed a fractal-based two-dimensional model of the human airways, employing a self-similar branching algorithm to fill a two-dimensional lung boundary [130,131]. The model was used to analyze planar gamma camera images of pulmonary ventilation and perfusion. Canals et al. developed a similar two-dimensional model of the bronchial tree and used it to estimate departures from several optimality principles [132]. In a further increase in complexity, the Martonen airway model was extended to three-dimensions [133]. The 3D model was first projected into two-dimensions to analyze planar gamma camera images [134] before finally being applied to three-dimensional SPECT images of inhaled drug deposition [133].

Tawhai et al. developed a three-dimensional model of the human airways based on a volume-dividing branch algorithm which filled a lung boundary derived from high-resolution CT images [135,136]. Like the Martonen model, their model was based on the principles of fractal geometry. In a subsequent paper [126], their model was used to extend CT-derived anatomical airway models beyond the resolution limits of the CT. The algorithm utilized CT-derived lung boundaries to contain the volume-filling branch algorithm. Tawhai et al. also applied their technique to extend CT-derived anatomical models of the pulmonary vasculature [137,138]. Venegas et al. used the model developed by Tawhai et al. to investigate which combinations of airways could be constricted to replicate ventilation patterns seen in $^{13}N_2$-saline PET images of asthmatic subjects [139].

Kitaoka et al. developed a mathematical model of the human airways which also uses a volume-dividing branch algorithm [140]. In a subsequent paper arterial and venous components were added alongside the airways [141]. Virtual CT images of the model were then created by assigning voxels in the model values equal to the HU-values of the corresponding tissues. The Kitaoka model was used by Segars et al. to extend the airways within their NCAT phantom, creating an increasingly more realistic model of the human torso for three-dimensional imaging simulations [142].

In rodents, Lee et al. modeled the shape and curvature of individual asymmetric airway bifurcations [143]. They validated their model by comparison with measurements from airway casts of a Sprague-Dawley rat.

The advantages of mathematical models, many of which are based on the principles of fractal geometry, include their versatility and subsequent ability to be applied to different subjects. As seen, they can be used in conjunction with anatomical models to extend them beyond the limitations of their source. The strength of mathematical models is also their disadvantage however, because they are not specific to certain individuals.

1.6 Thesis Objectives

The larger components of pulmonary anatomy, the airways and major blood vessels, can be visualized using μCT. The finer components of the lung, the respiratory bronchioles and alveoli, are too fine to be resolved with the μCT system at hand. They can, however, be resolved and measured within histology images.

Various functional processes occurring within the rodent lung can be investigated using μSPECT and μPET. Functional images are often overlaid onto anatomical images to provide the most complete picture possible. The overall objective of this work was to observe and quantify rodent lung anatomy and to bridge the gap between lung structure and pre-clinical images of the rodent lung acquired using μCT, μSPECT, and μPET. Understanding the relationship between structure and function in the lung is an essential first step for the regionalization of functional imaging data and helps to improve our understanding of functional changes within the lung. These images serve a critical role in pre-clinical research and ultimately help to improve our understanding of respiratory diseases in humans.

The first objective was to visualize and measure lung anatomy using the available μCT system. This included both the airways and pulmonary vasculature of both the Sprague-Dawley rat and the BALB/c mouse, two rodent strains widely used in medical research. This data was used to inspire and validate a mathematical model of the rodent lung.

The second objective was to create a model of the rodent lung which could be applied to both anatomical and functional lung images, facilitating regionalization of imaging data and tracking disease progression in individual animals over time. A secondary application of the model should allow the simulation of: 1) certain lung diseases, 2) particle deposition, 3) bronchoconstriction patterns and changes in airway resistance. Various parameters can be varied to investigate their effects on the simulated results.

The third objective involved going beyond the limits of the μCT resolution and acquiring measurements at a microstructure level in the alveolar region. This entailed

utilizing lung histology. The objective was to develop an automated method for quantifying and characterizing airspaces in whole histological lung slices. This would be very valuable because it would largely eliminate the potential for sampling bias inherent in most histological analyses, which may lead to diseased areas being missed or overestimated, especially in cases of heterogeneous lung disease. It will also greatly reduce analysis time compared to current methods.

Together these objectives provide an increased understanding of the anatomy underlying pre-clinical images of the rodent lung. Remaining for posterity would be 1) a database of measurements from both the rat and mouse lungs, 2) software for generating lung models within μCT images of the thorax and the overlaid functional data acquired using μSPECT or μPET, 3) software for investigating the effects of various parameters on the deposition of inhaled particles and bronchoconstriction, 4) software for quantifying airspaces in whole histological lung sections (*Pneumometrics*).

2 Airway and Pulmonary Vascular Measurements Using Contrast-Enhanced Micro-CT in Rodents

2.1 Synopsis

The purpose of this section was to visualize and measure rodent lung anatomy, furthering our understanding of airway and vascular structure and the relationship between them. These observations served as a basis for a mathematical lung model that can be applied to both anatomical and functional images of the rodent lung. In this work, the airway and pulmonary vasculature was visualized and measured using micro-CT. It was determined that the resolution of our CT system was not high enough to adequately visualize the smaller airways. A high-density contrast agent was therefore used to allow visualization of the finer airway structure. A similar problem was encountered when visualizing the pulmonary vasculature. The resolution of the CT prevented adequate visualization of the smaller vascular structures. Again we used a high-density contrast agent. Clinically, a bolus of this substance is administered to increase vascular contrast. It was found, however, that to produce the desired contrast between the vasculature and the surrounding tissue it was necessary to completely replace the animal blood supply with the high-density material. It was attempted to visualize both the airways and the vasculature in a single animal but this produced unsatisfactory results. The use of contrast agents allowed us to not only visualize these structures of interest, but also to segment them from the images and make measurements from them. The obtained anatomical measurements are accessible from a rodent lung database which was used later to validate the model and can be used to further study lung structure in rats and mice.

2.2 Contribution to Manuscript

As primary author, I, WB Counter, designed and conducted the experiment, analyzed the data and wrote the manuscript. I developed all the computer algorithms to segment, measure, and analyze the data. IQ Wang helped in animal preparation; TH Farncombe provided expertise in microCT imaging and edited the manuscript; NR Labiris contributed to study design, provided financial support, expertise in lung anatomy/physiology, and edited the manuscript.

2.3 Manuscript

This manuscript has been submitted to the American Physiological Society journal, Lung Cellular and Molecular Physiology. References are listed in alphabetical order using the last name of the first author.

Airway and Pulmonary Vascular Measurements Using Contrast-Enhanced Micro-CT in Rodents

WB Counter[1,2], IQ Wang[1], TH Farncombe[3,4], NR Labiris[1,4]

[1] Department of Medicine, McMaster University; [2] Department of Medical Physics, McMaster University; [3] Department of Radiology, McMaster University; [4] Department of Nuclear Medicine, Hamilton Health Sciences, McMaster University, Hamilton, Ontario, Canada

Author Contributions:
WBC designed, conducted, and analyzed the experiment, and wrote the manuscript; IQW assisted in animal preparation and method development; THF provided imaging expertise and editing of the manuscript; NRL provided study concept/design, expertise in lung structure/physiology, aided in data analysis, provided financial support, and editing of manuscript.

Financial Support: N.R. Labiris holds an Internal Department of Medicine Career Award

Running Head: Imaging Lung Structure in Rodents

Word Count: 4829

Correspondence: Name: Dr. Renée Labiris
Mailing Address: 1280 Main St. W., Hamilton, Ontario, L8S 4K1, Health Science Centre, rm. 1V11
Phone: 905 521-2100 ext. 75657
Fax: 905 546-1125
Email Address: labir@mcmaster.ca

Abstract:

Pre-clinical imaging allows pulmonary researchers to study lung disease and pulmonary drug delivery non-invasively and longitudinally in small animals. However, anatomically localizing a pathology or drug deposition to a particular lung region is not easily done. Thus, a detailed knowledge of the anatomical structure of small animal lungs is necessary for understanding disease progression and in addition would facilitate the analysis of the imaging data, mapping drug deposition and relating function to structure. In this study, contrast-enhanced micro- computed tomography (CT) of the lung produced high resolution images that allowed for the characterization of the rodent airway and pulmonary vasculature. Contrast-enhanced micro-CT was used to visualize the airways and pulmonary vasculature in Sprague-Dawley rats (200-225g) and BALB/c mice (20-25 g) post-mortem. Segmented volumes from these images were processed to yield automated measurements of the airways and pulmonary vasculature. The diameters, lengths, and branching angles of the airway, arterial, and venous trees were measured and analyzed as a function of generation number and vessel diameter to establish rules which could be applied at all levels of tree hierarchy. In the rat, airway, arterial, and venous tress were measured down to the 20^{th}, 16^{th}, and 14^{th} generation, respectively. In the mouse, airway, arterial, and venous trees were measured down to the 16^{th}, 8^{th}, and 7^{th} generation, respectively. This structural information, catalogued in a rodent database, will increase our understanding of lung structure and will aid in future studies of the relationship between structure and function in animal models of disease.

Key Words: Computed Tomography, Contrast Agents, Pulmonary Circulation, Airway Nomenclature

Introduction:

The lung is a complex organ that works dynamically and must react to changes in posture, environment and disease [20]. Its major function is gas exchange; bringing oxygen into the body while removing carbon dioxide. To accomplish this task, a well-coordinated interaction between the lung and pulmonary circulation is essential. The rodent lung is comprised of two branching networks: the airways and pulmonary vasculature. With the advent of small animal imaging systems, researchers are able to visualize these networks *in situ*, and non-invasively study the progression of lung disease and assess drug efficacy in animal models of disease. Much of this research involves combining the anatomical data obtained using Computed Tomography (CT) with the functional data obtained using Single Photon Emission Computed Tomography (SPECT) or Positron Emission Tomography (PET). A detailed knowledge of the structure of the lung would facilitate the mapping of functional data relative to lung anatomy and thus, further our understanding of how changes in lung structure affect its function.

Most rodent lungs are divided into five lobes by fissures; 4 on the right and 1 on the left [37]. The lung contains two zones, a conducting zone that transports air into and out of the lung and a respiratory zone where gas exchange occurs. The conducting zone starts at the trachea and branches into the two main bronchi that enter the lung. The bronchi continue to branch until they reach the respiratory zone, the alveolar sacs. To describe the airway network, two different naming systems are typically used. The most common of these, "generation", was introduced by Weibel in 1963 [39]. Starting with the trachea at generation 0, the generation number is increased by one at every bifurcation. This terminology is commonly used for the human airways but does not take into account the more asymmetric structure of the rodent lung. An alternative terminology, known as "order", was introduced by Wallau et al. in 2000 [38] to account for the asymmetry in the rodent lung. In this naming scheme, an airway segment can be assigned the same order as its parent segment if its diameter is significantly larger than that of its sister segments. Otherwise, all daughter segments receive an order one greater than that of their parent segment. This is not to be confused with the concept of order introduced by Horton and Strahler, which was applied to the human airways by Horsfield [9] in 1990. In this system, terminal segments are assigned an order of 1 and hence the tracheal order is dependent on the degree of segmentation. It is possible that neither generation nor order perfectly describes tree hierarchy within the rodent lung and the choice of naming schemes may depend on the desired application.

The pulmonary airways are accompanied by an extensive vascular network, allowing the oxygenation of blood travelling through the lungs [37]. The pulmonary vasculature is comprised of two branching networks connected by a shared capillary bed,

the actual site of gas exchange. The structure of both the arterial and venous vasculature within the lung is similar to that of the airways, permitting similar classifications of tree hierarchy.

A number of studies have examined lung structure by creating casts of either the pulmonary airways [4,17,24,36,39] or pulmonary vasculature [12]. The development of medical imaging techniques has allowed lung structure to be studied *in situ*. The segmentation of structures from medical imaging data has received significant attention [19]. The air in the conducting airways provides good contrast between that structure and the surrounding lung parenchyma and has resulted in a great deal of attention being directed towards the segmentation of the airways from clinical CT images [3,5,6,16,32,34,35,43]. Several researchers have attempted to apply these same techniques to micro-CT images of small animals [2,13,29,30,33,36]. Limitations in CT resolution often prevent adequate segmentation of the airways, and as a result, several high-density contrast agents have been used. Segmentation of the pulmonary vasculature from micro-CT images presents an even more difficult task due to the similar intensity values between blood and soft tissue. Several groups have examined the use of different vascular contrast agents in small animals to study vascular anatomy and how it is affected by disease [7,8,14,15,22,24,28,40,44]. Although these techniques allow visualization of the pulmonary vasculature, they seldom include both the arterial and venous components and are mostly done *ex situ* [8,14,24], potentially leading to an over-inflation of the lung and a loss of its physiological dimensions.

The objectives of this study were to visualize both the pulmonary airways and vasculature of the Sprague-Dawley rat and BALB/c mouse *in situ* using contrast-enhanced micro-CT imaging post-mortem. From these images, parameters such as diameter, length and branching angles were automatically measured to create an anatomical database for normal rodent lungs. Imaging was done *in situ* to maintain the physiological shape and pressure of the lung.

Materials and Methods:

Animals

Male Sprague-Dawley rats (*Charles River Laboratories, Wilmington, MA*) weighing 200-225g and male BALB/c mice (*Charles River Laboratories, Wilmington, MA)* weighing 20-25g were used. One cohort of animals (n=5 rats, mice) were used for airway visualization and a second cohort (n=5 rats, mice) were used for vascular visualization. All animals within a species were age, weight, and sex matched. All

animal experiments were approved by the Animal Research Ethics Board at McMaster University, in accordance with the Canadian Council on Animal Care guidelines.

Airway Visualization using Micro-CT

Microfil MV-122 (*FlowTech Inc, Carver, MA*), containing lead chromate, was used as a high-density contrast agent to visualize the conducting airways of rodents in micro-CT images. Animals were anaesthetized using 4-5% isoflurane and then euthanized by exsanguination. A tracheotomy was immediately performed and the contrast agent was infused into the airways using a perfusion pump (*Thermo Electron Corp., Beverly, MA*) with a constant flow rate of 0.33 ml/min for rats and 0.033 ml/min for mice. Optimal infusion volumes were determined experimentally and found to be about 1 µl/gram body weight. Micro-CT images were acquired using a hybrid SPECT/CT (*X-SPECT, Gamma Medica, Northridge, CA*) with the following parameters: 1024 projections, 75 kVp and 205 µA. Images for rats were reconstructed using a Feldkamp filtered backprojection algorithm into 0.115 mm isotropic voxels to create a 512x512x512 image. Images of the mouse lung, which did not require as large a field-of-view as the rat lung, were reconstructed into 0.080 mm isotropic voxels using the same reconstruction algorithm. Several images were acquired pre- and post-contrast agent delivery to verify that infusion of the contrast-agent did not alter airway diameter.

Vascular Visualization using Micro-CT

Omnipaque (*GE Healthcare, USA*), containing organically bound iodine (300 mg/mL), was used as a high-density vascular contrast agent. Following sedation with 4-5% isoflurane, a catheter was placed into the tail vein and heparin (10 mg/kg body weight) was administered. Omnipaque was then delivered via the tail vein catheter using a perfusion pump (*Thermo Electron Corp., Beverly, MA*) with a constant flow rate of 5 ml/min for rats and 0.5 ml/min for mice. The femoral artery was severed to allow drainage of the perfusate. Following exsanguination, the lungs were inflated with air delivered via a tracheotomy to improve perfusion within the lung (3 ml for the rat, 0.3 ml for the mouse). Perfusion continued until the fluid draining from the severed femoral artery turned clear. The femoral artery was then clamped off to prevent leakage of the contrast agent during the image acquisition. The CT parameters and reconstruction algorithms were the same as for the airway visualization detailed above.

Airway & Vascular Segmentation

Images were smoothed using a 3D Gaussian filter with a sigma value of 1 voxel and a kernel of 3 voxels. Regions corresponding to the lungs were manually extracted from the CT datasets using Amira 4.1.1 (*Mercury Computer Systems Inc., San Diego, CA*). This included the removal of the descending aorta and the vena cava from each lung volume. A volume-growing algorithm was then employed to extract the high-density regions of interest, either the airways or vasculature, from the lung regions. The algorithm began with the manual selection of a seed point located at the approximate centre of the main vessel (trachea for the airways, main pulmonary artery for arterial, main pulmonary vein for venous). Any of the seed point's six face-neighbours were added to the segmentation if they satisfied one of two conditions; either 1) the voxel had an intensity value greater or equal to 1500 HU or 2) the voxel was between 500 and 1500 HU and it's intensity value was twice the mean value of the group of it's surrounding voxels. The procedure was repeated until no more voxels were added to the segmentation. The algorithm recorded the number of steps that each voxel was away from the seed point, which was used later to locate the terminal points of the structure and is referred to as a seed map. Terminal points were defined as the voxels of the segmented volumes that were most distal from the seed point and hence where identified as local maximums in the seed map. Segmentation of the pulmonary vasculature proceeded in a similar fashion using the same density (HU) thresholds. The vascular data required an additional step to separate the vasculature into the arterial and venous components. Voxels from the fully segmented vasculature were assigned to be either arterial or venous based on their proximity to voxels which belonged conclusively to either the pulmonary arteries or pulmonary veins. The process began with separate segmentations of both the arterial and venous trees, acquired by increasing the volume-growing threshold so that no connected voxel path existed between the pulmonary arteries and veins. This allowed the pulmonary arteries to be segmented without segmenting the pulmonary veins and *vice versa*. The two separate segmentations were then alternatively dilated within the full vascular segmentation until most of the voxels in the full segmentation were assigned as either arterial or venous. A small percentage (<1%) of voxels from the full vascular segmentation were not assigned as arterial or venous due to their proximity to the shared capillary bed.

Anatomical Measurements

Each of the three segmented structures (airway, arterial, venous) was measured by first detecting the relative positions of both it's terminal points and it's branching points. A branching point was defined as a single voxel representing the location of a bifurcation within a segmented structure (as detailed below). This allowed each of the structures to

be modelled as a network of cylindrical tubes, or segments, connecting adjacent branching and terminal points. Each segment therefore consisted of two endpoints in 3D space and a diameter, which was measured along the length of the segment and averaged for that segment.

The segmented trees (airway, arterial, or venous) contained information regarding each voxels distance from the initial seed point (seed map). Segmentations were also coded (distance map) to reflect each voxel's distance from the nearest background voxel (i.e. the nearest non-airway or non-vascular voxel). Terminal points were detected by searching for local maximums in the seed map. Identification of branching points was accomplished using a centre-line extraction, or skeletonization, of the segmented structure [1,10,11,17,21,23,31,42]. This was done by tracing each terminal point back to the seed point through the segmented volume. The seed map was used to drive each terminal point towards the seed point, while the distance map was used simultaneously to drive that path away from the object boundary. A smoothing step was used to optimize the path from each terminal point to the seed point. The centre-line was then coded to reflect the number of neighbouring voxels of each point; terminal points have one neighbour, regular points have two neighbours and branch points have 3 or more neighbours. A branching model, which is essentially a list of segment endpoints, was then created using the coded-centreline. The distance map provided a measure of segment radius at all points along the centre-line and allowed a calculation of average radius (or diameter, D) for each segment. The length (L) of each segment was taken to be the distance between it's two endpoints, which were either both branching points, or in the case of a terminal segment, a branch point and a terminal point. Branching angles were calculated by comparing the orientation of each segment to that of it's parent. Two branching angles were calculated; theta (θ) represents the absolute branching angle between parent and daughter segments while phi (φ) represents the rotational angle between successive bifurcations. Additional segment parameters included diameter/diameter of parent (D/D_P), length/length of parent (L/L_P), and length/diameter (L/D).

The validity of the automated anatomical measurements was measured by a Bland-Altman plot comparing a random selection of vessel diameters with standard manual measurements from the original contrast-enhanced CT image. Measurements were made by three individuals with extensive experience in lung CT measurements. Values lying within the 95% confidence interval of the difference between the automated and manual measurements were taken to imply agreement. For the manual measurements, interrater and intrarater reliability were assessed using Pearson's correlation coefficient.

Segment Classification

The generation number and order were determined for each segment according to the schemes introduced by Weibel [39] and Wallau [38], respectively. We chose not to apply the Horsfield ordering scheme due to its dependence on the degree of segmentation [9]. Generation number was assigned starting with the trachea as generation 0 and increasing generation number by 1 at each branching point. Order was assigned to each segment by first determining whether the bifurcation was symmetric or asymmetric. An asymmetric bifurcation was defined as one in which the diameters of the daughters differed by more than 10% of the larger segment. In this case, the larger daughter was assigned the same order as the parent segment and the smaller daughter was assigned an order one greater than the parent segment. In the case of a symmetric bifurcation, both daughters were assigned an order one greater than the parent segment. The trachea was assigned an order of 0 and the two main bronchi were assigned an order of 1. Each segment was assigned to one of the five lobes by defining the main segment entering each lobe. Segments were defined as major or minor depending on whether they had the same order as their parent. Segments were also divided into five diameter groups and analyzed [25]. Different diameter categories were used for the rat and mouse lungs.

Results:

The airway, arterial, and venous trees of the Sprague-Dawley rat and BALB/c mouse lung have been visualized and segmented from contrast-enhanced CT images (Figure 1 & 2). Each of the segmented volumes was modelled as a network of cylindrical tubes by detecting the location of the bifurcation points using a skeletonization algorithm (Figure 3). The smallest vessels which were able to be resolved, segmented, and measured had diameters equal to twice the voxel dimension (0.23 mm for the rat and 0.16 mm for the mouse). The lobe, generation, and order were determined automatically for each segment (Figure 4). No significant differences between airway diameters from gated end-inspiratory images and the contrast-enhanced post-mortem images were observed (Figure 5A). No significant difference was found between automated measurements made from the segmentation models of the airways and vasculature and the standard manual measurements obtained from the CTs (Figure 5B); automated and manual measurements agreed to within 10%. For the manual measurements, interrater variability had $R^2 = 0.93$ and intrarater variability had $R^2 = 0.99$.

In the rat lung an average of 562 airways were segmented. Their diameters ranged from 0.23 mm to 2 mm over 20 generations. Approximately 88% of all segments

had a diameter less than that of their parent and the mean ratio of a segment diameter to the diameter of its parent (D/D_P) was 0.80 (SD 0.22). The average branching angle (θ) was found to be 53.39° (SD 26.82°) and the average rotational angle (φ) was found to be 170.72° (SD 105.66°). The mean ratio of a segment length to its diameter (L/D) was found to be 2.66 (SD 1.99). For the arterial tree, an average of 108 vessels were segmented ranging in diameter from 0.23 mm to 1.62 mm over 16 generations. The average branching angle (θ) and rotational angle (φ) were found to be 49.35° (SD 26.77°) and 167.06° (SD 104.13°), respectively. Approximately 89% of all segments had a diameter less than that of their parent and the ratio of a segment diameter to the diameter of its parent (D/D_P) was 0.69 (SD 0.26). The mean ratio of an arterial segment length to its diameter (L/D) was found to be 3.69 (SD 2.99). For the venous tree, an average of 118 vessels were segmented with diameters ranging from 0.23 mm to 2.55 mm over 14 generations. The average branching angle (θ) was found to be 48.46° (SD 25.04°) and the average rotational angle (φ) was found to be 165.98° (SD 102.24°). Approximately 91% of all segments had a diameter less than that of their parent and the ratio of a segment diameter to the diameter of its parent (D/D_P) was 0.69 (SD 0.27). The mean ratio of a venous segment length to its diameter (L/D) was found to be 3.96 (SD 3.60). Refer to table 1 for the complete list of measurements.

In the mouse lung an average of 206 airways were segmented ranging in diameter from 0.16 mm to 1 mm over 16 generations. The average branching angle (θ) was found to be 45.61° (SD 24.27°) and the average rotational angle (φ) was found to be 172.45° (SD 102.59°). Approximately 87% of all segments had a diameter less than that of their parent and the ratio of a segment diameter to the diameter of its parent (D/D_P) was 0.72 (SD 0.24). The mean ratio of a segment length to its diameter (L/D) was found to be 3.54 (SD 2.72). For the arterial tree, an average of 45 vessels were segmented. Their diameters ranged from 0.16 mm to 0.6 mm over 8 generations. The average branching angle (θ) was found to be 47.03° (SD 25.08°) and the average rotational angle (φ) was found to be 154.22° (SD 102.91°). Approximately 87% of all segments had a diameter less than that of their parent and the ratio of a segment diameter to the diameter of its parent (D/D_P) was 0.77 (SD 0.28). The mean ratio of an arterial segment length to its diameter (L/D) was found to be 3.94 (SD 3.08). For the venous tree, an average of 51 vessels were segmented. Their diameters ranged from 0.23 mm to 1.2 mm over 7 generations. The average branching angle (θ) was found to be 49.19° (SD 25.74°) and the average rotational angle (φ) was found to be 163.25° (SD 103.26°). Approximately 94% of all segments had a diameter less than that of their parent and the ratio of a segment diameter to the diameter of its parent (D/D_P) was 0.68 (SD 0.20). The mean ratio of a venous segment length to its diameter (L/D) was found to be 3.08 (SD 2.12). Refer to table 2 for the complete list of measurements.

The airways and vascular trees of the rat were also grouped into one of five diameter categories ranging from D≥1mm (D1) to D<0.25mm (D5) (Table 3). For the airways, about 87% of the segments had diameters less than 0.5mm, while only 4% had diameters greater than 1mm. The larger airways (D≥1mm) were relatively longer in length and had smaller branching angles than those with diameters less than 1mm. For the arterial system, about 56% of the segmented vessels had diameters less than 0.5 mm, while 11% had diameters greater than 1 mm. Like the airways, the larger arterial segments (D≥1mm) were relatively longer in length and had smaller branching angles than those with diameters less than 1mm. For the venous system, about 57% of the segmented vessels had diameters less than 0.5 mm, while about 16% had diameters greater than 1mm. The airways and vascular trees of the mouse were divided into five distinct diameter categories ranging from D≥0.8mm (D1) to D<0.2mm (D5) (Table 4). The distribution of vessels within the distinct diameter groupings was similar to that of the rat. No arterial vessels of the mouse had diameters falling into the largest diameter category (D≥0.8mm).

Selected parameters were plotted as a function of generation number for each of the three physiological trees for both rats (Figure 6) and mice (Figure 7). For both rats and mice, the airway, arterial and venous data show similar trends as a function of increasing generation number. For the airways, both the diameter and length appear to exhibit a rapid decline as a function of generation number. Although less pronounced, a similar decrease as a function of generation number existed for the lengths and diameters of both the arterial and venous data. The two branching angles, theta and phi, showed similar behaviour as a function of generation number for each of the three pulmonary components. The average theta and phi values plateau at approximately 45° and 180°, respectively. The ratios D/D_P, L/L_P, and L/D remained relatively constant as a function of generation number. D/D_P exhibits less variability than either L/L_P or L/D. For all three pulmonary components, the intermediate generations (5-15) were the most numerous. Additional data, such as length and branching angles (θ and φ), can be found in supplemental data for both rats (Supplemental Figure 1) and mice (Supplemental Figure 2). For the rat data, we compared our diameter measurements to those made by Lee [18] in Sprague-Dawley rats and Yeh [41] in Long-Evans rats (Supplemental Figure 3).

Discussion:

Using contrast-enhanced CT, the airways and pulmonary vasculature of the Sprague-Dawley rat and the BALB/c mouse were visualized post-mortem. Segmentations from these images were modeled as a series of connected cylinders and automated measurements of the airway, arterial and venous trees were acquired. These anatomical measurements were analyzed by grouping segments using the traditional nomenclature for the lung, generation, and by diameter for each of the three biological trees.

For the rat, airway dimensions have been measured down to the 20^{th} generation while the dimensions of the arterial and venous components of the pulmonary vasculature have been measured down to the 16^{th} and 14^{th} generation, respectively. For the mouse, airway dimensions have been measured down to the 16^{th} generation while the dimensions of the arterial and venous components of the pulmonary vasculature have both been measured down to the 8^{th} and 7^{th} generations, respectively. This discrepancy in number of segmentable generations between the airways and vasculature is due to the removal of the shared capillary bed of the pulmonary vasculature. Unlike the more symmetric human lung, where all terminal segments have approximately the same generation number, terminal segments in the rodent lung span a larger range of generation numbers. As a consequence most segments in the rodent lung are in the intermediate generations, and only relatively few segments are of the highest generation numbers. Although our inability to resolve all the smallest vessels did contribute to the observed distribution of generation numbers, we believe the distribution was primarily due to the more asymmetric structure of the rodent lung.

Although the number of segments is considerably larger for the airway data than for either the arterial or venous data, the various parameters behave in a similar manner as a function of generation number. Similar relationships also exist between species. Intermediate generation numbers are the most numerous for both rats and mice. Average diameters and lengths as a function of generation number exhibit similar patterns. The average ratio between diameter and parent diameter remains relatively constant across all generations for both rats and mice. Both species also have large degrees of variability for theta, phi, and L/D as a function of generation.

For the airways, we compared our airway diameter measurements with those made by Lee et al [18] and Yeh et al [41]. Our data exhibited a very similar trend to that of Lee, both of which were made in the Sprague-Dawley rats. The slightly larger values and smaller standard deviations obtained by Lee were likely the result of the fact that there measurements were made in older and more developed rats [27]. Sera et al. [29] reported an average D/D_P value of 0.89 for the rat airways, measured using microfocal X-

ray CT, which is similar to our value of 0.80 (SD 0.22). They also reported an average L/D value of 2.06 which is similar to our value of 2.66 (SD 1.90). Several authors have looked at the correlation between a segments length and diameter [18,25,26,29]. Phalen et al. [25] and Phillips et al. [26], taking measurements from the same airway cast, measured L/D values for both major and minor segments. For the major segments they reported an average L/D value of 1.10 (SD 0.66) while we measured it to be 2.47 (SD 1.88) and for the minor segments they reported it to be 1.90 (SD 0.62) while we measured it to be 2.76 (SD 1.92). There are a couple of noticeable differences between our study and those of Phalen and Phillips that may account for these discrepancies. Different strains of rat (Long Evans) were used and our average measurement included all segmentable airways while they limited their analysis to segments with diameters greater than 0.4 mm. This relationship (L/D) has been used to predict a segments diameter based on its length, or *vice versa*. Although the current study is in good agreement with previously stated values, we found a large degree of variability in this relationship. The parameter D/D_P may provide a more reliable indicator of segment diameter provided that the diameter of the parent segment is known.

Segments of the various lung structures have been categorized by both generation and order. When comparing the concepts of generation and order, a useful analogy is that of road intersections. In the concept of generation, the main road splits into two smaller roads, while in the concept of order, a smaller road breaks off the main road which continues in roughly the same direction (although the "main road" becomes progressively narrower). The process of determining order is also dependent on segment diameter and small variations in these diameter measurements can lead to an inconsistent ordering of segments. Generation, on the other hand, provides a more robust naming terminology which can be applied on a segment-by-segment basis. It is widely used for human airway nomenclature and has also been used by other researchers for rodent airways [18,29,30]. Thiesse and colleagues [33] developed a novel nomenclature for rodent airways which assigns a unique name to each vessel based on its lobe and branching pattern. We believe that their naming system, although useful for first few generations, could become unmanageable when the number of segmented vessels becomes very large, necessitating the grouping of vessels by generation, order, or diameter. The various parameters (D, L, D/D_P, L/L_P, L/D, theta, and phi) were therefore analyzed as a function of generation number, providing a reliable way of categorizing the segments of each biological tree.

The current study has several limitations. First is the resolution of the micro-CT system which limits the ability to visualize and resolve the finer elements within the rodent lung. The resulting partial-volume effects can lead to variability in the segmented volumes and hence the number of segmented vessels. Thus, as mentioned, the smallest vessels that we were able to measure had diameters of twice the voxel dimension (0.23

mm for rats, 0.16 mm for mice). Variability in the distribution of the contrast agent could also contribute to this segmentation variability. A small gravity-based dependence was observed which resulted in a more complete instillation of contrast material into the lower regions (in this case dorsally due to the supine position). Due to the complexities of the pulmonary vascular network and its shared capillary bed, segmentation of vascular volumes included a reduced number of vessels compared to that of the pulmonary airways. Together, these limitations prevented us from resolving all of the smaller vessels within the rodent lungs. A further limitation was that our measurements were made post-mortem and therefore do not allow dynamic and longitudinal studies to be performed.

Our objective was not to measure every vessel in the lung but to get a sense of rodent lung anatomy that could be visualized with our micro-CT system. This data has been entered into a rodent database, the purpose of which was to inspire and validate a mathematical model of the rodent lung. The visualization, measurement and categorization of the airway and pulmonary vascular trees of Sprague Dawley rats and BALB/c mice, commonly used to model lung disease, has provided us with an increased knowledge of lung structure and has facilitated our understanding of how changes in lung structure affect its function. This will also aid in future regionalization of lung imaging data.

Acknowledgements:

The authors would like to thank the McMaster Centre for Pre-Clinical and Translational Imaging (MCPTI) for the acquisition and reconstruction of all micro-CT images. We would also like to thank Brian Jobse, Kristi Lindsay, and Cory McCurry for performing the manual CT measurements.

References:

[1] **Al-Kofahi Y, Dowell N, Pace C, Shain W, Turner JN, Roysam B**. Improved Detection of Branching Points in Algorithms for Automated Neuron Tracing from 3D Confocal Images. *Cytometry Part A, 73A: 36-43, 2008*

[2] **Artaechevarria X, Perez-Martin D, Ceresa C, Biurrun G, Blanco D, Montuenga LM, Ginneken B, Ortiz-de-Solorzano C, Munoz-Barrutia A**. Airway Segmentation and analysis for the study of mouse models of lung disease using micro-CT. *Phys. Med. Biol. 54 (2009) 7009-7024*

[3] **Aykac D, Hoffman EA, McLennan G, Reinhardt JM**. Segmentation and Analysis of the Human Airway Tree From Three-Dimensional X-Ray CT Images. *IEEE Transactions on Medical Imaging, vol. 22, No.8, August 2003*

[4] **Einstein DR, Neradilak B, Pollisar N, Minard KR, Wallis C, Fanucchi M, Carson JP, Kuprat AP, Kabilan S, Jacob RE, Corley RA**. An Automated Self-Similarity Analysis of the Pulmonary Tree of the Sprague-Dawley Rat. *The Anatomical Record 291:1628-1648 (2008)*

[5] **Fabijanska A**. Two-pass region growing algorithm for segmenting airway tree from MDCT chest scans. *Computerized Medical Imaging and Graphics 33 (2009) 537-546*

[6] **Fetita CI, Preteux F, Beigelman-Aubry C, Grenier P**. Pulmonary Airways: 3-D Reconstruction From Multislice CT and Clinical Investigation. *IEEE Transactions on Medical Imaging, vol.23, no.11, November 2004*

[7] **Grabherr S, Hess A, Karolczak M, Thali MJ, Friess SD, Kalender WA, Dirnhofer R, Djonov V**. Angiofil-Mediated Visualization of the Vascular System by Microcomputed Tomography: A Feasibility Study. *Microscopy Research and Technique 71:551-556 (2008)*

[8] **Hislop A, Reid L**. Normal structure and dimensions of the pulmonary arteries in the rat. *J. Anat. (1978), 125, 1, pp. 71-83*

[9] **Horsfield K**. Diameters, generations, and orders of branches in the bronchial tree. *American Physiological Society 0161-7567/90 (1990)*

[10] **Jiang G, Gu L**. An Automatic and Fast Centerline Extraction Algorithm for Virtual Colonoscopy. *IEEE (2005), 0-7803-8740-6/05*

[11] **Jiang H, Alperin N**. A New Automatic Skeletonization Algorithm for 3D Vascular Volumes. *IEEE EMBS (2004) 0-7803-8439-3/04*

[12] **Jiang ZL, Kassab GS, Fung YC**. Diameter-defined Stahler system and connectivity matrix of the pulmonary arterial tree. *American Physiological Society 0161-7567/94*

[13] **Johnson, KA**. Imaging Techniques for Small Animal Imaging Models of Pulmonary Disease: Micro-CT. Toxicologic Pathology, 35:59-64, 2007

[14] **Karau KL, Molthen RC, Dhyani A, Haworth ST, Hanger CC, Roerig DL, Johnson RH, Dawson CA**. Pulmonary arterial morphometry from microfocal X-ray computed tomography. *Am J Physiol Heart Circ Physiol 281: H2747-H2756, 2001*

[15] **Kindlmann GL, Weinstein DM, Jones GM, Johnson CR, Capecchi MR, Keller C**. Practical vessel imaging by computed tomography in live transgenic mouse models for human tumours. Mol. Imaging. 2005 Oct-Dec;4(4):417-24

[16] **Kiraly AP, Higgins WE, McLennan G, Hoffman EA, Reinhardt JM**. Three-dimensional Human Airway Segmentation Methods for Clinical Virtual Bronchoscopy. *Acad Radiol 2002; 9:1153-1168*

[17] **Kline TL, Zamir M, Ritman EL**. Accuracy of Microvascular Measurements Obtained From Micro-CT Images. *Annals of Biomedical Engineering, Vol.38, No.9, September 2010, pp.2851-2864*

[18] **Lee D, Fanucchi MV, Plopper CG, Fung J, Wexler AS**. Pulmonary Architecture in the Conducting Regions of Six Rats. *The Anatomical Record 291:916-926 (2008)*

[19] **Lesage D, Angelini ED, Bloch I, Funka-Lea G**. A review of 3D vessel lumen segmentation techniques: Models, features and extraction schemes. *Medical Image Analysis 13 (2009) 819-845*

[20] **Levitzky MG**. Pulmonary Physiology. *Magraw-Hill,New York, 2007*

[21] **Maddah M, Soltanian-Zadeh H, Afzali-Kusha A**. Snake modeling and distance transform approach to vascular centerline extraction and quantification. *Computerized Medical Imaging and Graphics 27 (2003) 503-512*

[22] **Molthen RC, Karau KL, Dawson CA**. Quantitative models of the rat pulmonary arterial tree morphometry applied to hypoxia-induced arterial remodelling. *J Appl Physiol 97: 2372-2384, 2004*

[23] **Palagyi K, Tschirren J, Hoffman EA, Sonka M**. Quantitative analysis of pulmonary airway tree structures. *Computers in Biology and Medicine 36 (2006) 974-996*

[24] **Pannu HK, Thompson RE, Phelps J, Magee CA, Fishman EK**. Optimal Contrast Agents for Vascular Imaging on Computed Tomography: Iodixanol versus Iohexol. *Acad Radiol 2005; 12:576-584*

[25] **Phalen RF, Yeh HC, Schum GM, Raabe G**. Application of an Idealized Model to Morphometry of the Mammalian Tracheobronchial Tree. *Anat. Rec. (1978) 190: 167-176*

[26] **Phillips CG, Kaye SR**. Diameter-based analysis of the branching geometry of four mammalian bronchial trees. *Respiration Physiology 102 (1995) 303-316*

[27] **Razavi H, Dusch MN, Zarafshar CA, Taylor CA, Feinstein JA**. A method for quantitative characterization of growth in the 3-D structure of rat pulmonary arteries. *Microvascular Research 83 (2012) 146-153*

[28] **Ritman EL**. Micro-Computed Tomography of the Lungs and Pulmonary-Vascular System. Proc Am Thorac Soc, Vol 2. pp.477-480, 2005

[29] **Sera T, Fujioka H, Yokota H, Makinouchi A, Himeno R, Schroter RC, Tanishita K**. Three-dimensional visualization and morphometry of small airways from microfocal X-ray computed tomography. *Journal of Biomechanics 36 (2003) 1587-1594*

[30] **Shi L, Thiesse J, McLennan G, Hoffman EA, Reinhardt JM**. Three-Dimensional Murine Airway Segmentation in Micro-CT Images. *Proc. Of SPIE Vol. 6511 651105-1, 2007*

[31] **Sorantin E, Halmai C, Erdohelyi B, Palagyi K, Nyul LG, Olle K, Geiger B, Lindbichler F, Friedrich G, Kiesler K**. Spiral-CT-Based Assessment of Tracheal Stenoses Using 3-D-Skeletonization. *IEEE Transactions on Medical Imaging, vol.21, No.3, March 2002*

[32] **Tawhai MH, Hunter P, Tschirren J, Reinhardt J, McLennan G, Hoffman EA**. CT-based geometry analysis and finite element models of the human and ovine bronchial tree. *J Appl Physiol 97: 2310-2321, 2004*

[33] **Thiesse J, Namati E, Sieren JC, Smith AR, Reinhardt JM, Hoffman EA, McLennan G**. Lung structure phenotype variation in inbred mouse strains revealed through in vivo micro-CT imaging. *J Appl Physiol 109: 1960-1968, 2010*

[34] **Tschirren J, Hoffman EA, McLennan G, Sonka M**. Segmentation and Quantitative Analysis of Intrathoracic Airway Trees from Computed Tomography Images. *Proc Am Thorac Soc Vol.2, pp 484-487, 2005*

[35] **Tshirren J, Hoffman EA, McLennan G, Sonka M**. Intrathoracic Airway Trees: Segmentation and Airway Morphology Analysis from Low-Dose CT Scans. *IEEE Trans Med Imaging. 2005 December; 24(12): 1529-1539*

[36] **Vasilescu DM, Knudsen L, Ochs M, Weibel ER, Hoffman EA**. Optimized murine lung preparation for detailed structural evaluation via micro-computed tomography. *J Appl Physiol 112: 159-166, 2012*

[37] **Walker WF, Homberger DG**. Anatomy & Dissection of the Rat. *W.H. Freeman and Company, New York, 1997*

[38] **Wallau BR, Schmitz A, Perry SF**. Lung Morphology in Rodents (Mammalia, Rodentia) and Its Implications for Systematics. *Journal of Morphology 246:228-248 (2000)*

[39] **Weibel ER**. Morphometry of the Human Lung. *Berlin: Springer, 1963*

[40] **Wilson WL, Mullen M, Olley PM, Rabinovitch M**. Hyperoxia-Induced Pulmonary Vascular and Lung Abnormalities in Young Rats and Potential for Recovery. *Pediatric Research, 0031-3998/85/1910-1059*

[41] **Yeh HC, Schum GM, Duggan MT**. Anatomic Models of the Tracheobronchial and Pulmonary Regions of the Rat. *Anat. Rec. (1979) 483-492*

[42] **Yi D, Hayward V**. Skeletonization of Volumetric Angiograms for Display. *Computer Methods in Biomechanics and Biomedical Engineering, 2002 Vol.5(5), pp. 329-341*

[43] **Zheng B, Leader JK, McMurray JM, Park SC, Fuhrman CR, Gur D, Sciurba FC**. Automated detection and quantitative assessment of pulmonary airways depicted on CT images. *Med. Phys. 34(7), July 2007 0094-2405/2007/34(7)/2844/9*

[44] **Zhou YQ, Davidson L, Henkelman RM, Nieman BJ, Foster FS, Yu LX, Chen XJ**. Ultrasound-guided left-ventricular catheterization: a novel method of whole mouse perfusion. *Laboratory Investigation (2004) 84, 385-389*

Tables

Table 1: Summary of Rat Airway & Vascular Tree Measurements

	Airway	Arterial	Venous
# of Segments	562 ± 344	108 ± 43	118 ± 46
# of Generations	20 ± 3	16 ± 4	14 ± 2
θ (total)	53.39 ± 26.82	49.35 ± 26.77	48.46 ± 25.04
θ_{major}	39.20 ± 24.48	45.22 ± 25.95	46.30 ± 21.89
θ_{minor}	59.63 ± 25.39	51.43 ± 26.96	49.32 ± 26.14
Φ	170.72 ± 105.66	167.06 ± 104.13	165.98 ± 102.24
L/D	2.66 ± 1.90	3.69 ± 2.99	3.96 ± 3.60
L/D_{major}	2.47 ± 1.88	3.51 ± 3.03	3.77 ± 3.42
L/D_{minor}	2.76 ± 1.92	3.78 ± 2.96	4.04 ± 3.67
D/D_{parent}	0.80 ± 0.22	0.69 ± 0.26	0.69 ± 0.27
$\%D/D_{parent}<1$	87.80	88.80	90.99
D_{major}/D_{parent}	0.93 ± 0.22	0.72 ± 0.26	0.72 ± 0.28
D_{minor}/D_{parent}	0.75 ± 0.21	0.66 ± 0.26	0.67 ± 0.27
L/L_{parent}	1.02 ± 1.02	1.59 ± 1.89	1.57 ± 1.99
L_{major}/L_{parent}	1.17 ± 1.10	1.73 ± 2.18	1.52 ± 2.00
L_{minor}/L_{parent}	0.94 ± 0.98	1.44 ± 1.52	1.61 ± 1.99

Data expressed as mean ± SD

Table 2: Summary of Mouse Airway & Vascular Tree Measurements

	Airway	Arterial	Venous
# of Segments	206 ± 45	45 ± 257	51 ± 42
# of Generations	16 ± 4	8 ± 4	7 ± 5
θ (total)	45.61 ± 24.27	47.03 ± 25.08	49.19 ± 25.74
θ_{major}	30.42 ± 18.78	24.49 ± 13.88	18.03 ± 15.54
θ_{minor}	51.57 ± 20.52	53.24 ± 20.30	45.82 ± 21.55
Φ	172.45 ± 102.59	154.22 ± 102.91	163.25 ± 103.26
L/D	3.54 ± 2.72	3.94 ± 3.08	3.08 ± 2.12
L/D_{major}	2.54 ± 2.33	2.60 ± 1.97	3.56 ± 1.97
L/D_{minor}	4.18 ± 2.79	7.04 ± 4.23	5.37 ± 3.15
D/D_{parent}	0.72 ± 0.24	0.77 ± 0.28	0.68 ± 0.22
$\%D/D_{parent}<1$	86.81	87.44	93.68
D_{major}/D_{parent}	0.86 ± 0.19	0.91 ± 0.35	0.77 ± 0.39
D_{minor}/D_{parent}	0.60 ± 0.17	0.68 ± 0.20	0.69 ± 0.18
L/L_{parent}	1.26 ± 1.12	2.22 ± 5.05	1.55 ± 3.53
L_{major}/L_{parent}	1.18 ± 0.94	3.40 ± 7.80	2.22 ± 5.56
L_{minor}/L_{parent}	1.30 ± 1.21	1.49 ± 1.64	1.14 ± 0.82

Data expressed as mean ± SD

Table 3: Anatomical Measurements by Diameter Groups for Rats

Diameter Categories		Airways	Arterial	Venous
D1 D ≥ 1mm	# of Segments	24 ± 11	12 ± 6	17 ± 4
	% Segments	4.2	11.2	15.5
	L (mm)	2.72 ± 2.60	3.60 ± 2.29	2.97 ± 0.95
	θ (°)	25.96 ± 17.48	33.14 ± 21.07	35.05 ± 24.72
D2 1 mm > D ≥ 0.75 mm	# of Segments	16 ± 6	16 ± 6	12 ± 6
	% Segments	2.8	14.4	9.9
	L (mm)	1.61 ± 1.58	1.71 ± 1.29	1.78 ± 1.29
	θ (°)	48.96 ± 24.28	49.35 ± 27.02	48.00 ± 27.28
D3 0.75 mm > D ≥ 0.5 mm	# of Segments	35 ± 18	20 ± 8	22 ± 9
	% Segments	6.3	18.2	18.6
	L (mm)	1.16 ± 1.02	1.66 ± 1.25	1.57 ± 1.38
	θ (°)	54.75 ± 25.33	48.78 ± 25.54	50.82 ± 28.14
D4 0.5 mm > D ≥ 0.25 mm	# of Segments	254 ± 112	50 ± 19	49 ± 18
	% Segments	45.2	45.9	41.3
	L (mm)	0.83 ± 0.81	1.71 ± 1.24	1.82 ± 1.55
	θ (°)	57.36 ± 27.84	48.33 ± 25.43	49.04 ± 26.34
D5 D<0.25 mm	# of Segments	233 ± 226	12 ± 11	18 ± 13
	% Segments	41.5	10.3	14.8
	L (mm)	0.53 ± 0.41	0.90 ± 0.51	0.88 ± 0.70
	θ (°)	64.23 ± 28.54	57.50 ± 25.56	60.97 ± 29.12

Data expressed as mean ± SD

Table 4: Anatomical Measurements by Diameter Groups for Mice

Diameter Categories		Airways	Arterial	Venous
D1 D ≥ 0.8 mm	# of Segments	2 ± 1	0	2 ± 1
	% Segments	1.0	-	2.8
	L (mm)	4.71. ± 4.07	-	1.37 ± 1.28
	θ (°)	7.72 ± 9.03	-	19.02 ± 24.65
D2 0.8 mm > D ≥ 0.6 mm	# of Segments	14 ± 3	3 ± 2	4 ± 3
	% Segments	6.8	3.6	4.4
	L (mm)	1.18 ± 1.37	0.57 ± 0.24	1.43 ± 1.08
	θ (°)	20.66 ± 13.79	51.75 ± 18.42	27.48 ± 11.27
D3 0.6 mm > D ≥ 0.4 mm	# of Segments	24 ± 5	6 ± 2	12 ± 10
	% Segments	11.8	10.3	17.8
	L (mm)	0.78 ± 0.82	1.16 ± 0.86	0.88 ± 0.83
	θ (°)	41.72 ± 26.50	42.94 ± 19.69	42.96 ± 22.25
D4 0.4 mm > D ≥ 0.2 mm	# of Segments	68 ± 14	27 ± 8	25 ± 15
	% Segments	33.2	48.9	38.7
	L (mm)	0.90 ± 0.52	1.06 ± 0.77	0.99 ± 0.65
	θ (°)	46.26 ± 22.91	41.24 ± 25.71	47.09 ± 22.60
D5 D<0.2 mm	# of Segments	97 ± 27	21 ± 5	23 ± 10
	% Segments	47.2	37.2	36.4
	L (mm)	0.75 ± 0.50	0.82 ± 0.60	0.55 ± 0.25
	θ (°)	50.50 ± 23.01	55.31 ± 24.06	59.36 ± 27.23

Data expressed as mean ± SD

Table 5: Anatomical Measurements by Generation for Rats

Generation	Airway		Arterial		Venous	
	Diameter (mm)	Length (mm)	Diameter (mm)	Length (mm)	Diameter (mm)	Length (mm)
0	1.950 ± 0.100	9.556 ± 2.223	0.944 ± 0.232	0.929 ± 0.368	1.797 ± 0.338	1.812 ± 0.384
1	1.539 ± 0.284	8.338 ± 3.112	1.018 ± 0.247	6.040 ± 1.566	1.502 ± 0.655	2.722 ± 1.628
2	1.325 ± 0.589	3.284 ± 1.130	0.883 ± 0.340	1.430 ± 0.594	1.140 ± 0.558	2.229 ± 1.570
3	0.995 ± 0.611	1.863 ± 1.221	0.688 ± 0.340	1.658 ± 1.113	0.941 ± 0.475	2.689 ± 1.787
4	0.671 ± 0.476	1.737 ± 1.208	0.597 ± 0.363	1.560 ± 1.143	0.751 ± 0.460	2.168 ± 1.574
5	0.469 ± 0.337	1.342 ± 1.041	0.570 ± 0.341	1.541 ± 1.062	0.609 ± 0.403	1.782 ± 1.393
6	0.386 ± 0.273	1.037 ± 0.709	0.574 ± 0.326	1.882 ± 1.426	0.552 ± 0.330	1.905 ± 1.385
7	0.358 ± 0.237	0.884 ± 0.755	0.513 ± 0.298	1.617 ± 1.250	0.504 ± 0.318	1.574 ± 1.320
8	0.356 ± 0.216	0.892 ± 0.783	0.521 ± 0.269	1.733 ± 1.377	0.470 ± 0.277	1.852 ± 1.886
9	0.348 ± 0.210	0.867 ± 0.593	0.494 ± 0.256	1.752 ± 1.744	0.505 ± 0.253	1.483 ± 1.418
10	0.328 ± 0.183	0.785 ± 0.627	0.478 ± 0.235	1.473 ± 1.106	0.445 ± 0.216	1.712 ± 1.301
11	0.324 ± 0.171	0.762 ± 0.606	0.556 ± 0.233	1.401 ± 0.700	0.448 ± 0.200	1.619 ± 1.419
12	0.319 ± 0.159	0.804 ± 0.544	0.490 ± 0.242	1.653 ± 1.184	0.408 ± 0.187	1.512 ± 1.174
13	0.309 ± 0.141	0.738 ± 0.478	0.508 ± 0.221	1.705 ± 0.986	0.400 ± 0.132	1.730 ± 1.091
14	0.305 ± 0.132	0.715 ± 0.507	0.425 ± 0.222	1.241 ± 0.621	0.283 ± 0.088	1.169 ± 0.983
15	0.304 ± 0.130	0.696 ± 0.457	0.468 ± 0.207	1.582 ± 0.866	-	-
16	0.307 ± 0.129	0.786 ± 0.652	0.373 ± 0.185	1.076 ± 0.597	-	-
17	0.288 ± 0.111	0.746 ± 0.495	-	-	-	-
18	0.283 ± 0.090	0.731 ± 0.478	-	-	-	-
19	0.266 ± 0.048	0.821 ± 0.688	-	-	-	-
20	0.256 ± 0.047	0.654 ± 0.539	-	-	-	-

Data expressed as mean ± SD

Table 6: Anatomical Measurements by Generation for Mice

Generation	Airway		Arterial		Venous	
	Diameter (mm)	Length (mm)	Diameter (mm)	Length (mm)	Diameter (mm)	Length (mm)
0	0.896 ± 0.099	7.617 ± 3.744	0.267 ± 0.038	0.188 ± 0.166	0.816 ± 0.279	0.421 ± 0.308
1	0.662 ± 0.102	5.061 ± 1.103	0.390 ± 0.112	2.883 ± 0.558	0.689 ± 0.198	2.649 ± 1.011
2	0.575 ± 0.202	1.455 ± 0.596	0.423 ± 0.179	1.295 ± 0.913	0.462 ± 0.183	1.842 ± 1.082
3	0.426 ± 0.194	0.967 ± 0.554	0.310 ± 0.154	1.104 ± 0.607	0.339 ± 0.160	1.090 ± 0.525
4	0.353 ± 0.165	0.843 ± 0.530	0.283 ± 0.132	0.808 ± 0.628	0.315 ± 0.134	0.744 ± 0.406
5	0.299 ± 0.151	0.877 ± 0.613	0.283 ± 0.117	0.901 ± 0.464	0.275 ± 0.122	0.643 ± 0.313
6	0.288 ± 0.155	0.778 ± 0.450	0.238 ± 0.078	0.948 ± 0.688	0.268 ± 0.120	0.654 ± 0.313
7	0.260 ± 0.131	0.769 ± 0.482	0.220 ± 0.061	0.625 ± 0.384	0.262 ± 0.104	0.616 ± 0.322
8	0.260 ± 0.133	0.792 ± 0.471	0.206 ± 0.053	0.699 ± 0.476	-	-
9	0.260 ± 0.134	0.721 ± 0.423	-	-	-	-
10	0.243 ± 0.124	0.704 ± 0.434	-	-	-	-
11	0.264 ± 0.125	0.802 ± 0.552	-	-	-	-
12	0.243 ± 0.101	0.740 ± 0.519	-	-	-	-
13	0.208 ± 0.068	0.798 ± 0.491	-	-	-	-
14	0.213 ± 0.062	0.619 ± 0.302	-	-	-	-
15	0.196 ± 0.052	0.741 ± 0.330	-	-	-	-
16	0.169 ± 0.010	0.665 ± 0.412	-	-	-	-

Data expressed as mean ± SD

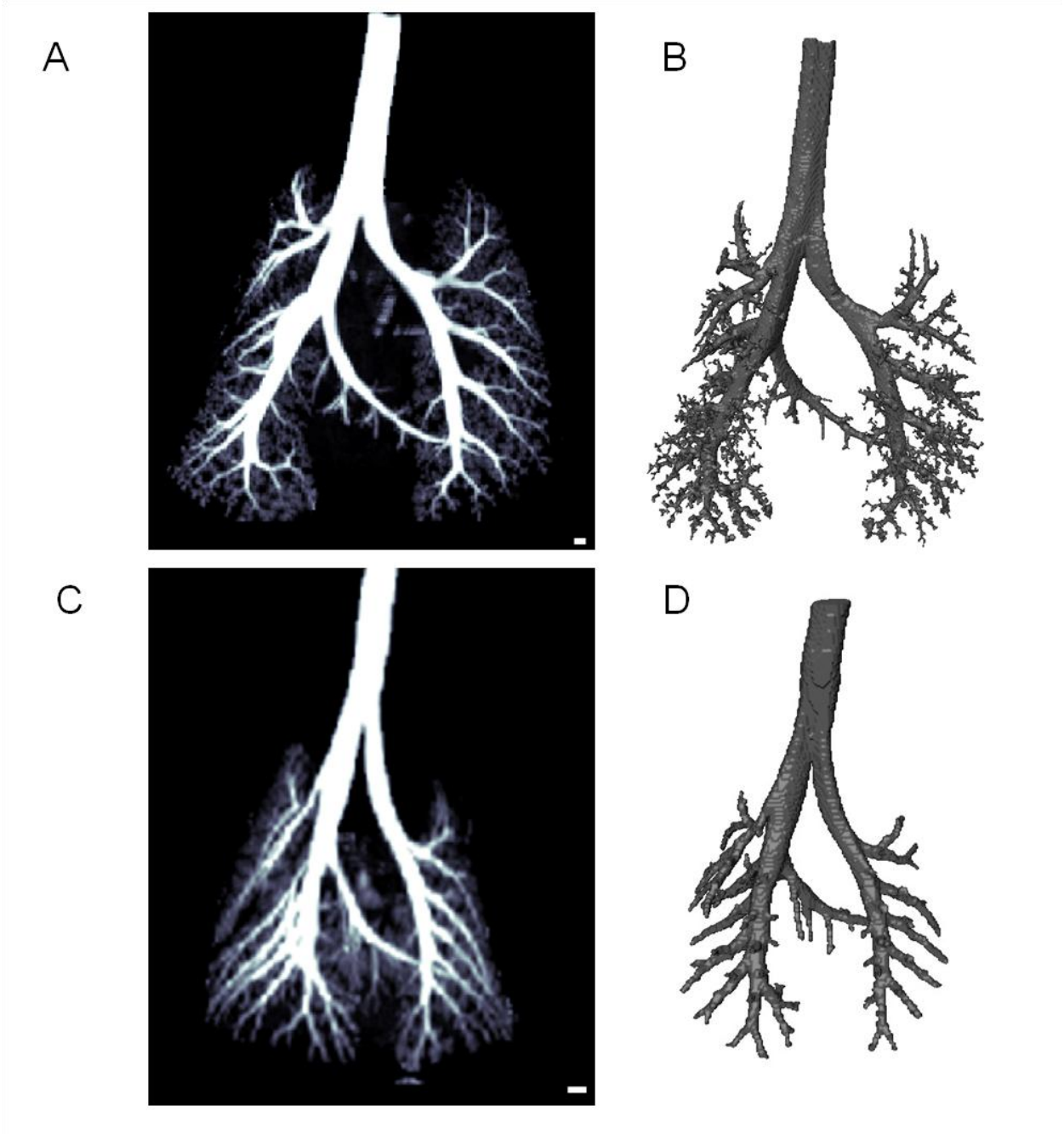

FIGURE 1: Airway visualization using contrast-enhanced CT (Microfil MV-122, *Flowtech Inc*.); (A) Maximum intensity projection from the rat, (B) segmented airway tree from the rat, (C) Maximum intensity projection from the mouse, (D) segmented airway tree from the mouse. Scale bars are 1 mm.

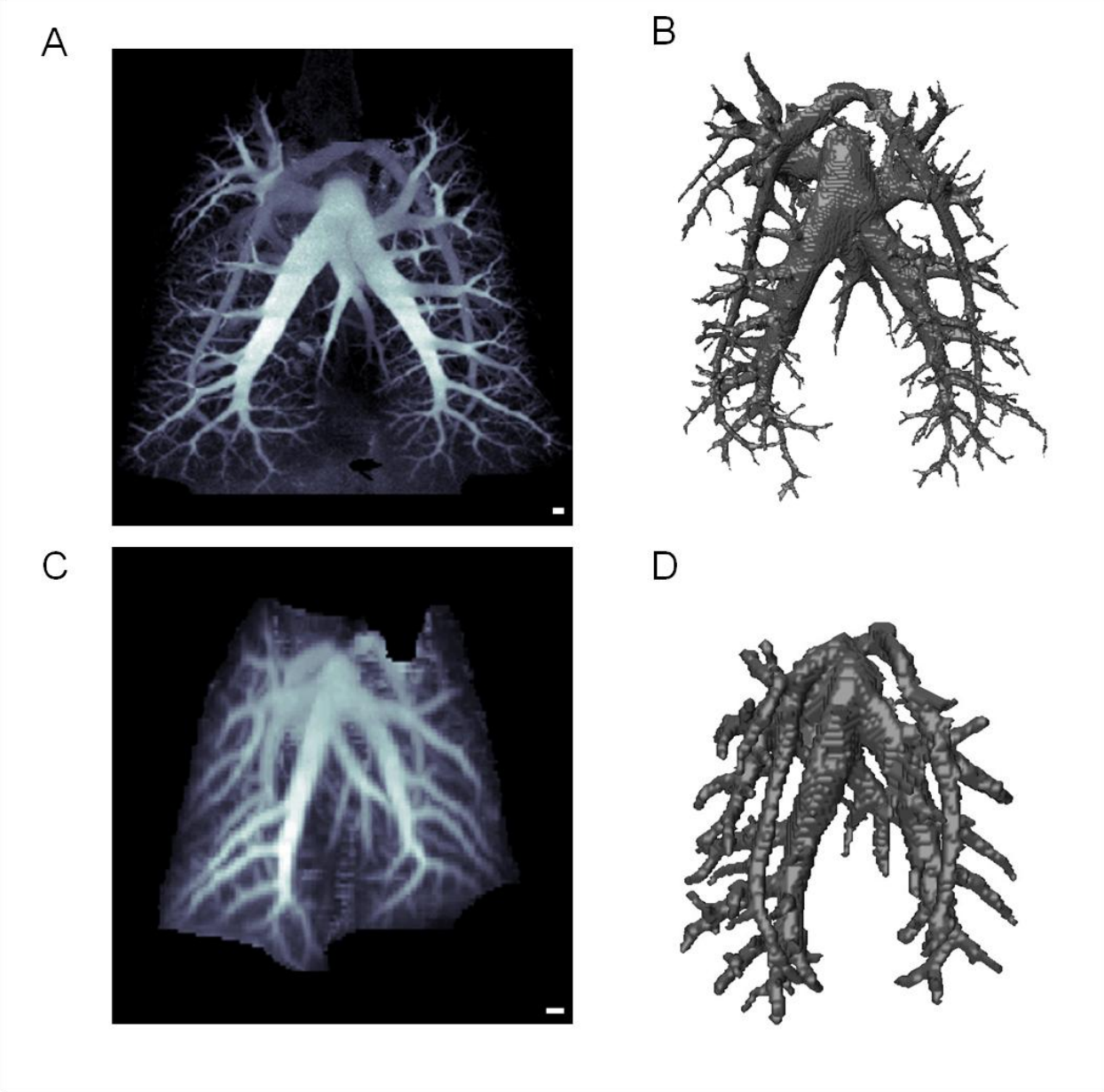

FIGURE 2: Vascular visualization using contrast-enhanced CT (Omnipaque, *GE Healthcare*); (A) Maximum intensity projection from the rat, (B) segmented vascular trees from the rat, (C) Maximum intensity projection from the mouse, (D) segmented vascular trees from the mouse. Scale bars are 1 mm.

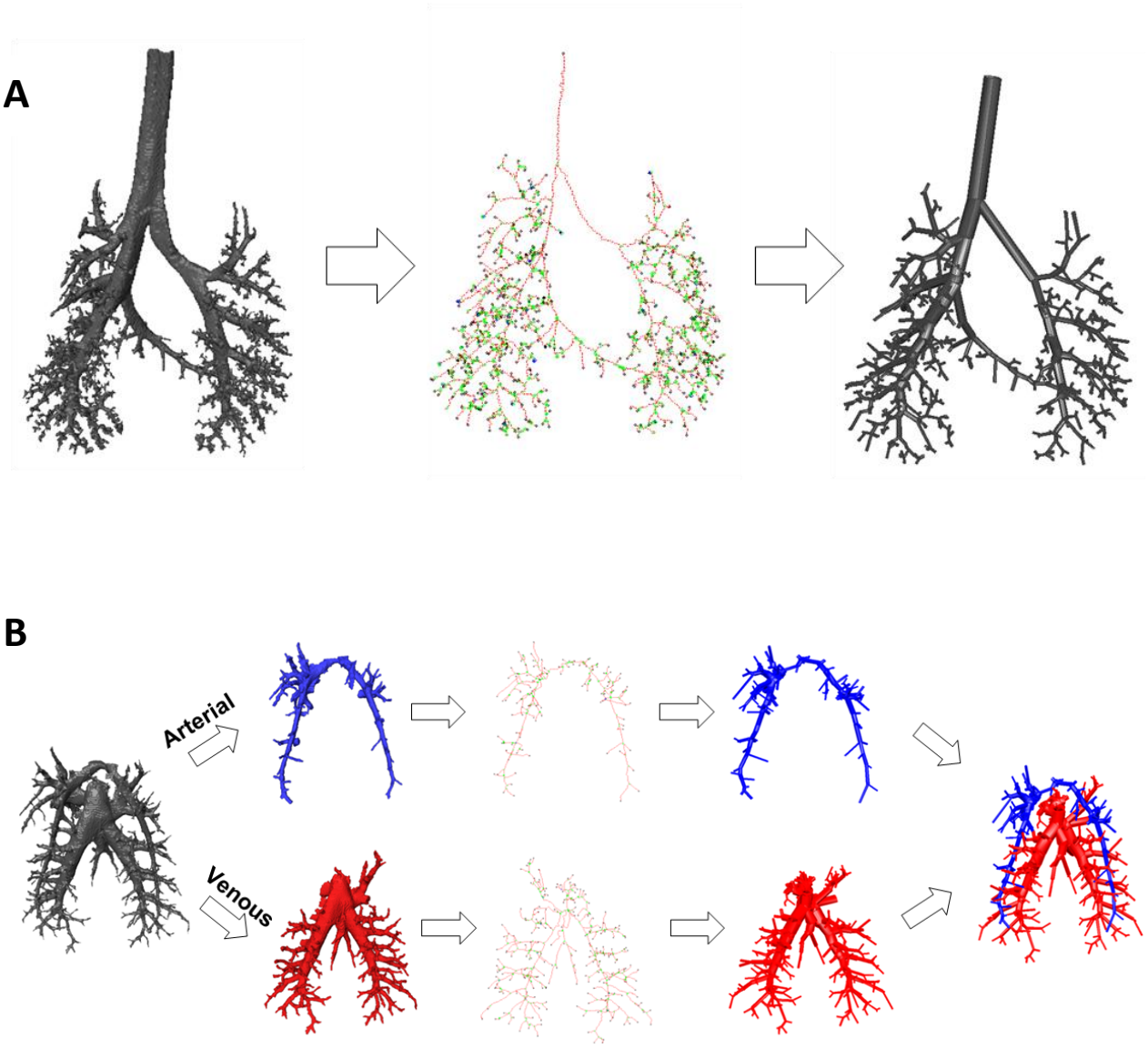

FIGURE 3: (A) Creation of individual airway model; from left to right, segmentation, coded centre-line, bifurcation model (shown for rat). (B) Creation of individual vascular models; from left to right, segmentation, vascular separation, coded-centre-lines, bifurcation models and fused vascular model (shown for rat).

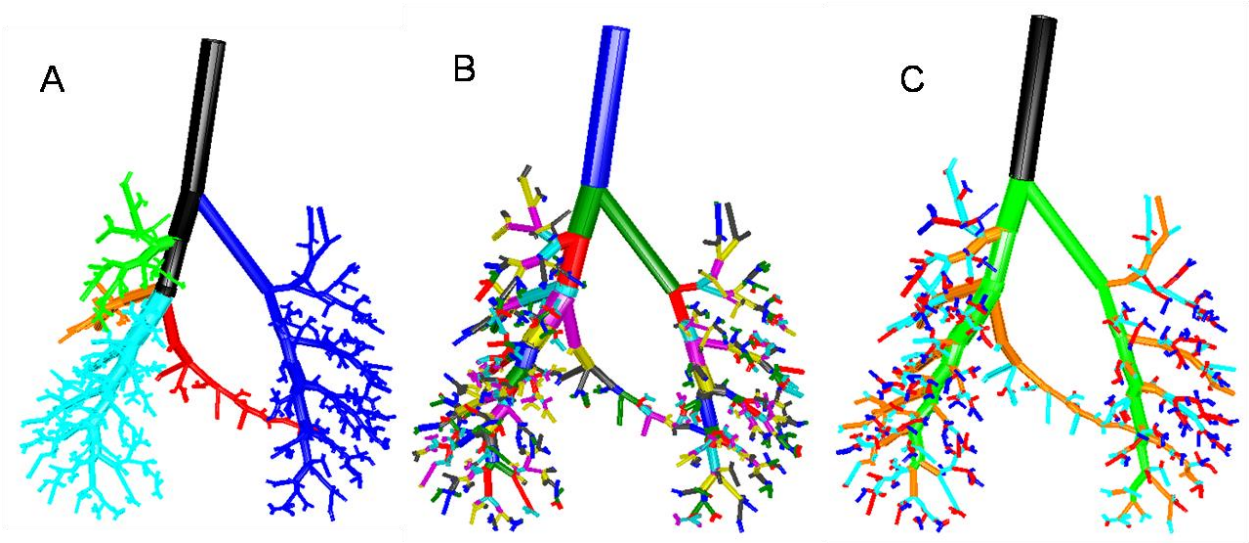

FIGURE 4: Classification of Individual Airway Model. A) Lobes, B) Generation, C) Order. Each colour represents a different tree hierarchy (shown for rat)

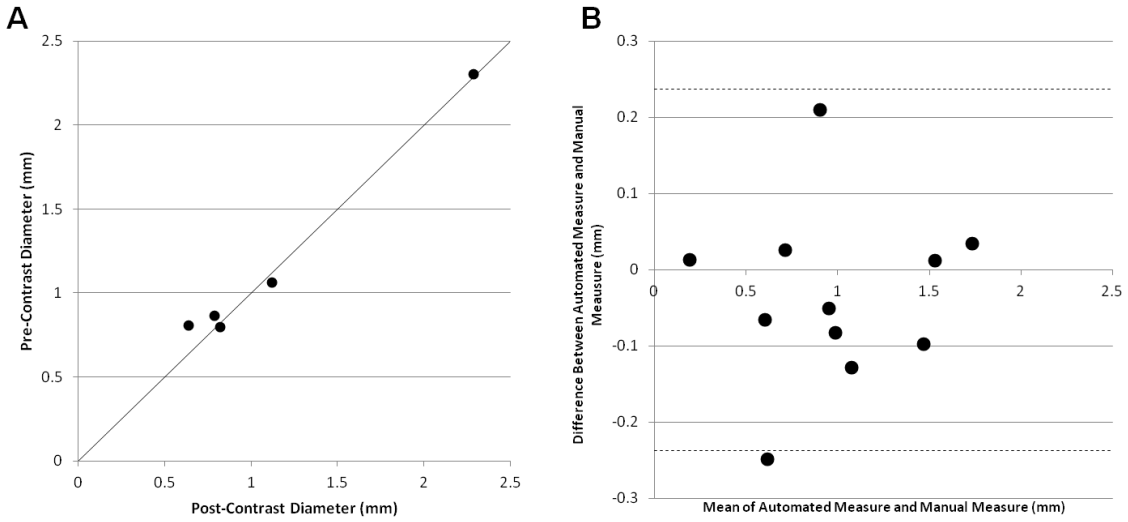

FIGURE 5: A) Pre-contrast diameter measurements versus post-contrast diameter measurements. The line represents the line of unity (x=y) B) Bland-Altman Plot of airway diameters as measured by automated measurements compared to the standard measurements taken by 3 individuals directly from contrast-enhanced CTs.

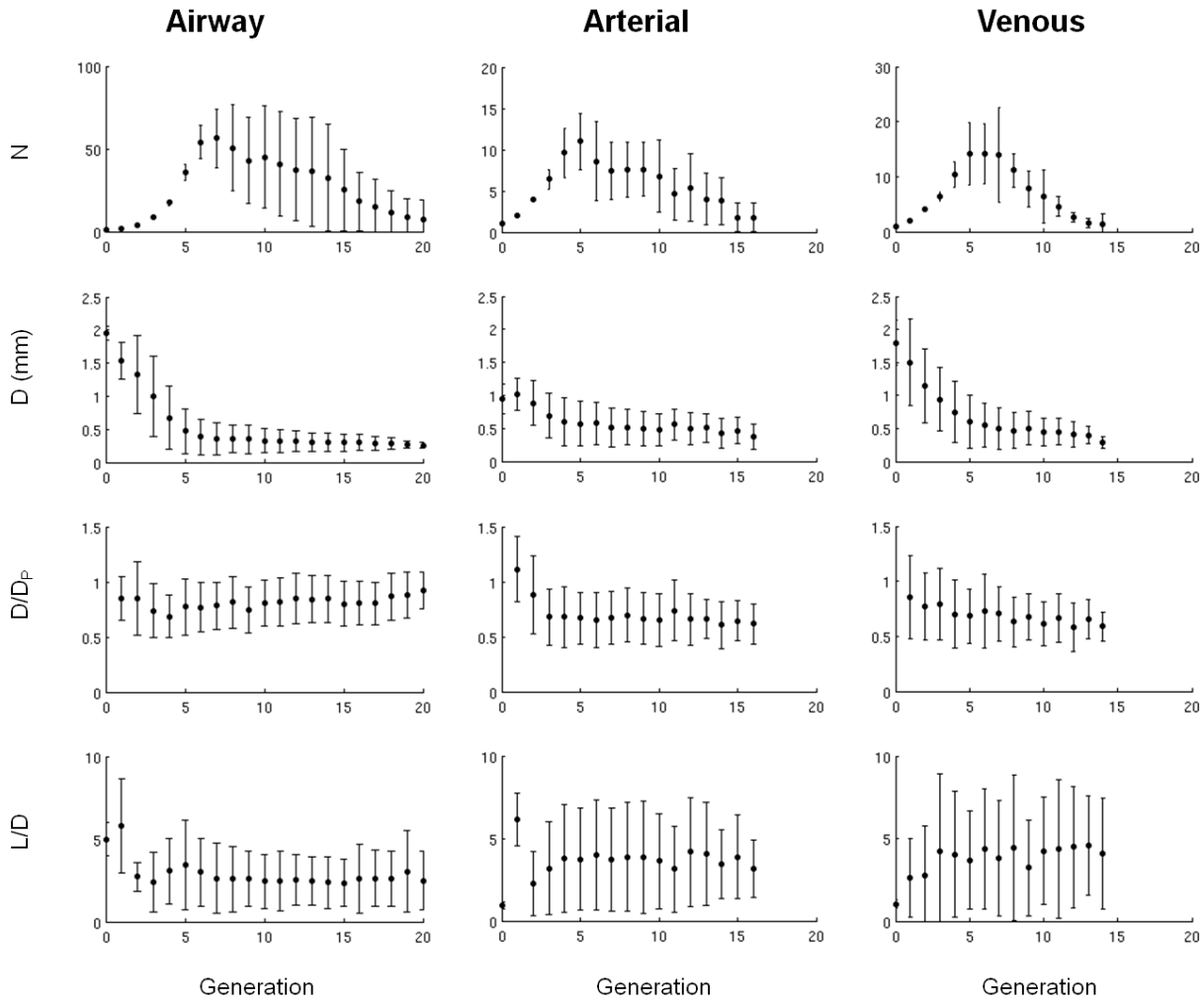

FIGURE 6: Airway, arterial, and venous data for the Sprague-Dawley rat. Parameters include number of airways (N), diameter (D), the ratio of diameter to parent diameter (D/D_P), and the ratio of length to diameter (L/D). Error bars representing the standard deviation are included and contain both inter- and intra-subject variability. Note: D/D_P not defined for generation 0.

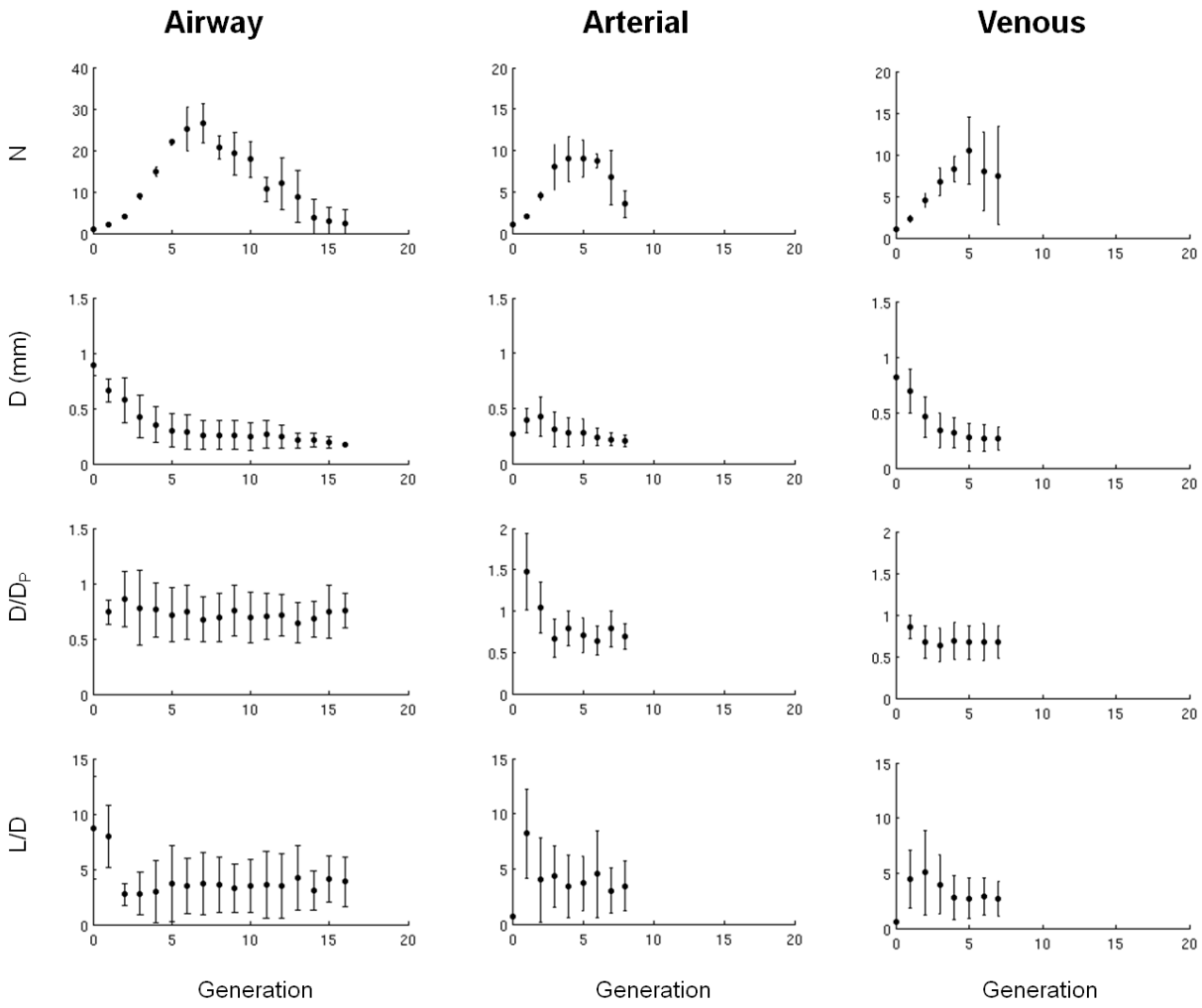

FIGURE 7: Airway, arterial, and venous data for the BALB/c mouse. Parameters include number of airways (N), diameter (D), the ratio of diameter to parent diameter (D/D_P), and the ratio of length to diameter (L/D). Error bars representing the standard deviation are included and contain both inter- and intra-subject variability. Note: D/D_P not defined for generation 0.

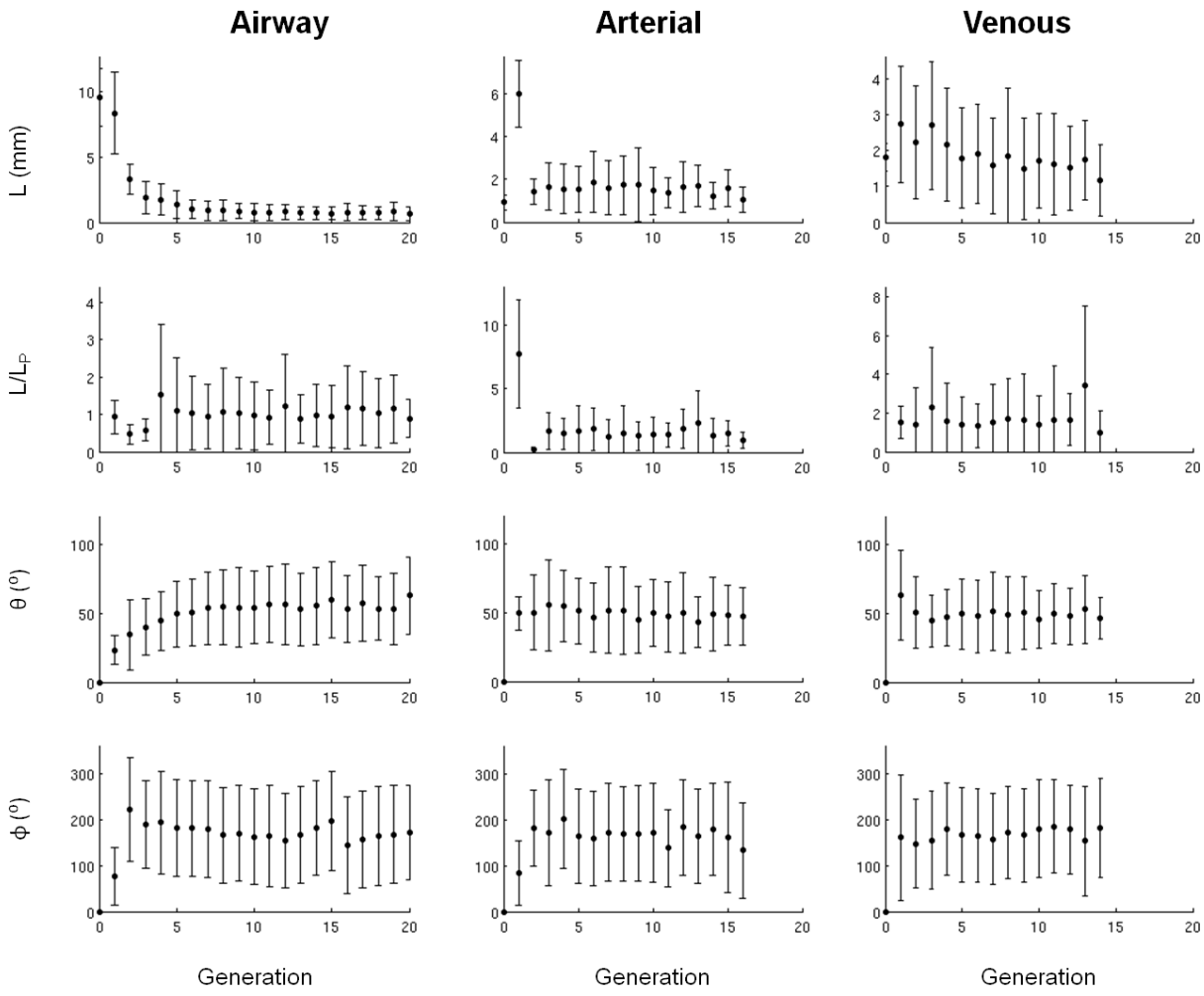

SUPPLEMENTAL FIGURE 1: Airway, arterial, and venous data for the Sprague-Dawley rat. Additional parameters include length (L), the ratio of length to parent length (L/L_P), the branching angle theta (θ), and the branching angle phi (φ). Error bars representing the standard deviation are included and contain both inter- and intra-subject variability. Note: L/L_P not defined for generation 0.

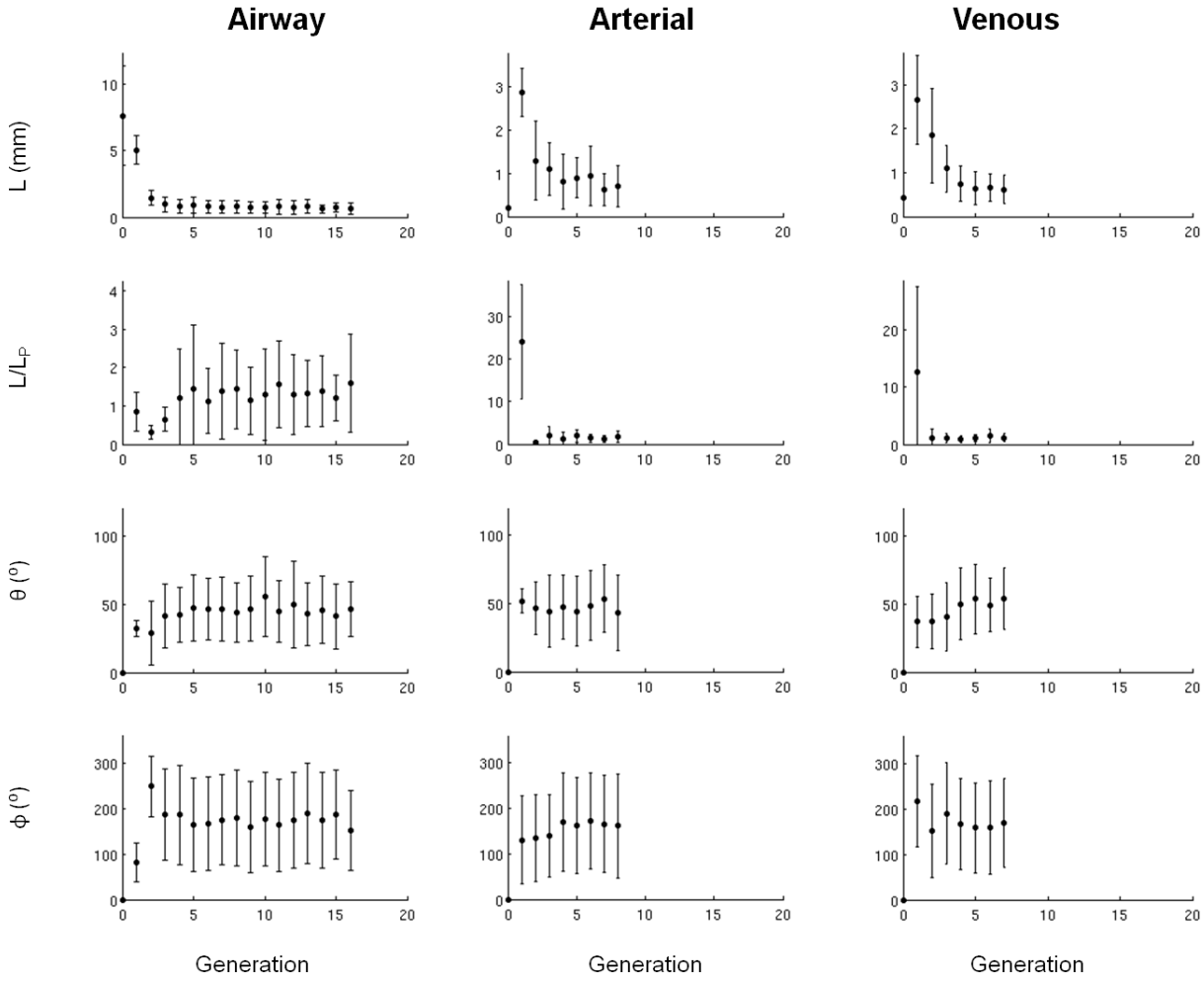

SUPPLEMENTAL FIGURE 2: Airway, arterial, and venous data for the BALB/c mouse. Additional parameters include length (L), the ratio of length to parent length (L/L_P), the branching angle theta (θ), and the branching angle phi (φ). Error bars representing the standard deviation are included and contain both inter- and intra-subject variability. Note: L/L_P not defined for generation 0.

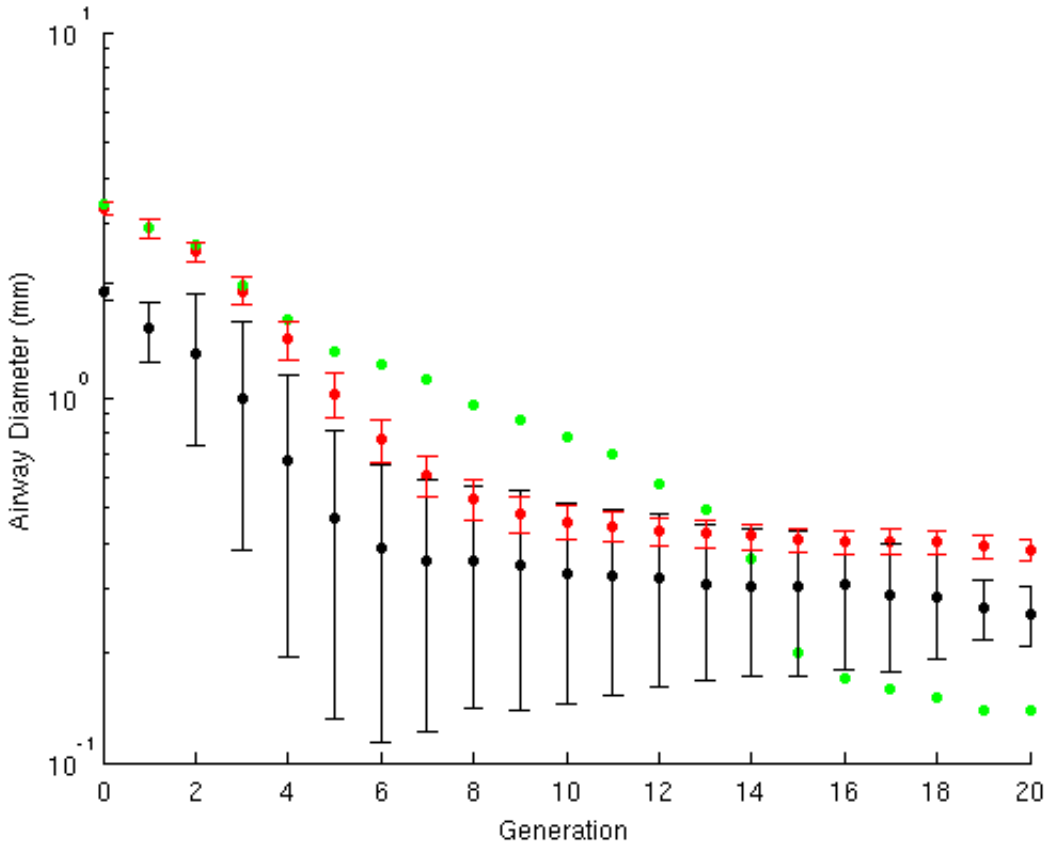

SUPPLEMENTAL FIGURE 3: Comparison of airway diameter measurements in rats between this study (Sprague-Dawley) and those of Lee et al. (Sprague-Dawley) and Yeh et al. (Wister). NOTE: The rats used in the Lee study were older and larger than the rats used in this study, which we believe explains their larger measurements and smaller variation.

3 Development of a Mathematical Rodent Lung Model for Image Analysis and Simulation of Respiratory Diseases

3.1 Synopsis

The purpose of this section was to develop a mathematical lung model which can be applied to un-enhanced CTs of the rodent lung. A critical step towards this end involved determining what parameters from the rodent lung database were of importance and which features of a specific CT would serve as a starting point for the generation of a lung model. The model begins with the visible airways and continuously generates daughter airways based on the location of lung boundaries and using a fractal-based branching algorithm. Arterial and venous segments are generated to follow the growing airway tree. At each bifurcation the diameter decreases according to rules established using the anatomical database. Branching ceases when the diameter decreases below a critical size, based on the average diameter of terminal bronchioles.

3.2 Contribution to Manuscript

As primary author, I, WB Counter, designed and developed the model and did the analysis. I wrote all the software and the manuscript. RG Rhem provided expertise in Matlab; TH Farncombe provided expertise in imaging physics and edited the manuscript; NR Labiris contributed to study design, provided financial support, expertise in lung anatomy/physiology, and edited the manuscript.

3.3 Manuscript

References are listed in alphabetical order using the last name of the first author.

Development of a Mathematical Rodent Lung Model for Image Analysis and Simulation of Respiratory Diseases

WB Counter[1,2], R Rhem[1], TH Farncombe[3,4], NR Labiris[1,4]

[1] Department of Medicine, McMaster University; [2] Department of Medical Physics, McMaster University; [3] Department of Radiology, McMaster University; [4] Department of Nuclear Medicine, Hamilton Health Sciences, McMaster University, Hamilton, Ontario, Canada

Author Contributions:
WBC created the lung model, wrote the software, and wrote the manuscript; RGR provided expertise in Matlab; THF provided imaging expertise, and editing of the manuscript; NRL provided study concept/design, expertise in lung structure/physiology, provided financial support, and editing of manuscript

Financial Support: N.R. Labiris holds an Internal Department of Medicine Career Award

Running Head: Development of a Virtual Rodent Lung

Word Count: 3498

Correspondence: Name: Dr. Renée Labiris
Mailing Address: 1280 Main St. W., Hamilton, Ontario, L8S 4K1, Health Science Centre, rm. 1V11
Phone: 905 521-2100 ext. 75657
Fax: 905 546-1125
Email Address: labir@mcmaster.ca

Abstract:

Imaging of small animals has vastly improved the ability of pulmonary researchers to study lung disease and the efficacy of inhaled pharmaceuticals. A mathematical model of the rodent lung would increase our understanding of structure-function relationships within the lung and facilitate the analysis of anatomical and functional images. The objectives of developing this lung model were: 1) to extend the airways and vasculature in un-enhanced CT images of small animals beyond the resolution of the scanner so that biological processes or structural changes can be mapped to specific lung regions, and 2) to simulate respiratory diseases, including COPD, asthma, and pulmonary hypertension, by altering various structural parameters such as airway and vascular diameters. Such a model would reduce the need to conduct animal experiments to address certain scientific questions. Based partially on measurements from contrast-enhanced CTs, this virtual lung can be applied to un-enhanced CT images and can be used in image analysis. The airway tree was generated by employing a fractal-based branching/volume-filling algorithm within individual lobe boundaries. Arterial and venous components were then added alongside the generated airways and within the lobe boundaries to form a pulmonary model containing both airways and vasculature. A detailed mathematical rodent lung model would greatly facilitate the analysis of anatomical and functional images and allow the simulation of various respiratory diseases.

Key Words: Pulmonary, Airways, Vasculature, Lung, Mathematical Model, Fractal, Rodent, Preclinical Imaging, Disease simulation

Introduction:

Animal models of disease play an important role in enhancing our understanding of the mechanism of disease and enable us to screen novel drug compounds for efficacy. However, the endpoint is usually histology after necropsy providing a snapshot of the disease state at one timepoint. Such results tell us little about disease progression, about events prior to initiation of therapy, or potential effects after a longer treatment period. Small animal imaging offers the advantage of a non-invasive, longitudinal evaluation of biological processes such as inflammation, infection, ventilation, perfusion, and receptor occupancy without the need for serial sacrificing. However, since the technology is relatively new, methods of analyzing and relating functional or structural abnormalities detected with imaging to location in the lung has not been extensively developed.

Lung models can either be anatomical, created directly from the imaging data, or mathematical, using a series of repeatable rules to generate branching structures [15,20]. Anatomical models, unlike mathematical models, are specific to the individual being imaged and only contain structures that are visible within the image. In contrast, mathematical models are not specific to individual animals but can predict the location of lung anatomy beyond the resolution limits of most small animal CT systems.

Three-dimensional mathematical models of the human airways have been created by various research groups. Most of these models make the assumption that each segment is a circular, rigid tube with a constant diameter. Kitaoka et al. [7] have created a mathematical model of the human airway tree in order to study structure-function relationships within the lung. Their model used a series of branching rules to successively divide an initial bounding volume into smaller and smaller regions. It assumes dichotomous branching and ensures that the terminal segments are distributed evenly throughout the lung volume. In a subsequent paper [8], vascular trees were added to the previously generated airway tree to create a full human lung model that was then used to simulate CT images in a process known as virtual imaging. Martonen et al. [4,11,16,17] created a mathematical model of the human airway network to relate SPECT deposition patterns to real lung structures. Like that of Kitaoka, their model generated a branching structure within a bounding volume. Its uniform and regular appearance can be attributed to several factors; constant branching angles, a constant rotation plane, and a highly simplified lung boundary. Tawhai et al. [2,3,18,19] have also created an airway model that generates a branching structure within a bounding volume. The bounding volume, derived from MRI data, was separated into five distinct regions that represent the five lobes of the human lungs. Each lobe boundary was then filled with a set of randomly distributed grid points. The centre of mass of the points was calculated, and the line connecting the starting point with the centre of mass was used to divide the set of grid

points into two new subsets of points. The process is repeated until only one grid point is left within each subset. Diameters were then randomly assigned using data collected from Horsfield et al. in 1981. It has been noted that the use of evenly spaced grid-points results in a branched structure that reflects the shape of the bounding volume instead of the distribution of the random points [18]. Segars et al. [5] used a modified Kitaoka algorithm to extend the airways in their NCAT phantom beyond what they were able to segment from human HRCT datasets. Like the Kitaoka algorithm, the individual lobes were used as boundaries and diameters were assigned using a length to diameter relationship (L/D=3). Transverse slices of their model were then compared to actual HRCT slices and found to be similar to the actual imaging data. Wexler et al. [9,10,21] introduced a mathematical model of airway development based on the presence of several virtual morphogen sources within the bounding lung volume. These sources produce morphogen gradients; airways at sites of high morphogen concentration developed normally while airways with low morphogen concentrations failed to do so.

To our knowledge, no lung model including both the airways and vasculature exists for rodents. Since the majority of preclinical studies use rodents to investigate lung disease, a rodent-specific lung model would be useful in the analysis of anatomical and functional imaging data. We have developed a mathematical rodent lung model that combines boundary information from a specific CT image with previously acquired measurements of airways and pulmonary vasculature from contrast-enhanced CT images [WBC, paper 1] and a branching/volume-filling algorithm. Such a model provides detailed information regarding lung anatomy that can provide context to both anatomical and functional images and provide insight into the relation between structure and function in the lung. Furthermore, the ability to simulate disease scenarios with the model could reduce the need for animal studies.

Materials and Methods:

In previous work we measured the lengths, diameters, and branching angles of both the airways and pulmonary vasculature of Sprague-Dawley rats (200-225g) and BALB/c mice (20-25g) using contrast-enhanced micro-CT images [WBC, paper 1]. Briefly, the airways and vasculature were segmented from the contrast-enhanced images, converted into networks of cylindrical segments for measurement, and then analyzed as a function of generation number to create an anatomical database. In order to create a lung model that could be applied to different sizes of animals, select pieces of data from an anatomical rodent database were combined with image-specific information such as the lung boundary and location of the conducting airways from an individual animal's un-

enhanced CT image. Both boundaries and airways were acquired manually using Amira 4.1.1 (*Computer Systems Inc., San Diego, CA)*. The lung boundary was divided into 5 individual lobes, each of which served as the boundary for a contained fractal-based branching algorithm. Diameters were assigned to this airway tree using the segmented conducting airways and rules that were established from the database for assigning the diameter of a segment based on the diameter of its parent segment. Arterial and venous segments were then added alongside the airway tree in a manner that avoided possible intersection of segments to create a virtual rodent lung model containing airway, arterial, and venous components.

Division of the Lung into Individual Lobes

Generating a contained branching structure required a bounding volume. In order to create a realistic lung model each lobe of the lung was used as a separate boundary to contain a branching structure. Separation of a lung volume into the individual lobes is not a simple task in humans [12,22]. It is even more of a problem in images of small animals, where the fissures dividing the lobes are often absent due to resolution limitations and partial volume effects. The process begins with a manual segmentation of the lung region from a CT image, acquired using Amira. To separate this lung into individual lobes in the rat we utilized a coded segmentation of the conducting airways. In this coded segmentation, the conducting airways feeding each lobe were assigned different values. Voxels in the lung segmentation were then assigned to one of the five lobes if they were adjacent to any voxels from their respective coded airway. The process continued until all the voxels of the lung segmentation were assigned to one of the five lobes. Lobe separation was performed in both contrast-enhanced and un-enhanced CT images of the lung. Figure 1 shows the results of this process for a representative contrast-enhanced CT image of the Sprague-Dawley rat lung. The performance of this lobe-dividing algorithm was assessed by comparing its results with a lung that was manually divided into individual lobes using Amira 4.1.1.

Airway Generating Algorithm

Defining the individual lobe boundaries allowed airways to be generated within each lobe using a fractal-based branching/volume-dividing algorithm. The algorithm is similar to that developed by Tawhai et al. [18,19] for airway branching in the human lung. Each bounding volume requires an entry point, or root segment, where the branching process begins. The root segment is essentially the main airway supplying each lobe. They were derived from the manually segmented airway tree mentioned above.

Initially, each lobe boundary was filled with an evenly distributed set of grid points which represented the respiratory centres, or terminal bronchioles, of the lung. The centre of mass was calculated by averaging the coordinates (x,y,z) of the set of grid points. The grid points were then divided into two sets using a vector connecting the entry point with the centre of mass. A plane of random orientation which contained the aforementioned vector was used to divide the grid points. Once the grid points were divided, the centre of mass of each set was calculated. A line was then drawn from the starting point a fraction of the way to the new centre of mass. The fraction, known as the branching fraction, was initially set at 0.4 (40%) [18] but was allowed to fluctuate slightly around this value using a normal distribution with a mean of 0 and standard deviation of 0.1. The initial set of grid points was continuously divided into smaller and smaller subsets until only a single grid point remained in each set. A two-dimensional example is illustrated in Figure 2A following 3 iterations and 553 iterations. The 3-dimensional algorithm was repeated for each lobe to generate an anatomically realistic airway structure. As input, the algorithm used the boundary of each lobe as well as the root segment supplying that lobe. The input and output of the three-dimensional algorithm are shown in figure 2B, where the dots represent the bounding volume of each lobe and not the set of grid points within.

Vascular Tracing Algorithm

The spatial orientation between the airways and pulmonary vasculature, derived from contrast-enhanced CT images, is shown in figure 3A. Although the airways were generated in a pseudo-random manner within the lung volume, the corresponding generated vascular segments followed the airways to ensure that each respiratory centre was supplied by both an arterial and venous segment. For each segment in the generated airway tree, the algorithm added both an arterial and venous segment. The vascular segment began where its parent segment left off and was grown alongside its corresponding airway segment. The two are not parallel however because the vascular segments get closer to the airway segments as their diameters decrease. Using this method, it was possible for intersections to occur when the airway and vascular segments are both in the same plane as the daughter airway segments. To avoid these points of intersection, the algorithm ensured that the vector connecting the airway and vascular endpoints was perpendicular to the plane containing the two daughter airway segments. This was accomplished by positioning the vascular endpoint at the location which minimized the rotation of the vascular segment around its corresponding airway segment. Figure 3B shows both an orientation that will intersect another segment and an orientation that will not. For every bifurcation, two possible vascular endpoints exist; one on each side of the bifurcation plane. One of these potential endpoints will be the arterial

endpoint and the other will be the venous endpoint. The algorithm selected the orientation which minimized the rotation between the vector which connects the starting points and the vector which connects the endpoints. Results of the vascular tracing algorithm are displayed for both a single vascular tree as well as both the arterial and venous trees (Figure 3C-D).

Airway and Vascular Diameter Assignment

The airway-generating algorithm detailed above used the boundary of each lobe to generate a branching structure which was evenly distributed within that boundary. The branching angles and segment lengths in the model were a result of this algorithm. Segment diameters, on the other hand, were assigned using the relationship between the ratio of segment diameter to parent diameter (D/D_P) and segment branching angle (theta, θ). From an anatomical rodent lung database [WBC, paper 1], it was observed that D/D_P was dependant on the branching angle of the segments. Segments which continued in roughly the same direction as the parent had diameters very close to that of the parent segment where segments which branched off at larger angles had smaller diameters compared to their parents. A graph of D/D_P versus theta (θ) is shown in Figure 4 and from it the following relationship was established:

$$D/D_P = 0.852 - 0.001*\theta \qquad \text{[Equation 1]}$$

Diameters were therefore assigned using the diameter of the parent segment and the angle theta at which the branch deviated from its parent. Arterial and venous segment diameters were defined using the diameter of their corresponding airway. Relationships between airway and vascular diameters have been investigated by several authors for both human [1] and canine [6] lungs. Based on manual measurements from CTs the narrower arterial segments were assigned a diameter equal to 80% of the airway diameter while the larger venous segments were assigned a diameter equal to 110% of the airway diameter. These values were determined experimentally by comparing adjacent airway, arterial, and venous diameters from both enhanced and un-enhanced CT images.

Model Validation

Several of the preceding steps required validation. The results of the automated lobe-dividing algorithm, for both enhanced and un-enhanced images, were compared to a manual lobe segmentation which represented the gold standard. The percent of voxels from the automated algorithm which were correctly assigned based on the gold standard

was used as measure of the algorithms efficacy. Lobe separation in contrast-enhanced images was found to agree with the gold standard to within 5%. Lobe separation in un-enhanced images was found to agree with the gold standard to within 15%. The performance of the lung model was assessed by comparing it to a database of anatomical measurements obtained from contrast-enhanced CTs. A second database was generated pseudo-randomly by generating the mathematical model five times within a representative lobe-divided lung boundary. Airway, arterial, and venous data was compared together or separated into five distinct diameter groupings using an unpaired T test.

Results:

A mathematical model has been developed for the rodent lung that contains both the airways and vasculature [Figure 5]. The model uses a fractal-based branching/volume-filling algorithm to generate an airway tree within a lobe-divided lung boundary. Diameters were assigned based on rules established from a previously collected anatomical database that relate a segment's diameter to its branching angle (θ) and the diameter of its parent. Arterial and venous segments were then grown alongside the previously generated airway tree and assigned diameters based on the diameter of their corresponding airways. The model contains segments with diameters ranging from 0.02 mm to 2 mm over 20 generations.

The model was validated by comparing the average parameter values measured from the contrast-enhanced CT images with those of the model for airway, arterial, and venous data (Table 1). The generated model data was not statistically different from the measured data for each of the three pulmonary components. Additionally, segments were classified as either major or minor based on their relative diameters. As expected minor segments branch off at higher angles (θ) and possess diameters that are a smaller percentage of their parent diameter (D/D_P) than that of the major segments.

Additionally, segments were grouped into diameter-based categories for comparison. Segments ranged from category D1 ($D \geq 1$mm) to category D5 ($D < 0.25$mm). For each of the five diameter categories the average diameter, length, and branching angles of the generated model were plotted against those of the measured anatomical data (Figure 6). No major statistical differences were found between any of the three pulmonary components. Standard deviations were also found to be similar between the generated model and the anatomical data. Further validation of the model has been performed and is shown elsewhere [Refer to Chapter 4 – Mathematical Rodent Lung Model Validation].

In Figure 7, the model is shown alongside of the anatomical models created from the contrast-enhanced CTs for comparison. Besides the fact that the mathematical model contains more than ten times the number of segments, as expected, the two are similar. The mathematical model allows the airway and vascular components of the pulmonary system to be combined in an anatomically acceptable way. The model extends the airway and vascular structures to contain segments that are an order of magnitude smaller than what could be resolved, segmented, and measured from the contrast enhanced CTs.

Application of the Virtual Lung

The model can easily be adjusted for applications in other species of small animals. Figure 8 demonstrates the procedure for an un-enhanced CT image of a BALB/C mouse. After segmenting the lung boundary and visible airways from the image, the lung is divided into lobes, airways are grown to fill each lobe, and finally arterial and venous segments are grown alongside the airways. This allows us to predict the approximate location of the pulmonary airways and vasculature within micro-CT images where usually only the first several generations of airways are visible.

Discussion:

A mathematical lung model that includes both the airways and pulmonary vasculature has been developed for the rodent lung and allows lung anatomy to be predicted within un-enhanced CT images [Figure 8]. Beginning with segmentations of the lung boundaries and of the visible airways from micro-CT images, the model utilizes a fractal-based volume-dividing algorithm to generate branching airway structures within the individual lobe boundaries. A second algorithm adds both arterial and venous segments to the generated airway tree and ensures that no intersection points exist between the various segments. Segment diameters have been assigned using rules developed from measurements from contrast-enhanced micro-CT images [WBC, paper 1], and are a function of both parent diameter and branching angle. Each of the three components, airway, arterial, and venous, contains approximately 30 000 segments. A major benefit of the model is that it contains many more segments than can be visualized and segmented within even contrast-enhanced CTs of the lung.

Several authors have assigned segment diameters using the length-diameter ratio. Although we did measure an average L/D ratio similar to these other authors, we found that a high degree of variability existed in this measurement. Instead we assigned a diameter based on a relationship between the diameter of the parent segment and the

branching angle theta (Equation 1). Basically, segments that branched off their parent segments at high angles were assigned a smaller percentage of their parent's diameter. This ignores the observation that airways can sometimes widen as they descend in several species of rodents.

Extensive validation revealed that the proposed model was unable to produce a close agreement with the anatomical measurements in all cases and that further development is required [See Chapter 4 – Mathematical Rodent Lung Model Validation]. Several other differences existed between the model and the actual structures as seen in Figure 7. Supernumerary vessels and shunts are absent, meaning that every airway segment has both a corresponding arterial and venous segment. The model also makes the assumption that every respiratory centre (ie. pulmonary acinus) is supplied by a single set of vascular segments (one arterial and one venous). The mathematical model contains segments from generation 0 (trachea) to generation 20 and are distributed in a way such that intermediate generation numbers are the most numerous. Although it contains less than 5% of the number of segments in the mathematical model, one of the anatomical datasets contained several airways of generation 22. This discrepancy is understandable based on the fact that each terminal segment, or respiratory centre, in the mathematical model could still branch several times to supply multiple alveoli.

A valid mathematical model can also be used to simulate various lung diseases. This can be done by generating lung models within previously acquired, un-enhanced CT images of control or baseline animals. Parameters can then be adjusted to simulate various pathologies. The relationships between airway and vascular diameters can be varied to reflect varying pulmonary blood pressures. Bronchoconstrictive diseases such as asthma can be simulated by occluding or narrowing different segments or groups of segments. The effect that changes in airway diameter can have on airway resistance, and hence one's ability to breathe, can then be calculated. These simulations may help to reduce the number of animals required for certain experiments. Further, such a model may have certain applications in particle deposition studies and may aid researchers in determining where various inhaled particles are deposited within the lung. Although the model was based partially on measurements from the rodent lung, it can easily be adjusted to allow application to other species of small animals that are used in pre-clinical imaging facilities.

References:

[1] **Berend N, Woolcock AJ, Marlin GE**. Relationship between bronchial and arterial diameters in normal human lungs. *Thorax, 1979, 34,354-358*

[2] **Burrowes KS, Hunter PJ, Tawhai MH**. Anatomically based finite element models of the human pulmonary arterial and venous trees including supernumerary vessels. *J Appl Physiol 99: 731-738, 2005*

[3] **Burrowes KS, Swan AJ, Warren NJ, Tawhai MH**. Towards a virtual lung: multi-scale, multi-physics modelling of the pulmonary system. *Phil. Trans. R. Soc. A 2008 366, 3247-3263*

[4] **Burton RT, Isaacs KK, Fleming JS, Martonen TB**. Computer Reconstruction of a Human Lung Boundary Model From Magnetic Resonance Images. *Respir Care 2004; 49(2): 180-185*

[5] **Garity JM, Segars WP, Knisley SB, Tsui BMW**. Development of a Dynamic Model for the Lung Lobes and Airway Tree in the NCAT Phantom. *IEEE Transactions on Nuclear Science, Vol.50, No.3, June 2003*

[6] **Horsfield K, Kemp W, Phillips S**. Diameters of Arteries, Veins, and Airways in Isolated Dog Lung. *Anatomical Record 216:392-395 (1986)*

[7] **Kitaoka H, Takaki R, Suki B**. A three-dimensional model of the human airway tree. *American Physiological Society 8750-7587/99*

[8] **Kitaoka H**. Computational morphology of the lung and its virtual imaging. *European Journal of Radiology 44 (2002) 164-171*

[9] **Lee D, Fanucchi MV, Plopper CG, Fung J, Wexler AS**. Pulmonary Architecture in the Conducting Regions of Six Rats. *The Anatomical Record 291:916-926 (2008)*

[10] **Lee D, Park SS, Ban-Weiss GA, Fanucchi MV, Plopper CG, Wexler AS**. Bifurcation Model for Characterization of Pulmonary Architecture. *The Anatomical Record 291:379-389 (2008)*

[11] **Martonen TB, Schrotoeter JD, Fleming JS**. 3D In Silico Modeling of the Human Respiratory System for Inhaled Drug Delivery and Imaging Analysis. *Journal of Pharmaceutical Sciences, Vol.96, No.3, March 2007*

[12] **Montesantos S, Fleming JS, Bolt LT**. A Spatial Model of the Human Airway Tree: The Hybrid Conceptual Model. *Journal of Aerosol Medicine and Drug Delivery Vol.23, No.1, 2010*

[13] **Phalen RF, Yeh HC, Schum GM, Raabe OG**. Application of an Idealized Model to Morphometry of the Mammalian Tracheobronchial Tree. *Anat. Rec. (1978) 190: 167-176*

[14] **Phillips CG, Kaye SR**. Diameter-based analysis of the branching geometry of four mammalian bronchial trees. *Respiration Physiology 102 (1995) 303-316*

[15] **Schmidt A, Zidowitz S, Kriete A, Denhard T, Krass S, Peitgen HO**. A digital reference model of the human bronchial tree. *Computerized Medical Imaging and Graphics 28 (2004) 203-211*

[16] **Schroeter JD, Fleming JS, Hwang D, Martonen TB**. A computer model of lung morphology to analyze SPECT images. *Computerized Medical Imaging and Graphics 26 (2002) 237-246*

[17] **Schroeter JD, Pritchard JN, Hwang D, Martonen TB**. Airway Identification Within Planer Gamma Camera Images Using Computer Models of Lung Morphology. *Pharmaceutical Research, Vol.22, No.10, October 2005*

[18] **Tawhai MH, Pullan AJ, Hunter PJ**. Generation of an Anatomically Based Three-Dimensional Model of the Conducting Airways. *Annals of Biomedical Engineering, Vol.28, pp.793-802, 2000*

[19] **Tawhai MH, Burrowes KS**. Developing Integrative Computational Models of Pulmonary Structure. The *Anatomical Record (Part B: New Anat.) 275B:207-218, 2003*

[20] **Tawhai MH, Hunter P, Tschirren J, Reinhardt J, McLennan G, Hoffman EA**. CT-based geometry analysis and finite element models of the human and ovine bronchial tree. *J Appl Physiol 97: 2310-2321, 2004*

[21] **Tebockhorst S, Lee DY, Wexler AS, Oldham MJ**. Interaction of epithelium with mesenchyme affects global features of lung architecture: a computer model of development. *J Appl Physiol 102: 294-305, 2007*

[22] **Ukil S, Reinhardt JM**. Anatomy-Guided Lung Lobe Segmentation in X-Ray CT Images. *IEEE Transactions on Medical Imaging, Vol.28, No.2, February 2009*

[23] **Yeh HC, Schum GM, Duggan MT**. Anatomical Models of the Tracheobronchial and Pulmonary Regions of the Rat. *Anat. Rec. (1979) 195: 483-492*

Tables

Table 1: Comparison of Anatomical and Model Data

	Airway		Arterial		Venous	
	Micro-CT	Model	Micro-CT	Model	Micro-CT	Model
θ (total)	53.39 ± 26.82	43.07 ± 34.80	49.35 ± 26.77	46.91 ± 35.98	48.46 ± 25.04	46.90 ± 36.05
θ_{major}	39.20 ± 24.48	40.08 ± 31.34	45.22 ± 25.95	40.93 ± 31.84	46.30 ± 21.89	41.05 ± 31.81
θ_{minor}	59.63 ± 25.39	44.81 ± 33.10	51.43 ± 26.96	50.43 ± 35.50	49.32 ± 26.14	50.28 ± 35.33
Φ	170.72 ± 105.66	181.37 ± 98.82	167.06 ± 104.13	176.62 ± 98.24	165.98 ± 102.24	176.62 ± 98.18
L/D	2.66 ± 1.90	2.98 ± 1.94	3.69 ± 2.99	4.39 ± 2.78	3.96 ± 3.60	2.56 ± 1.62
L/D_{major}	2.47 ± 1.88	2.81 ± 1.58	3.51 ± 3.03	3.56 ± 1.97	3.77 ± 3.42	2.59 ± 1.43
L/D_{minor}	2.76 ± 1.92	2.60 ± 1.39	3.78 ± 2.96	3.36 ± 1.70	4.04 ± 3.67	2.45 ± 1.24
D/D_{parent}	0.80 ± 0.22	0.80 ± 0.05	0.68 ± 0.26	0.80 ± 0.05	0.68 ± 0.27	0.80 ± 0.05
$\%D/D_{parent}<1$	87.80	99.99	88.80	99.99	90.99	99.99
D_{major}/D_{parent}	0.93 ± 0.22	0.82 ± 0.04	0.72 ± 0.26	0.81 ± 0.04	0.72 ± 0.28	0.82 ± 0.04
D_{minor}/D_{parent}	0.75 ± 0.21	0.79 ± 0.05	0.66 ± 0.26	0.79 ± 0.05	0.67 ± 0.27	0.79 ± 0.05
L/L_{parent}	1.02 ± 1.02	0.96 ± 0.65	1.59 ± 1.89	0.92 ± 0.56	1.57 ± 1.99	0.92 ± 0.55
$\%L/L_{parent}<1$	65.92	65.33	50.92	67.92	53.66	67.90

Data expressed as mean ± SD

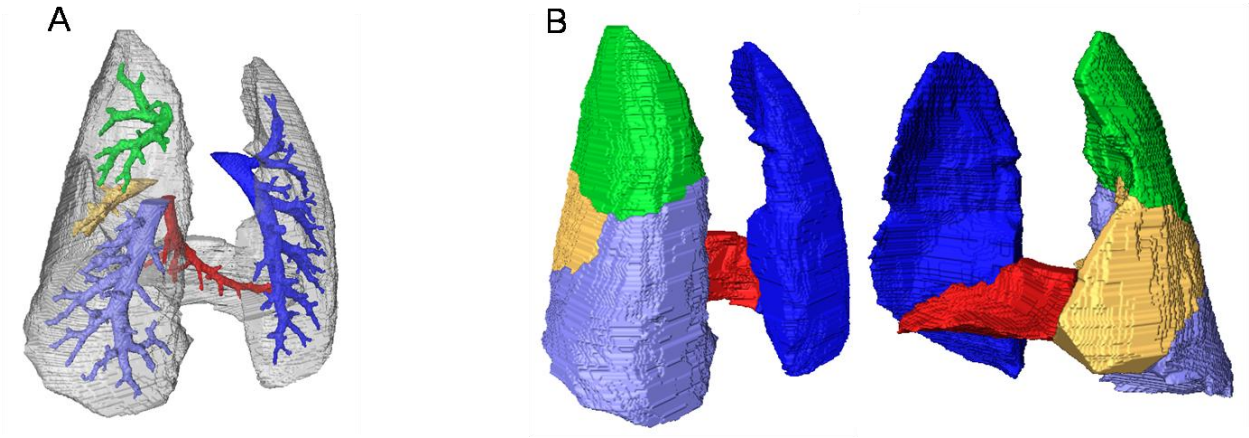

FIGURE 1: Lobar separation of the lung into left (blue), cranial (green), middle (yellow), caudal (purple), and accessory (red) lobes. A) Starting point from contrast-enhanced CT includes Lung field and segmented airways. B) Lung field divided into individual lobes.

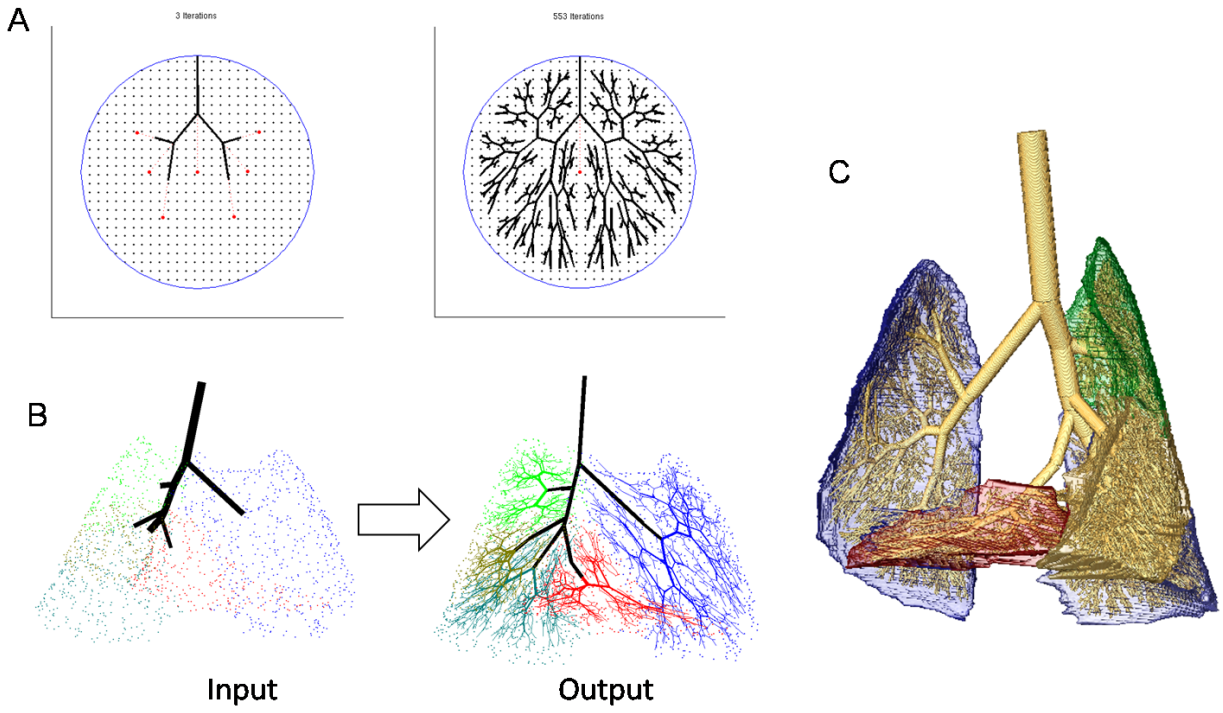

FIGURE 2: Airway generating algorithm using volume division. A) Two dimensional example of airway algorithm after 3 and 533 iterations. B) Input, including lobe boundaries and entry points, and output of airway algorithm in three dimensions. C) Representative Airway Tree generated using this method.

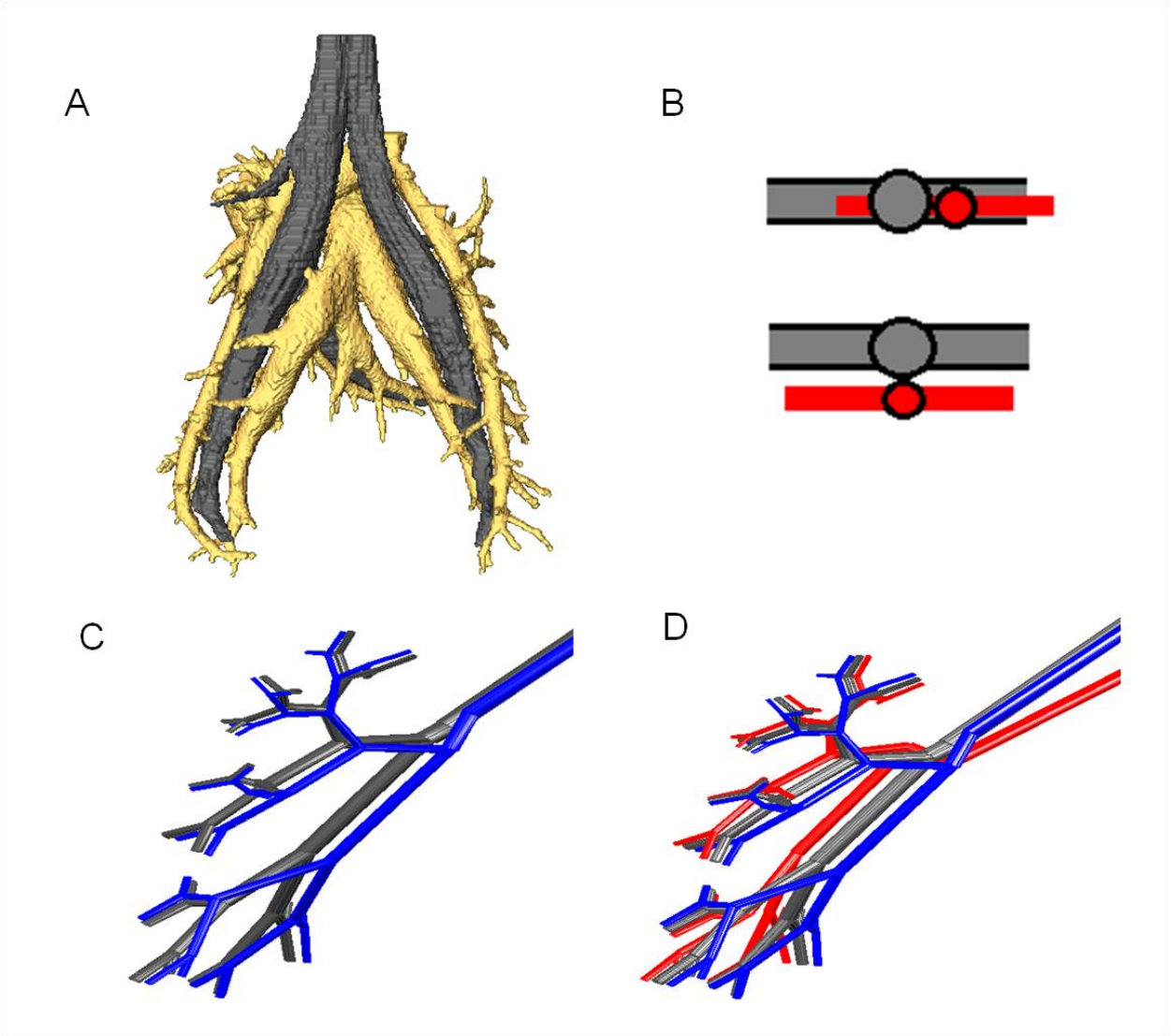

FIGURE 3: Vascular tracing algorithm. A) Segmentation of major airways and pulmonary vasculature showing spatial relationship between them. B) Bifurcation viewed from above; problematic orientation causing intersection (top) and preferred orientation which avoids intersection (bottom). C) Airway segments with added vascular tree, D) Airway segments with added arterial and venous vasculature.

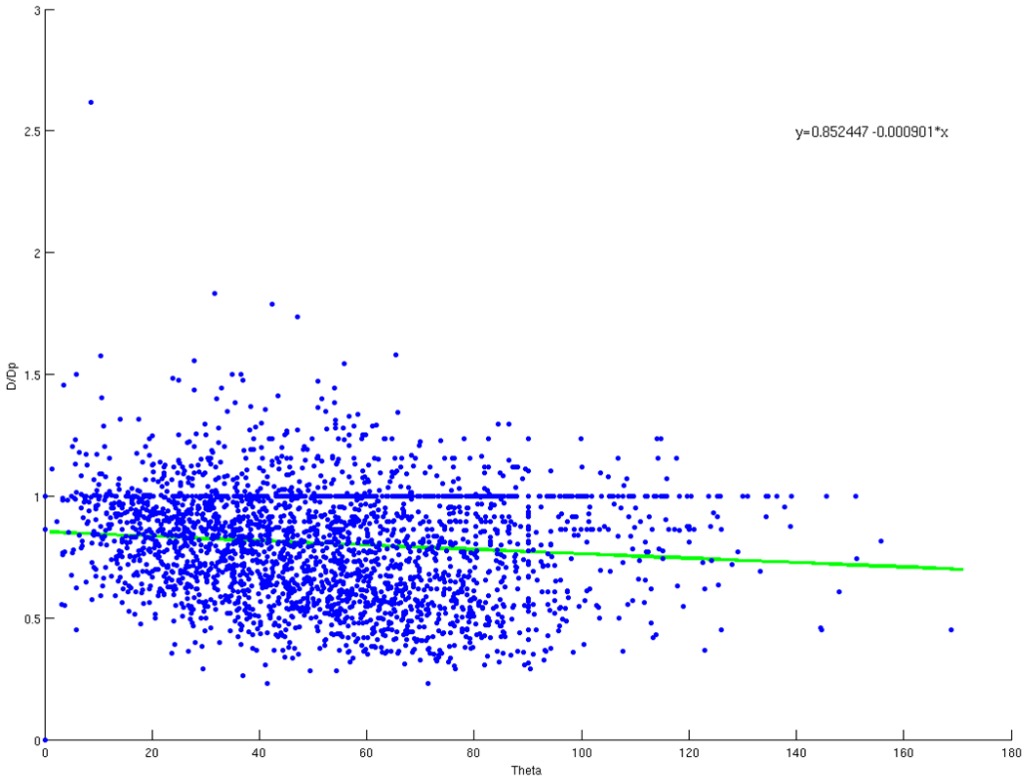

FIGURE 4: Relationship between D/D_P and Theta from contrast-enhanced airways

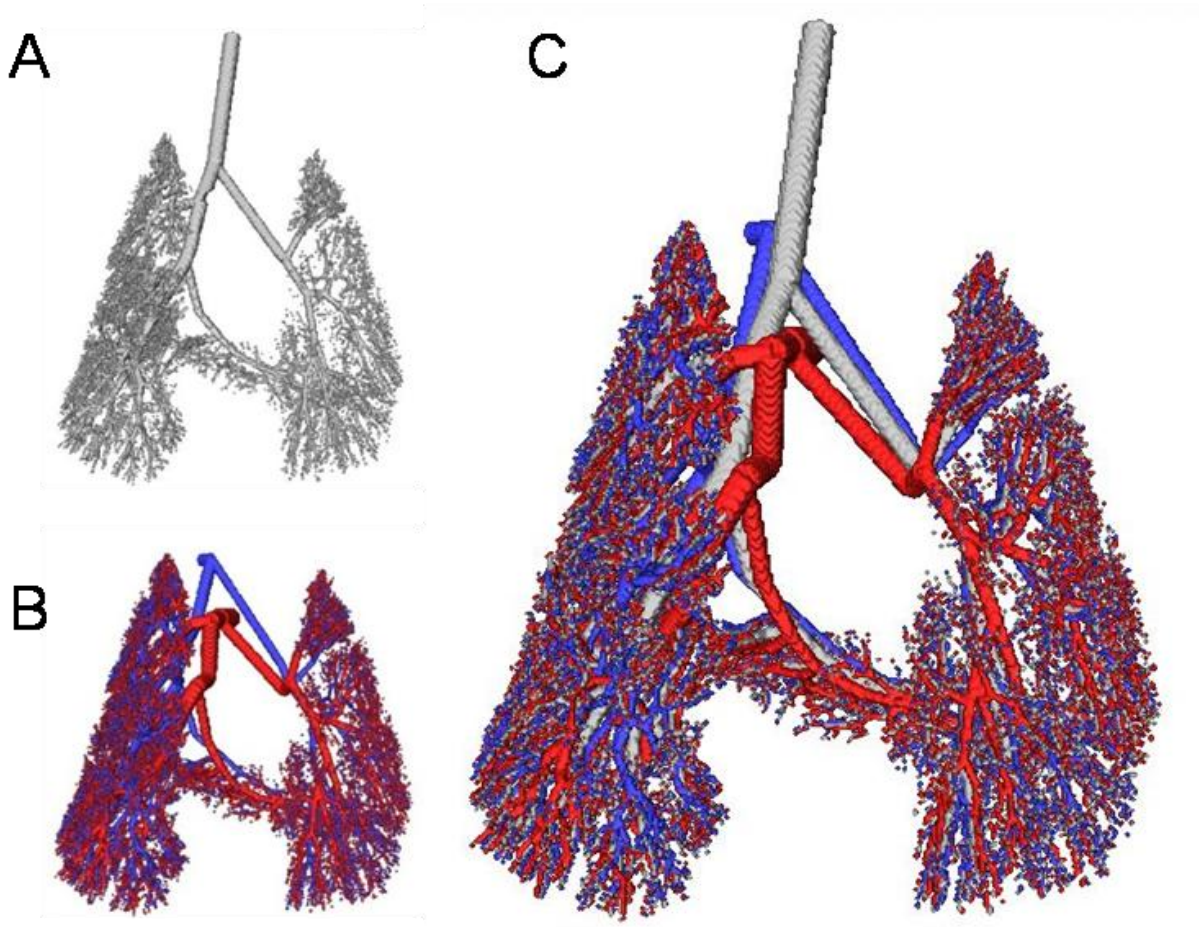

FIGURE 5: Virtual Lung Model. A) Airway model, B) vascular model, and C) model with airway and vasculature combined.

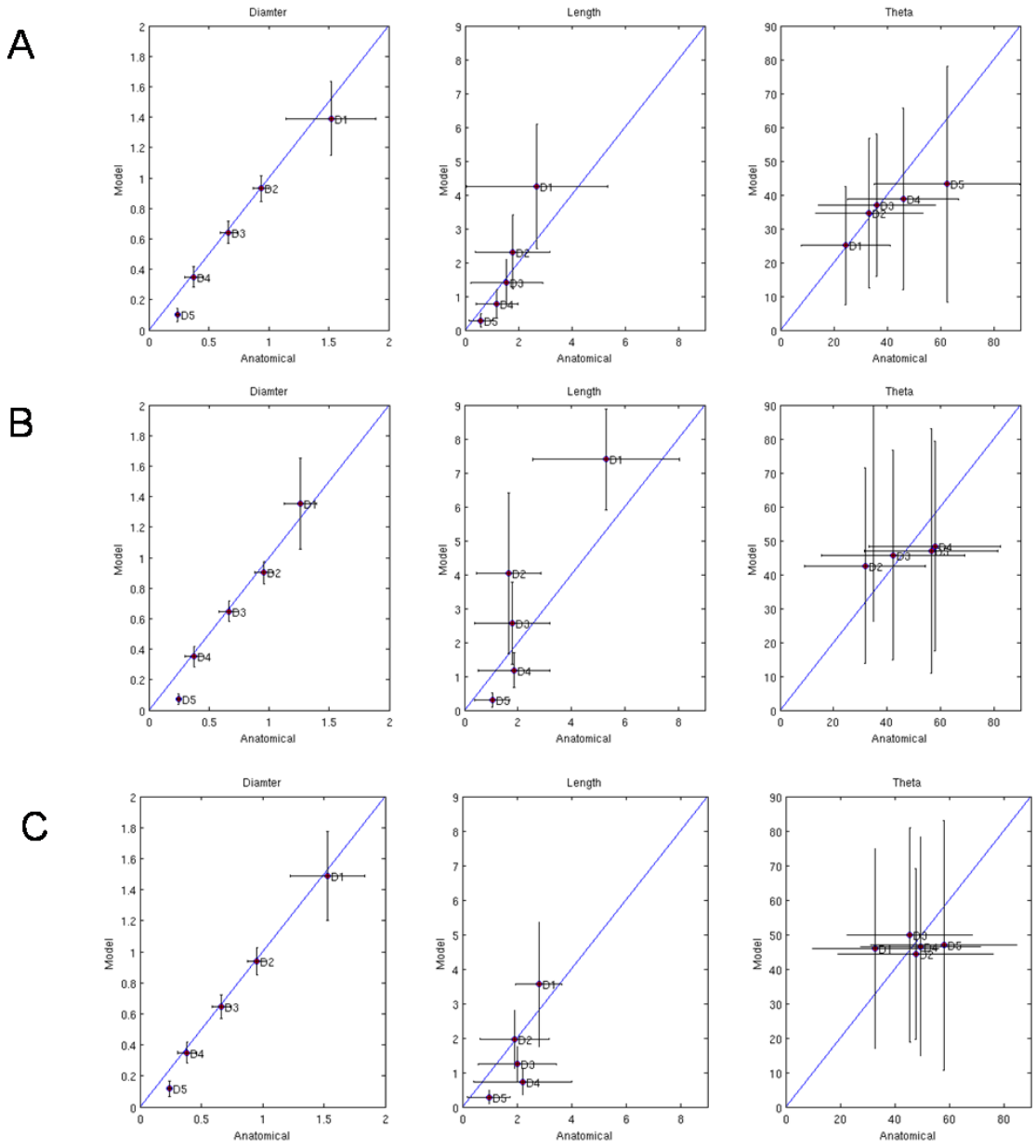

FIGURE 6: Comparison of Model Data and Anatomical Measurements for Airway (A), Arterial (B), and Venous (C) diameters, lengths, and branching angles. D1 contains segments with diameters ≥ 1mm, D2 contains segments ranging from 0.75 to 1mm, D3 contains segments ranging from 0.5 to 0.75mm, D4 contains segments ranging from 0.25 to 0.5mm, and D5 contains segments less than 0.25mm in diameter.

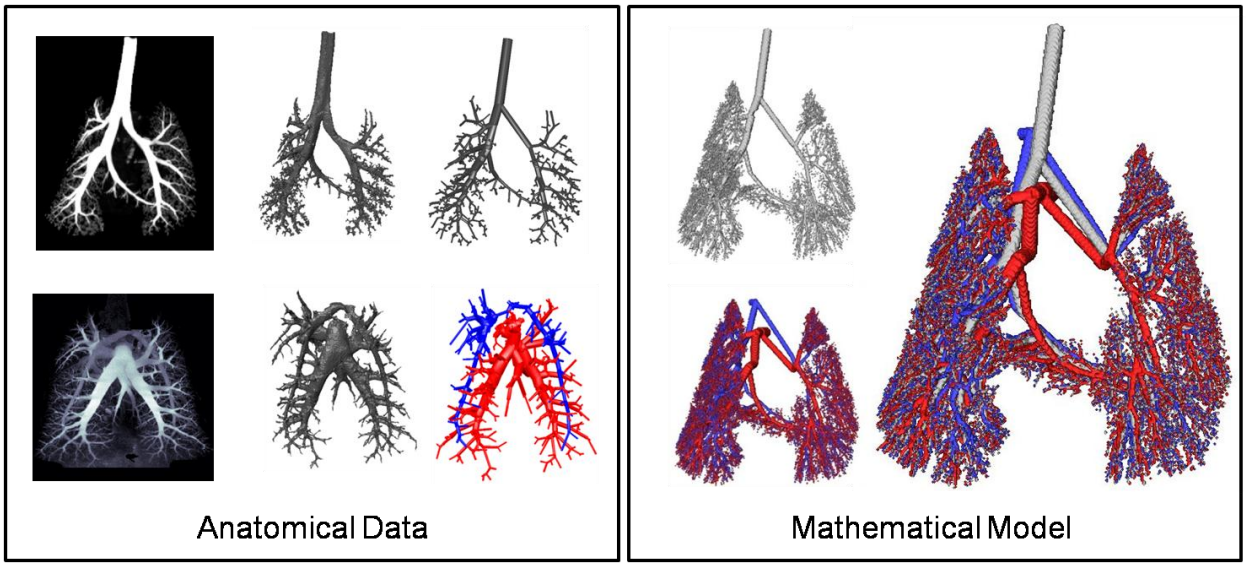

FIGURE 7: Summary of modelling process; Anatomical data (left box) and Mathematical model (right box).

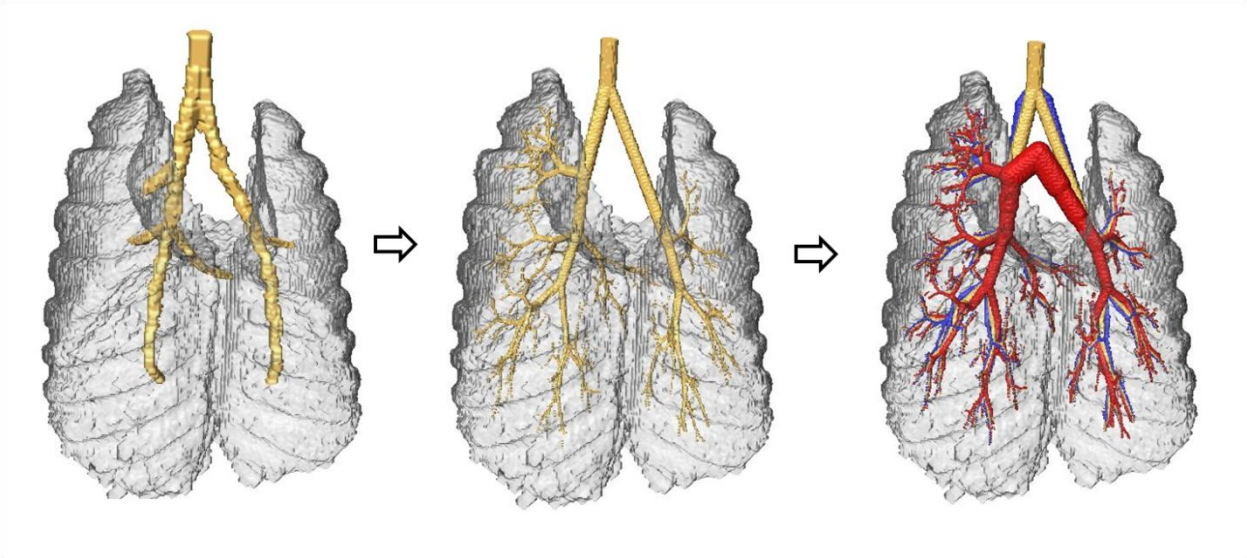

FIGURE 8: Summarizing the application of the model to an un-enhanced CT (from left to right); starting point (airway and lung segmentations), extension of airways using branching algorithm, addition of arterial and venous segments using vascular tracing algorithm.

4 Mathematical Rodent Lung Model Validation

Introduction:

In this chapter, further validation of the mathematical lung model described in chapter 3 was undertaken.

Method:

Airway models were generated for animals which had contrast-enhanced measurements. These models were generated using the exact protocol for applying the model to unenhanced animals. As a starting point, each model used a segmentation of the main airways and generated an airway tree using a space-filling approach. The branching fraction was set at 0.4 [*Tawhai-Anatomical Record 275B:207-218,2003*] and segment diameter was determined from the measured relationship between the parent airway diameter and the branching angle theta ($D/D_P = 0.852*\theta - 0.001$); the values were allowed to vary slightly to create an element of randomness within the generated models. When a segment diameter decreased to below 0.02 mm it was no longer allowed to branch, and hence became a terminal segment. After generating each model, it was run through the segmentation/measurement software. The parameters measured from the airway model were then compared to the anatomical measurements for that animal. Comparison data for the mouse is shown by both diameter categories and generation numbers (Figure 4.1-4.6). Diameter categories for the mouse were set at $D1 \geq 0.8$ mm, $0.8\text{mm} > D2 \geq 0.6$ mm, $0.6\text{ mm} > D3 \geq 0.4$ mm, $0.4\text{ mm} > D4 \geq 0.2$ mm, $D5 < 0.2$mm. The number of segments for each diameter category and generation number are shown in tables 4.1 and 4.2.

Figure 4.1: Generated Mouse Airway Models

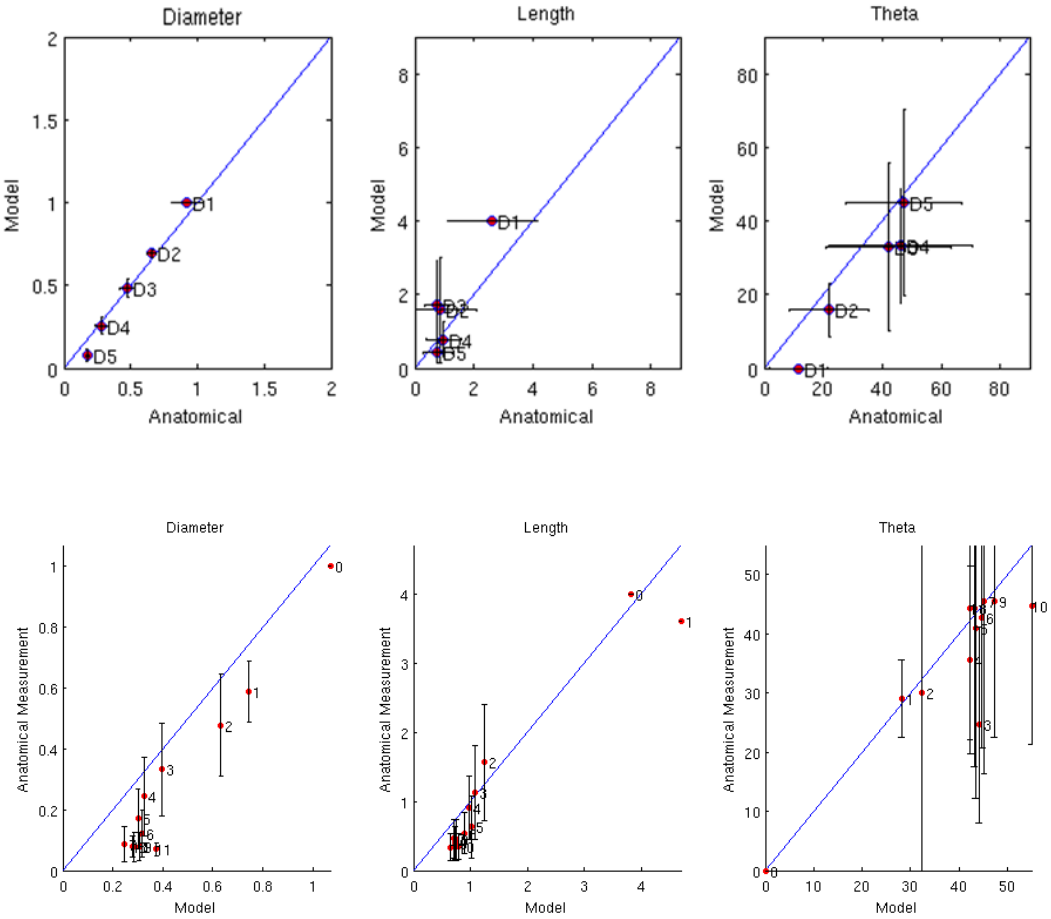

Figure 4.2: Comparison between anatomical and model data for mouse1 by diameter (top) and generation (bottom).

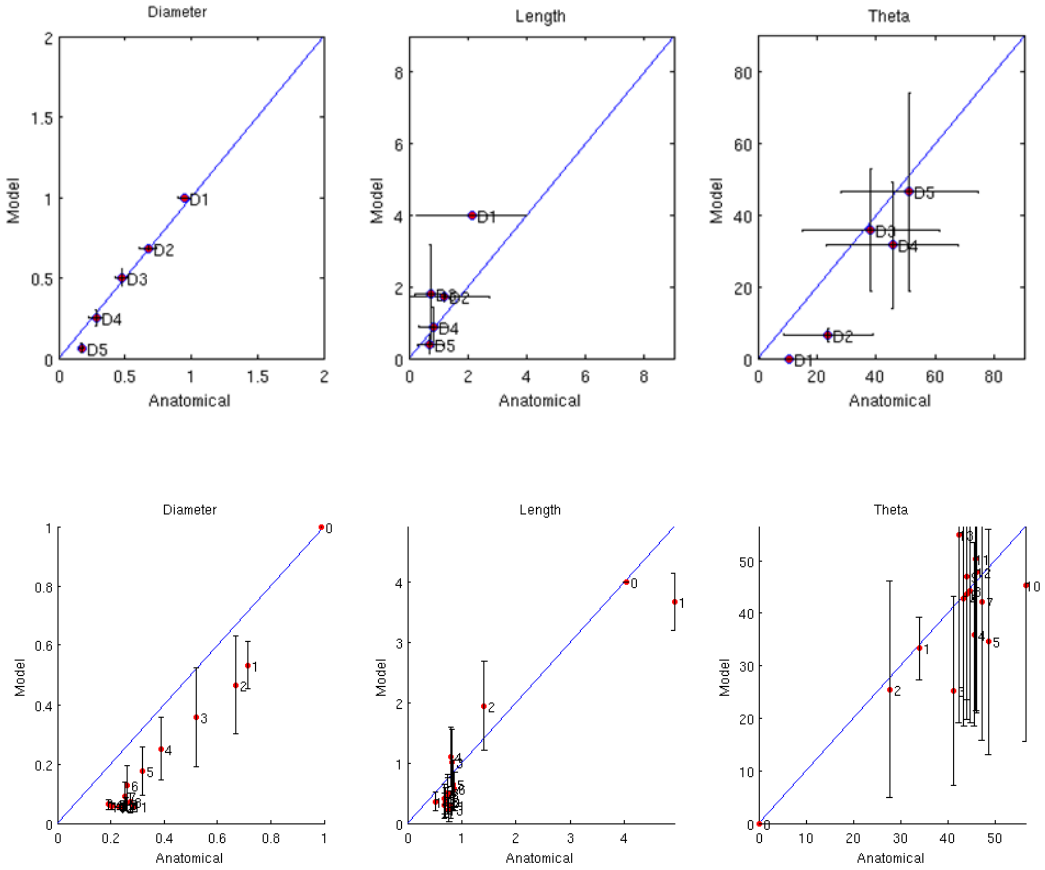

Figure 4.3: Comparison between anatomical and model data for mouse2 by diameter (top) and generation (bottom).

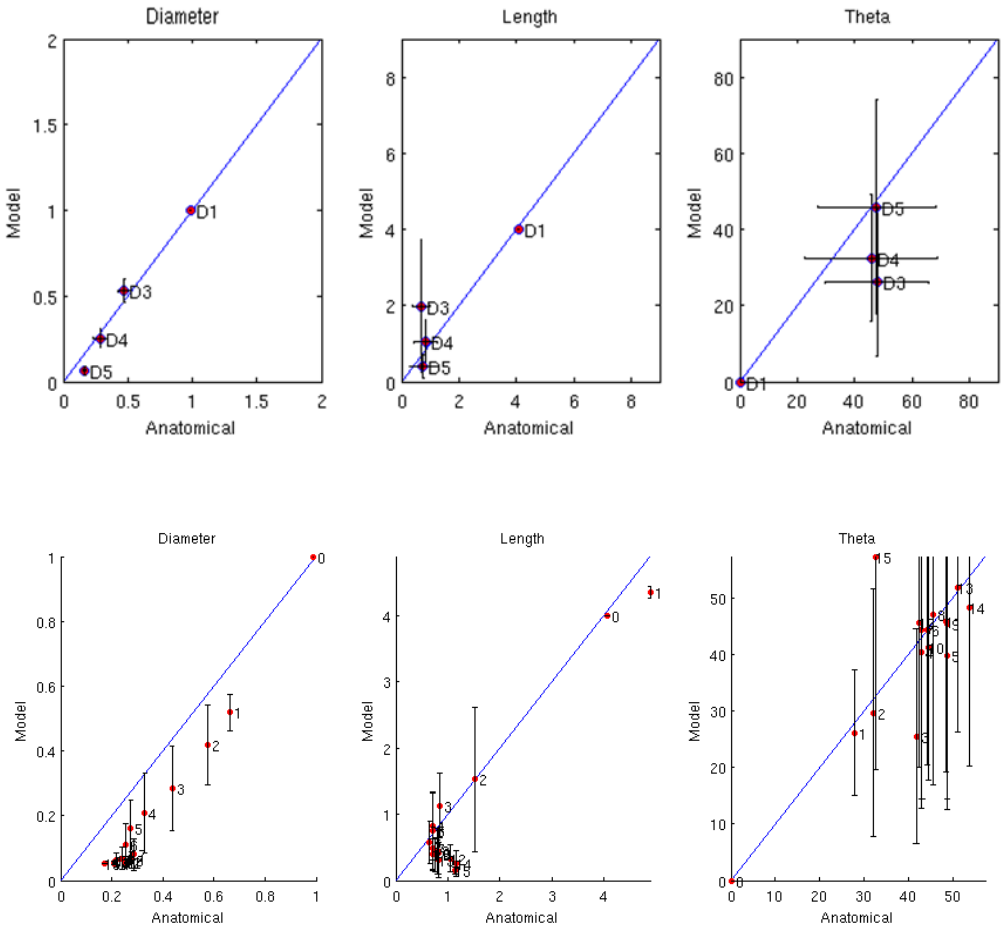

Figure 4.4: Comparison between anatomical and model data for mouse3 by diameter (top) and generation (bottom).

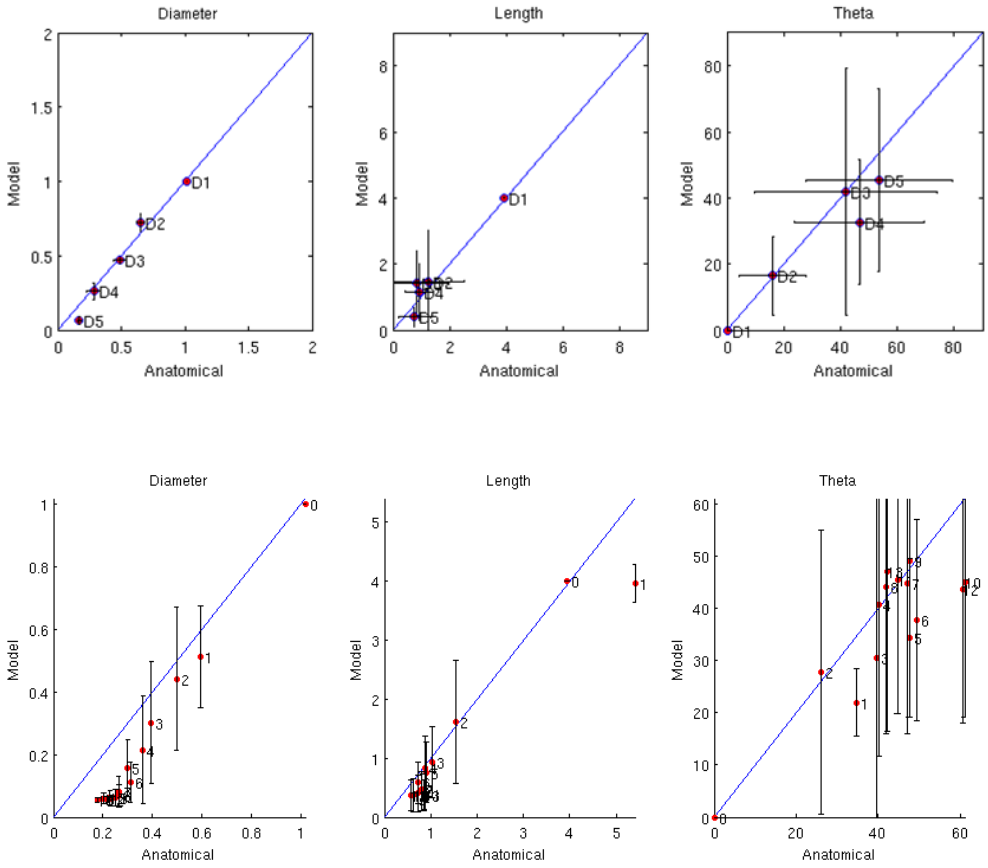

Figure 4.5: Comparison between anatomical and model data for mouse4 by diameter (top) and generation (bottom).

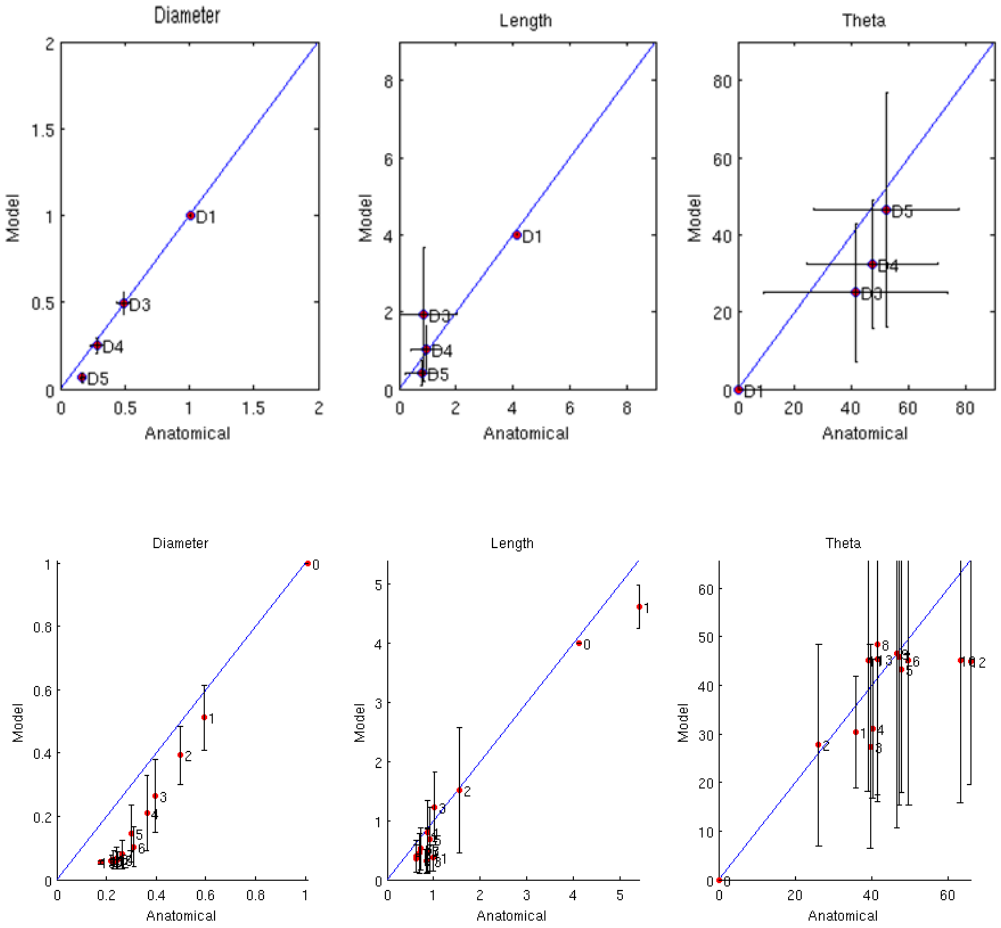

Figure 4.6: Comparison between anatomical and model data for mouse5 by diameter (top) and generation (bottom).

Table 4.1: Number of Segments for Different Diameter Categories for the Mouse

Diameter Category	Mouse 1		Mouse 2		Mouse 3		Mouse 4		Mouse 5	
	Anatomical	Model	Anatomical	Model	Anatomical	Model	Anatomical	Model	Anatomical	Model
D1	4	1	3	1	1	1	1	1	1	1
D2	17	4	16	2	16	0	11	4	10	0
D3	24	5	29	7	15	7	27	2	27	8
D4	69	49	92	46	65	36	59	28	57	32
D5	88	1545	146	1486	86	1231	86	1084	81	1198

Table 4.2: Number of Segments for Different Generation Numbers for the Mouse

Gen.	Mouse 1		Mouse 2		Mouse 3		Mouse 4		Mouse 5	
	Anatomical	Model	Anatomical	Model	Anatomical	Model	Anatomical	Model	Anatomical	Model
0	1	1	1	1	1	1	1	1	1	1
1	2	2	2	2	2	2	2	2	2	2
2	4	4	4	4	4	4	4	4	4	4
3	10	8	8	8	9	8	9	8	9	8
4	16	16	14	16	16	16	14	14	14	16
5	21	35	23	32	22	29	22	24	22	32
6	20	66	34	62	24	58	24	48	24	65
7	31	135	30	126	19	117	26	96	27	115
8	18	225	24	227	23	187	18	150	20	184
9	15	237	27	291	14	207	20	186	20	194
10	15	192	24	312	19	162	18	157	13	142
11	8	177	15	259	10	163	12	124	8	135
12	10	231	23	161	9	165	10	137	8	133
13	10	211	19	37	7	116	4	99	4	119
14	8	57	9	4	2	37	0	57	0	76
15	7	7	6	0	2	3	0	12	0	13

The process was then repeated for the rats that received contrast enhancement. The parameters used were the same as those used for the mouse. Comparison data for the rat is shown by both diameter categories and generation numbers (Figures 4.7 -4.12). Diameter categories for the rat we set to D1 ≥ 1 mm, 1mm > D2 ≥ 0.75 mm, 0.75 mm > D3 ≥ 0.5 mm, 0.5 mm > D4 ≥ 0.25 mm, D5 < 0.25mm. The number of segments for each diameter category and generation number are shown in tables 4.3 and 4.4.

Figure 4.7: Generated Rat Airway Models

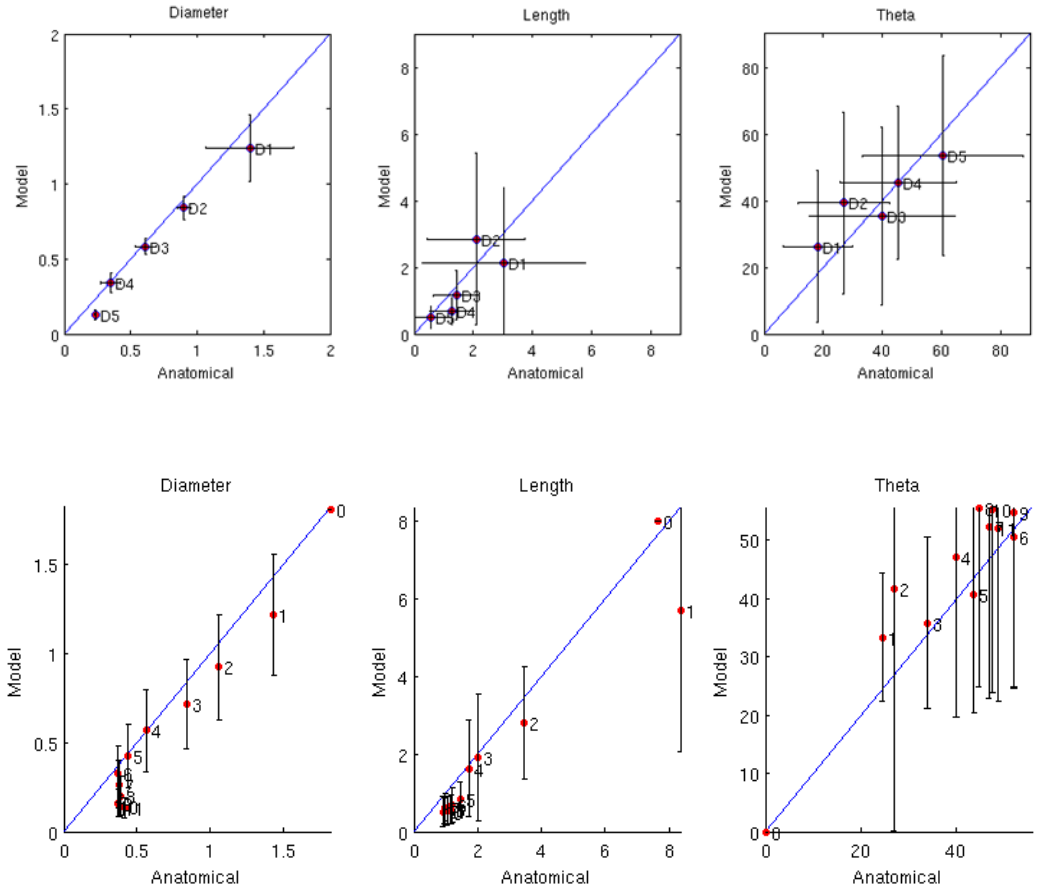

Figure 4.8: Comparison between anatomical and model data for Rat 1 by diameter (top) and generation (bottom).

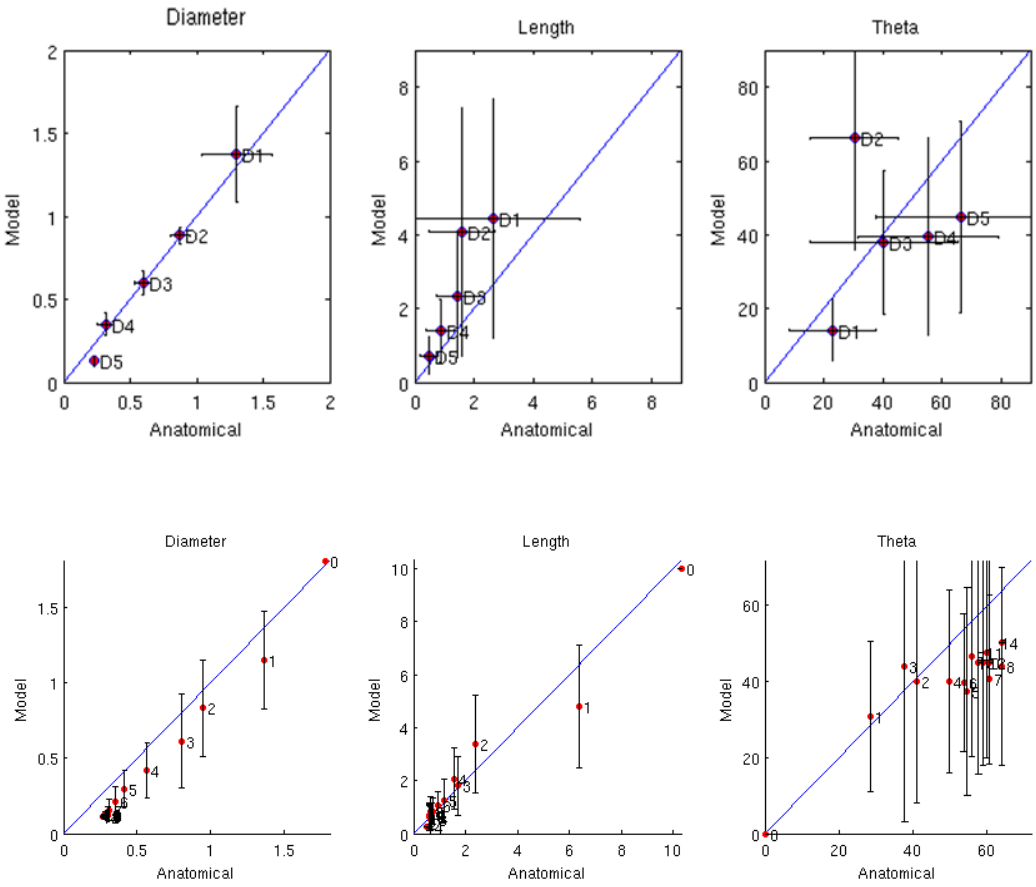

Figure 4.9: Comparison between anatomical and model data for Rat 2 by diameter (top) and generation (bottom).

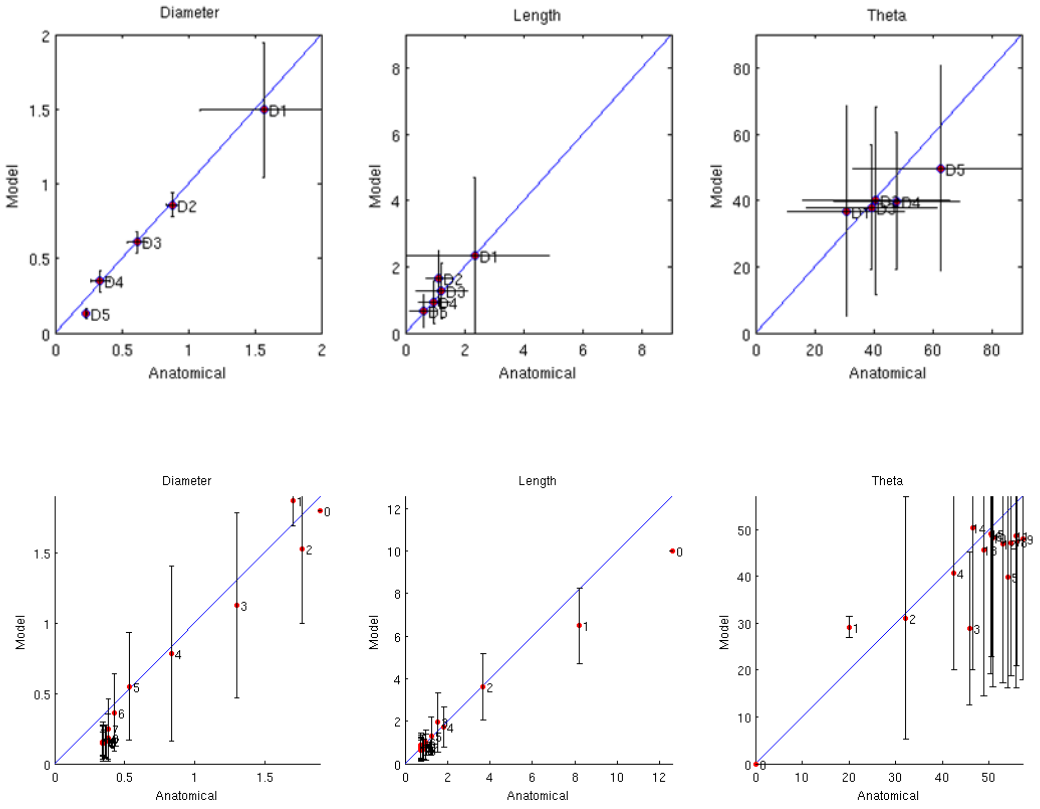

Figure 4.10: Comparison between anatomical and model data for Rat 3 by diameter (top) and generation (bottom).

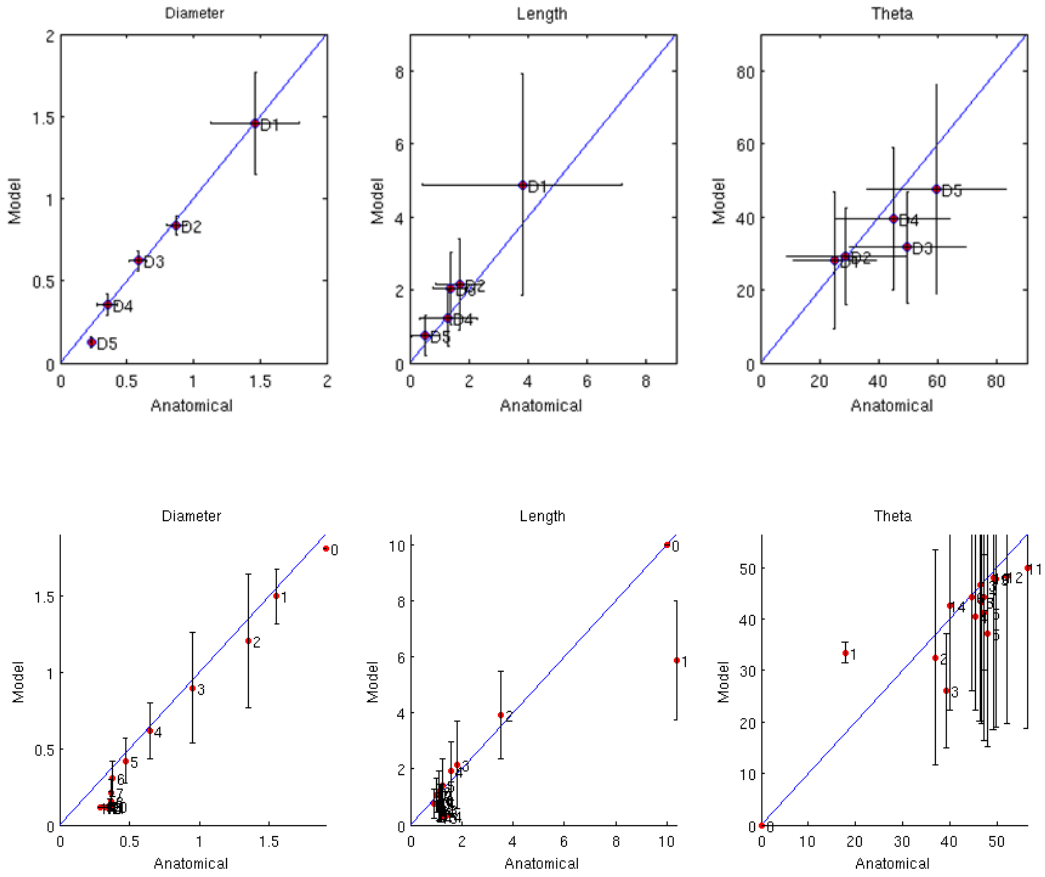

Figure 4.11: Comparison between anatomical and model data for Rat 4 by diameter (top) and generation (bottom).

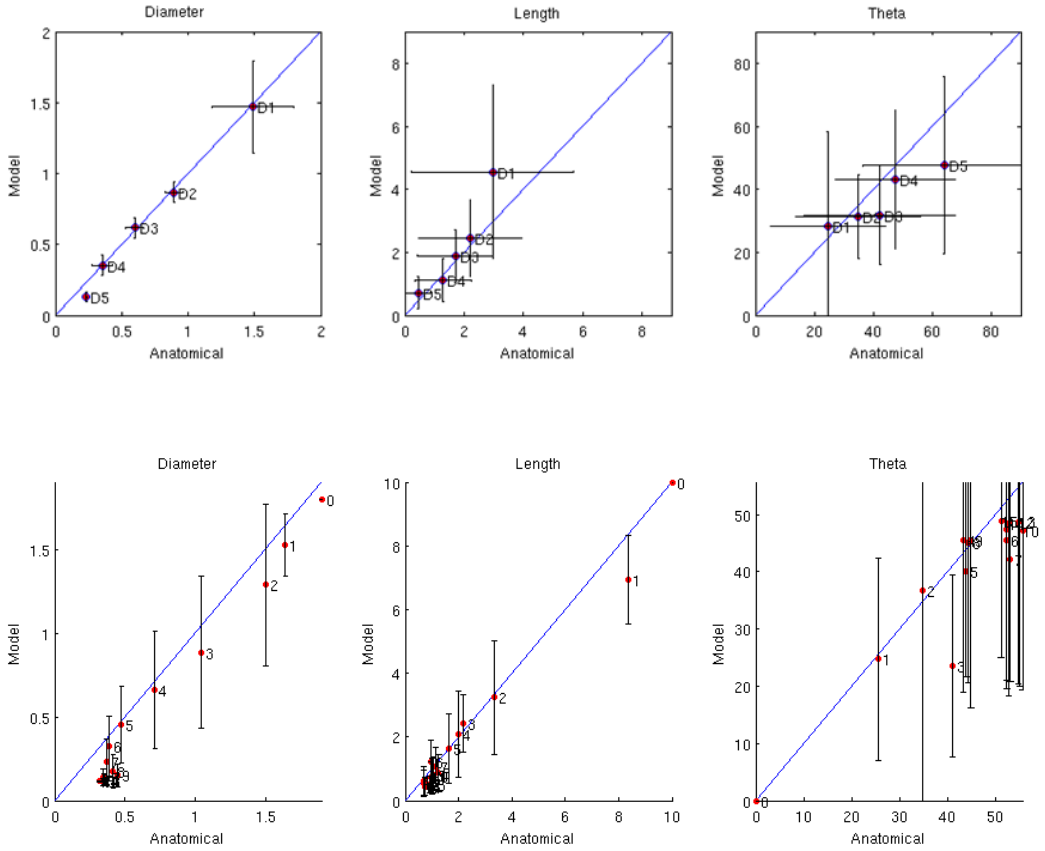

Figure 4.12: Comparison between anatomical and model data for Rat 5 by diameter (top) and generation (bottom).

Table 4.3: Number of Segments for Different Diameter Categories for the Rat

Diameter	Rat 1		Rat 2		Rat 3		Rat 4		Rat 5	
Category	Anatomical	Model	Anatomical	Model	Anatomical	Model	Anatomical	Model	Anatomical	Model
D1	27	187	16	5	44	31	18	8	23	11
D2	18	16	20	2	23	24	15	9	11	10
D3	70	94	31	11	66	51	20	18	28	27
D4	220	797	349	59	398	269	186	114	142	161
D5	0	5975	586	950	336	3184	85	1725	79	2410

Table 4.4: Number of Segments for Different Generation Numbers for the Rat

Gen.	Rat 1		Rat 2		Rat 3		Rat 4		Rat 5	
	Anatomical	Model	Anatomical	Model	Anatomical	Model	Anatomical	Model	Anatomical	Model
0	1	1	1	1	1	1	1	1	1	1
1	2	2	2	2	2	2	2	2	2	2
2	4	3	4	4	4	4	4	4	4	4
3	8	8	8	9	9	8	8	8	9	8
4	16	16	18	16	20	17	16	17	18	17
5	33	32	37	32	44	32	33	32	33	30
6	50	62	58	60	68	61	53	61	41	62
7	48	119	77	116	72	122	50	123	35	121
8	40	244	85	190	70	217	36	236	22	229
9	27	437	70	218	72	330	28	380	18	349
10	21	627	84	163	73	375	23	426	24	418
11	16	791	81	127	69	382	18	328	20	451
12	16	887	84	64	54	265	17	168	15	466
13	18	794	85	24	55	238	10	73	13	326
14	10	595	79	1	55	285	8	11	11	115
15	8	326	53	0	51	309	5	4	9	16

Discussion and Conclusions:

This chapter details an extended validation for the rodent lung model. Although the vascular components of the model had initially been compared to the anatomical measurements, fundamental differences between the modeled and anatomical vasculature do not permit an informative direct comparison between the two. This discrepancy is a limitation of the model but I do believe that an agreement between the airway and vascular components of the model take priority over an exact agreement with the anatomical measurements.

As mentioned previously, each model used a segmentation of the main airways and generated an airway tree using a space-filling approach. The branching fraction was set at 0.4 [*Tawhai-Anatomical Record 275B:207-218,2003*] and segment diameter was determined from the measured relationship between the parent airway diameter and the branching angle theta ($D/D_P = 0.852*\theta - 0.001$); the values were allowed to vary slightly to create an element of randomness within the generated models. When a segment diameter decreased to below 0.02 mm it was no longer allowed to branch, and hence became a terminal segment. These parameters were used for both the rat and the mouse.

In this validation, the proposed lung model was used to generate airway trees within the lung boundaries of animals which had received contrast-enhancement for the purpose of CT-based measurements. The modeled parameters were compared to the measured parameters as both a function of generation number and categorized diameter. The number of segments within each generation and each diameter category were also compared. From these comparisons, it was determined that the proposed model failed to be fully representative of either the rat or the mouse lung.

A comparison of the modeled and measured parameters for the mouse (Figures 4.2-4.6) and for the rat (Figures 4.8-4.12) revealed several discrepancies. The model was unable to produce a close agreement with the anatomical measurements in all cases. Additionally, for the mouse, the model overestimated segment diameter as a function of generation number.

The largest discrepancy between the anatomical and modeled airways was found to be in the distribution of segment diameters. Tables 4.1 and 4.3 compare the number of segments within each of the five diameter categories. Discrepancies in the number of segments within the larger diameter categories (D1-D2) were not expected and are likely due to a failure of the proposed model. For the smaller diameter categories (D3-D5), however, the number of segments was much greater for the modeled airways than for the measured airways; this was expected because the aim of the model was to extend the airways beyond what could be resolved with the CT.

The reasons that the proposed model was unable to be fully representative of the rodent lung are difficult to delineate completely. It is entirely possible that a space-

filling algorithm, used in the proposed model to generate an airway tree within an anatomically-derived lung boundary, is less appropriate for the rodent airways than it is for the human airway tree [*Tawhai-Anatomical Record 275B:207-218,2003, Martonen-J Pharmological Sciences, Vol.96,No.3,March 2007*]; this is likely due to the much greater asymmetry in the rodent lung. A space-filling algorithm was used to insure that the generated airway model fit reasonably into the regions of the CT image that corresponded to the lungs. It is also possible that the optimal combination of parameter values (branching factor, diameter assignment, termination criteria) utilized in the space-filling algorithm have not been obtained. It was observed that the termination criteria used in this case did allow for some segments to be less than the anatomical limit (0.02 mm for both rats and mice), although this would only affect the smallest diameter category and the highest generation numbers. Another possibility is that not every method used to examine the validity of the model was entirely appropriate; perhaps a comparison of segments by 5 diameter categories was not the optimal method of assessment.

The pursuit of a more accurate lung model could progress in one of two major directions. The first would be to continue with a space-filling approach and to further adjust combinations of parameters (branching fraction, diameter assignment, etc.) until a better correlation is achieved. The other possibility is to shift into an entirely new direction and move away from a space-filling model. One possibility could be to apply a non-rigid transformation to fit a contrast-enhanced lung onto an unenhanced lung and then to apply that same transformation to the contrast-enhanced lung structure (airways or vasculature). The constantly changing size and shape of the lung, however, would likely make this process difficult and time-intensive, if possible at all.

Instead of creating and applying a lung model, another possibility would be to focus on the ability to extract more of the airway structure from individual unenhanced CTs. Although this method may not be suitable for various simulation studies, it may provide a better tool for image analysis. It would therefore be possible to identify actual airways within the image instead of predicting airway location. This process is, however, heavily dependent on the CT resolution. Software has been developed [Vida Diagnostics] to do this with clinical CTs, but it is uncertain whether the software will improve airway segmentation results from the current pre-clinical CT system. Additionally, the software may prove to be ineffective in certain cases of severe lung disease.

In any case, serious consideration needs to be given to the models final purpose. Different types of lung models may be more or less applicable to various applications and a specific purpose should be kept in mind when designing and optimizing a model. While this model is currently unable to fully predict airway and vascular structure, it has provided valuable insight into the steps necessary to accomplish a similar task in the future.

5 An Automated Method for Quantifying Airspace Enlargement in Whole Histological Lung Slices

5.1 Synopsis

Chapters 2 and 3 focus on the largest anatomical features of the lung, namely, the airways and conducting vasculature. These regions are involved in the transport of air and blood to and away from the respiratory zones. This section, as opposed to being focused on the conducting region of the lung, focuses on the respiratory region of the lung, containing alveoli and the surrounding capillary beds. As mentioned, certain diseases of the lung affect this respiratory zone and hence decrease the lungs capability for gas exchange. Lung histology is often performed to study the micro-architecture of the lung. More precisely, it is done to observe changes in alveolar structure and size. This work introduces an automated technique for quantifying airspace enlargement in histological lung sections that is often present in emphysema. A provisional patent has been filed and the software (Pneumometrics) will soon be available commercially.

5.2 Contribution to Manuscript

As primary author, I, WB Counter, conceived and developed the method for quantifying airspace enlargement. I wrote the software and did all the debugging. I analyzed data and wrote the manuscript. BN Jobse contributed to study design, analyzed data, and edited the manuscript; RG Rhem contributed to study design, provide expertise in Matlab and edited the manuscript; NR Labiris contributed to study design, provided expertise in lung anatomy/physiology, and edited the manuscript.

5.3 Manuscript

This manuscript has been submitted to the American Thoracic Society journal, Respiratory Cell and Molecular Biology. References are listed in the order that they appear within the manuscript.

An Automated Method for Airspace Quantification in Whole Histological Lung Slices

William B. Counter, Brian N. Jobse, Rod G. Rhem, N. Renee Labiris

Department of Medicine, Firestone Institute for Respiratory Health – St. Joseph's Healthcare,
McMaster University, Hamilton, Ontario, Canada

Author Contributions:
WBC contributed to concept, wrote the software, analyzed data, and wrote the manuscript; BNJ contributed to concept, analyzed data, assisted in writing the software, and edited the manuscript; RGR contributed to concept, assisted in writing the software and edited the manuscript; NRL contributed to concept, provided expertise in lung structure/physiology, aided in data analysis, provided financial support, and edited the manuscript.

Financial Support: N.R. Labiris holds an Internal Department of Medicine Career Award

Running Head: Automated Lung Histology

Word Count: 2727

Correspondence: Name: Dr. Renée Labiris
Mailing Address: 1280 Main St. W., Hamilton, Ontario, L8S 4K1, Health Science Centre, rm. 1V11
Phone: 905 521-2100 ext. 75657
Fax: 905 546-1125
Email Address: labir@mcmaster.ca

Abstract:

Respiratory disorders, such as emphysema and bronchopulmonary dysplasia, are accompanied by airspace enlargement within the lung, decreasing the efficiency of gas exchange. Traditionally, airspace size is determined through manual measurements of high magnification images of histological slices of lung tissue; this process is both time and labour intensive and usually limited to small regions of interest. We have developed an automated method of measuring airspace parameters, including number and size, which can be applied to whole histological lung slices. The automated technique was validated by comparing its results to the gold standard method, mean linear intercept length (L_m) measurements in a rodent model of lung development; our measurements were highly correlated with the L_m measurements. The method was then applied to two mouse models of COPD, chronic cigarette smoke (CS) exposure and porcine pancreatic elastase (PPE) exposure. Both PPE-exposed and CS-exposed animals had significantly fewer airspaces per unit area, with airspaces being significantly larger in size than control mice. We also analyzed randomly-selected regions of interest to determine whether our whole-slice technique was more sensitive; airspace enlargement in the CS-model was only detectable using a whole slice analysis. This quantification of whole histological lung slices is highly correlated to L_m measurements and more sensitive to small changes in airspace size compared to region-of-interest analyses. The automation of this technique will significantly reduce analysis time, largely eliminate sampling bias, and reduce the number of animals required for a study.

Abstract Word Count: 238

Key Words: Quantitative histology, airspace size, automated measurements, mean linear intercept, emphysema

Introduction:

To understand the impact of lung disease, and its development, on the structure/function relationships within the lung it is first necessary to understand lung structure. Certain respiratory disorders, such as emphysema and bronchopulmonary dysplasia, involve the enlargement of airspaces within the lung. The functional consequence of airspace enlargement is a decrease in the efficiency of gas exchange. In animal models of lung disease [1], as well as in clinical practice [2], increases in airspace size are often measured from two-dimensional lung histology, a process where the lung is fixed and sectioned into very thin slices and studied at high magnification under a microscope.

The current gold standard for quantitative assessment of lung histology, specifically alveolar dimensions, is mean linear intercept length (L_m) [3]. This method involves laying a set of grid lines onto a small region of interest (ROI), and cleaving the grid lines where they intersect the alveolar septa from the histology image [4]. The resultant outcome is usually calculated by either averaging the lengths of the broken grid lines or dividing the total length of the grid lines by the number of intersections. One of the main disadvantages of this method is that analysis is limited to only a small fraction of the available histological data and therefore may not be representative of the whole lung. L_m measurements can be tedious and time consuming and are not always performed the same way at different centres making the comparison of morphometric studies difficult.

We have developed and validated software for the characterization of airspaces in whole histological lung sections. Our method was applied to two animal models of emphysema. Additionally, we compared our whole slice analysis to one using randomly-sampled regions of interest. The advantages of automating histological measurements are that many more airspaces can be efficiently and objectively measured and the analysis time is greatly reduced. The ability to quantify a large number of airspaces allows complete histological slices to be analyzed, largely eliminating any sampling bias which could lead to diseased areas being missed or overestimated, particularly in cases of heterogeneous lung disease.

Methods:

Animals: All animal experiments were approved by the Animal Research Ethics Board at McMaster University, in accordance with the Canadian Council on Animal Care guidelines. Animal details are discussed below.

Tissue Preparation and Histology: Following animal sacrifice and lung removal, the left lung lobe was cannulated and fixed at 30cm H_20 pressure with 10% formalin and submersed for 24 hours. It was then sectioned into 4 slices taken at evenly spaced increments between apex and base, and embedded in paraffin according to ATS guidelines [3]; 3-µm thick sections, sliced with a Leica 2255 microtome (*Leica Microsystems GmbH, Wetzlar, Germany*), were stained with haematoxylin and eosin (H&E). Images of whole H&E stained lung slices were acquired at 16x magnification on a Leica DMRA microscope (*Leica Microsystems GmbH, Wetzlar, Germany*) with an image resolution of 2560 x 1920 pixels, producing square pixels 6.098µm in length. Pictures were taken using OpenLab (*PerkinElmer, Waltham, MA*).

Automated Airspace Measurements: Histology images (Figure 1A) were first converted to greyscale using a weighted sum of RGB values (Figure 1B) using MATLAB 2009b (*MathWorks, Natick, MA*). The greyscale image was then converted into a binary image using an automated threshold (Figure 1C). The automated threshold was determined as the point where the interclass variance between the greyscale values of foreground and background pixels was at a minimum [5].

For each histology image, which may include more than 1 histological section, the largest connected section of histology was isolated automatically for analysis. This was done by first applying a morphological closing operation (an erosion followed by a dilation, both using a 25x25 pixel structuring element) to separate the foreground from the background (Figure 1D). An erosion essentially strips off all of the boundary pixels (pixels belonging to object and adjacent to background), while a dilation adds adjacent background pixels to the object. A filling operation was then used to fill holes in the foreground region (Figure 1E). The largest connected region was selected as the section area (Figure 1F). The selected section area(s) were then applied to the binary image for further processing (Figure 2A).

Before individual airspaces could be measured from the binary image two processes were necessary: structures within the binary image were isolated and large airways and blood vessels were removed. Airspaces within the binary image were first isolated to ensure that connected paths of pixels did not exist between adjacent airspaces, airways and blood vessels (Figure 2B). Isolation of airspaces was achieved using a series of morphological closing operations utilizing structuring elements of decreasing size. Beginning with the largest structuring element (11x11 pixel), a morphological closing operation was applied to the binary image, isolating the largest areas. These areas were saved to a second binary image before being dilated by 1 pixel, to guarantee isolation, and subsequently removed from the original binary image. The process was repeated with increasingly smaller structuring elements, capturing smaller and smaller airspaces with

each iteration. The smallest objects that we defined as airspaces were 3x3 pixel squares, representing the smallest object that could survive a single erosion; objects smaller than this size were considered as noise. A user then identified the airways and blood vessels from the original histology image and they were automatically removed from the analysis (Figure 2C).

Following airspace isolation and the removal of airways and blood vessels the processed binary image was quantified. Every connected region within the processed binary image was taken to be an airspace. The total number of airspaces and the number of airspaces per unit slice area were measured for each lung slice. For each airspace, a series of parameters relating to size and shape were measured. Airspace area was proportional to the number of pixels comprising each airspace. Horizontal and vertical diameters were determined as the maximum number of pixels spanning the horizontal and vertical directions, respectively. The equivalent diameter was calculated from the airspace area, under the assumption that the airspace was circular. The perimeter of each airspace was calculated by counting the number of boundary pixels; boundary pixels were identified using an erosion operation. The area to perimeter ratio was calculated by dividing the airspace area by its perimeter. Additionally, airspace areas were binned into logarithmic ranges in order to examine their distribution. Values were expressed in units of microns (or square microns) by multiplying the value in pixels by the length in microns (or area in square microns) of each pixel.

Validation of Automated Method: To validate the automated airspace quantification method we compared it to the current gold standard for measuring airspace size, the mean linear intercept (L_m). The results from our method (*Pneumometrics, McMaster University, 2012*) were compared with L_m measurements from a lung development study in rats exposed *in utero* to nicotine [6]. The study demonstrated that *in utero* nicotine expose caused an increase in airspace size. Briefly, female Wistar rats received either saline or nicotine bitartrate (1 $mg \cdot kg^{-1} \cdot d^{-1}$) via subcutaneous injection daily from 2 weeks prior to mating until weaning at postnatal day 21. Lung tissue was collected from the pups at birth, 3, and 12 weeks of age. For details on lung fixation and sectioning refer to Petre et al [6]. The L_m measurements were made on high magnification pictures randomly sampled from each histology slide. Evenly spaced grid lines were drawn onto the high magnification image using a computer. The linear intercept, L_m, was calculated by dividing the total length of the gridlines by the number of intersections between the grid lines and airspace septa. For each subject, the L_m measurement were plotted against the percentage of total airspace area for airspaces between 10^4-10^5 μm^2, as determined using the automated method. Linear regression was performed to determine the degree of

correlation between the two measures of airspace enlargement. The sample sizes required for both the L_m method and the automated method was calculated for a type-1 error of 5% and a power of 80% (*www.stat.ubc.ca/~rollin/stats/ssize*).

Application of Automated Method: The automated airspace assessment was applied to histology images from two mouse models of COPD: porcine pancreatic elastase (PPE) exposure, which destroys lung parenchyma and creates enlarged airspaces similar to severe emphysema, and cigarette-smoke (CS) exposure, which causes inflammation and limited airspace enlargement. PPE-exposed female BALB/c mice (n=6) received 4 units of PPE (*Elastin Products Company, Owensville, MO*) in 30 µl of PBS delivered intranasally. Control animals (n=3) received PBS alone. Animals were sacrificed by exsanguination 45 days post-delivery. CS-exposed female BALB/c mice (n=6) were exposed to the smoke generated from 12 2R4F reference cigarettes (*University of Kentucky, Lexington, KY*), with the filters removed, for 50 minutes twice daily, 5 days/week using a SIU48 whole body exposure system (*Promech Lab, Vintrie, Sweden*) for 24 weeks. Control animals (n=4) were exposed to room air alone. Animals were sacrificed by exsanguination approximately 16 hours after the final cigarette smoke exposure. Airspace area measurements from the CS-data have been published previously [*Jobse et al., Accepted to the Journal of Nuclear Medicine, 10/10/12*]. Histology images were taken at low magnification (x16) to include the entire slice area within the field of view and analyzed using the method described above. To determine whether a whole slice analysis was more sensitive than an analysis using randomly selected regions of interest (ROI), we reanalyzed CS-exposed animals and their controls using computer-controlled random sampling. For each slice, 5 ROIs (500 µm x 500 µm) were randomly selected avoiding major airways and blood vessels; the ROIs were then analyzed in the same way as the whole slices.

Statistical Analysis: All statistical analyses were performed using GraphPad Prism 5 (*GraphPad Software, Inc., CA*). Airspaces from all four slices of each animal were pooled prior to analysis. Data were expressed as mean ± standard error of the mean (SEM). For the number of airspaces per unit area, the mean equivalent diameter, and the mean area to perimeter ratio, statistical analyses were performed using a two-tailed unpaired t-test. For the airspace area logarithmic histograms, we analyzed the bin which contained the largest percentage of total area for the controls using a two-tailed unpaired t-test. Linear regression was performed to determine the degree of correlation between the results of the automated method with the L_m measurements. A p-value of <0.05 was considered statistically significant.

Results:

To determine the validity of our automated method of assessing airspace size, we compared our results with the gold standard measurement, L_m, in a lung development model in rats (Figure 3A-B). An increase in airspace size, measured using the traditional L_m method, was observed at 3 weeks postnatal in rats exposed to nicotine, compared to controls. In the nicotine-exposed animals, we observed a significant loss of area for airspaces in the 10^4-10^5 μm^2 range and a shift towards larger sizes compared to controls using the automated whole slice method (Figure 3C). We found that L_m measurements were highly correlated (Figure 3D) with the percentage of total airspace area for airways between 10^4 and 10^5 μm^2 (R= -0.93, p=0.0003). Further, the number of animals required to achieve 80% power was six with the automated method compared to 12 for manual L_m measurements.

We used our automated method to evaluate whole lung sections from two animal models of airspace enlargement. Histological sections from the PPE exposure mouse model were analyzed using our automated method (Figure 4). This model represents an extreme case of parenchymal destruction and airspace enlargement. The number of airspaces per unit area was significantly decreased in the PPE-exposed mice compared to their controls; PPE-exposed animals had 68.3±8.5 airspaces/μm^2 and control animals had 146.3±2.7 airspaces/μm^2 (Figure 4B). The mean equivalent diameter and the mean area to perimeter ratio were both found to be significantly increased in the PPE-exposed mice compared to controls (Figure 4C-D). The distribution of airspace areas was also found to differ dramatically between the PPE-exposed mice and their controls (Figure 4E). Airspaces from PPE-exposed mice were shifted to larger sizes compared to controls. The percentage of airspace area falling into the 10^3-10^4 μm^2 range was significantly lower for the PPE-exposed group (14.5±2.3%) compared to controls (57.4±1.3%). The automated method was also used to analyze histological sections from a cigarette-smoke (CS) exposure model in mice (Figure 5). The number of airspaces per unit area was significantly decreased in the CS-exposed mice compared to controls; CS-exposed animals had 142.1±1.7 airspaces/μm^2 and control animals had 163.8±6.6 airspaces/μm^2 (Figure 5B). No difference was found between either the mean equivalent diameter or the mean area to perimeter ratio between CS-exposed and control mice (Figure 5C-D). The distribution of airspace areas was found to differ between the CS-exposed mice and their controls; airspaces from CS-exposed mice were shifted to larger sizes compared to controls (Figure 5E). The percentage of airspace area falling into the 10^3-10^4 μm^2 range was significantly lower for the CS-exposed animals (53.5±1.1%) compared to controls (59.6±1.2%). To assess whether our whole-slice analysis was more sensitive than an analysis limited to small ROIs, we repeated the analysis using randomly selected regions

of interest. Although an ROI analysis was able to detect an increase in airspace size in the PPE animals (data not shown), it was unable to detect a significant difference between the CS-exposed animals and their controls (Figure 6). The whole slice analysis showed a significant decrease in the number of airspaces per unit area and a significant decrease in the range with the highest percentage of total area for the control animals; these changes were not detected using an ROI analysis.

Discussion:

We have introduced a novel method for automated airspace analysis that utilizes lower magnification images, allowing us to objectively analyze entire lung sections. The technique has been able to discriminate not only between obvious cases of airspace enlargement, such as the PPE model, but also cases where the differences in size are very small, such as the CS model. The small differences in airspace size between CS animals and controls were not detectable using an ROI analysis; only when the entire slices were analyzed did these differences become measurable. Our method for quantifying airspace enlargement produced results similar to those obtained using traditional L_m analysis. Instead of limiting our analysis to small regions of interest, we were able to analyze complete histological sections. This avoids a major problem of sampling within sections, where regions of interest are not always selected randomly. In cases of heterogeneous lung disease it is possible for diseased areas to be missed or overestimated. Our whole-slice analysis revealed a significant increase in airspace size that was not evident from an analysis of randomly sampled ROIs. The lower values obtained using the ROI analyses were probably due to the exclusion of larger airspaces. Calculations of required sample sizes revealed that our technique requires half the number of subjects compared to the traditional L_m technique to adequately power a study.

Several automated quantification schemes for analyzing lung histology have been developed previously but all rely on the analysis of small regions of interest [7-12]. Some of these techniques utilized a skeletonization algorithm which reduced the septal structures separating airspaces into single pixel paths [7-8]. The use of a skeletonization algorithm, however, could result in the over-estimation of airspace area due to decreased septal thickness. In contrast, the algorithm we use to isolate airspaces ensures that they retain their original size; it also allows for large airways and blood vessels to be easily excluded from the analysis, facilitating whole slice analysis.

We have developed an automated method for quantifying airspace enlargement in whole histological lung slices. The method largely eliminates sampling bias and reduces analysis time from hours to minutes and decreases the number of animals required in a

study. Our measurements of airspace size distribution correlated well with L_m measurements. The automated method successfully detected and quantified airspace enlargement in two animal models of COPD: porcine pancreatic elastase exposure and cigarette-smoke exposure. In both models the software was able to quantify statistically significant differences in airspace size, even in the cigarette-smoke exposure model, where the changes are not obvious to the human eye or by using an ROI analysis. This method represents a more objective system compared to current standards and can provide a better understanding of lung structure under pathological conditions.

Acknowledgements:

The authors would like to thank Dr. M. Stampfli and J. Kasinska for use and technical expertise with the smoke exposure system.

References:

[1] Anciaes AM, Olivo CR, Prado CM, Kagohara KH, Pinto TS, Moriya HT, Mauad T, Martins MA, Quirino FDT. Respiratory mechanics do not always mirror pulmonary histological changes in emphysema. *Clinics 2011; 66(10): 1797-1803*

[2] Kuppenvelt TH, Robbesom AA, VersteegENM, Veerkamp JH, Herwaarden CLA, Dekhuijzen PNR. Restoration by vacuum inflation of original alveolar dimensions in small human lung specimens. *Eur Respir J 2000; 15: 771-777*

[3] Hsia CCW, Hyde DM, Ochs M, Weibel ER. An Official Research Policy Statement of the American Thoracic Society/European Respiratory Society: Standards for Quantitative Assessment of Lung Structure. *Am J Respir Crit Care Med Vol 181. pp. 394-418, 2010*

[4] Knudsen L, Weibel ER, Gundersen JG, Weinstein FV, Ochs M. Assessment of air space size characteristics by intercept (chord) measurements: an accurate and efficient stereological approach. *J Appl Physiol 108: 412-421, 2010*

[5] Otsu N. A Threshold Selection Method from Gray-Level Histograms. *IEEE Transactions on Systems, Man, and Cybernetics, Vol. 9, No. 1, 1979, pp. 62-66*

[6] Petre MA, Petrik J, Ellis R, Inman MD, Holloway AC, Labiris NR. Fetal and Neonatal Exposure to Nicotine Disrupts Postnatal Lung Development in Rats: Role of VEGF and Its Receptors. International Journal of Toxicology 2011, 30(2) 244-252

[7] Parameswaren H, Majumbar A, Ito S, Alencar AM, Suki B. Quantitative characterization of airspace enlargement in emphysema. *J Appl Physiol 100: 186-193, 2006*

[8] Tschanz SA, Burri PH. A New Approach To Detect Structural Differences In Lung Parenchyma Using Digital Imaging. Experimental Lung Research 28:457-471, 2002

[9] Jacob RE, Carson JP, Gideon KM, Amidan BG, Smith CL, Lee KM. Comparison of Two Quantitative Methods of Discerning Airspace Enlargement in Smoke-Exposed Mice. *PLOS One August 2009, Vol.4, I.8,e6670*

[10] Namati E, Thiesse J, Ryk J, McLennan G. Alveolar Dynamics during Respiration: Are the Pores of Kohn a Pathway to Recruitment? *Am J Respir Cell Mol, Vol 38, pp.572-578, 2008*

[11] Gomes RFM, Shardonofsky F, Eidelman DH, Bates JHT. Respiratory mechanics and lung development in the rat from early age to adulthood. *J Appl Physiol 90: 1631-1638, 2001*

[12] Lundblad LKA, Thompson_Figueroa J, Leclair T, Sullivan MJ, Poynter ME, Irvin CG, Bates JHT. Tumor Necrosis Factor-α Overexpression in Lung Disease. *Am J Respir Crit Care Med Vol 171. Pp 1363-1370, 2005*

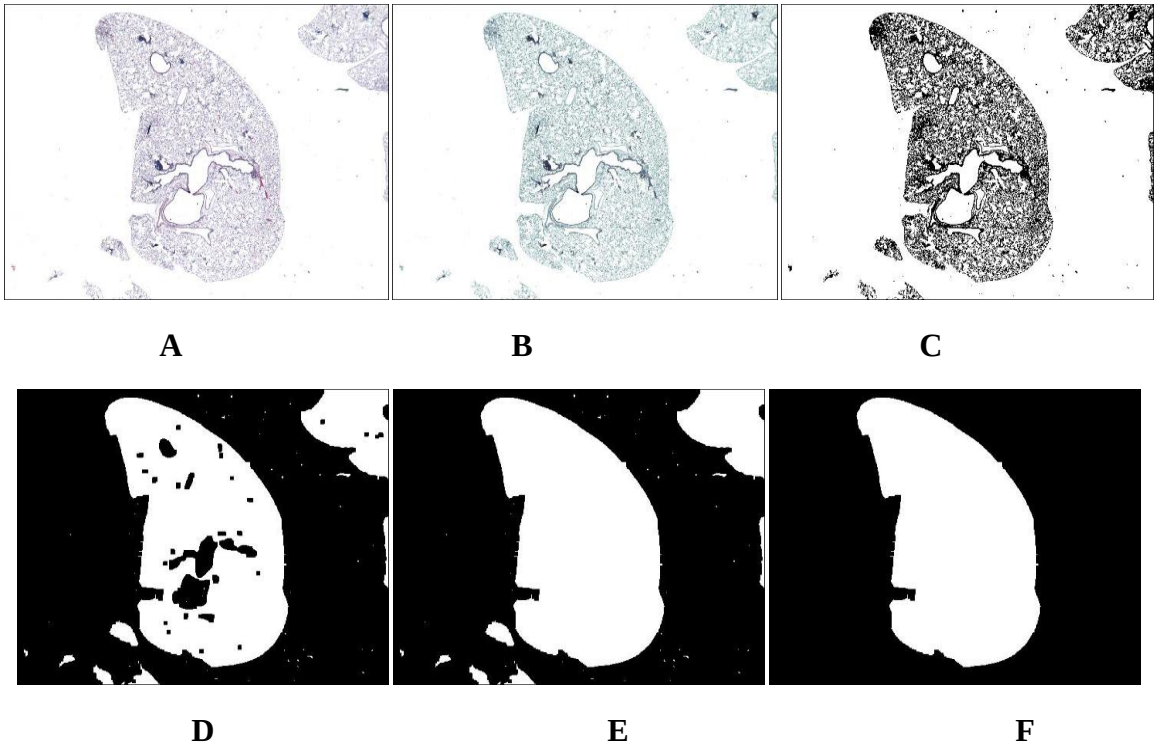

FIGURE 1: Histological Image Processing. A) Original image. B) Greyscale image. C) Binary image. D) Separation of foreground (lung) and background. E) Holes in the foreground region are filled. F) Largest foreground region (ROI) is select.

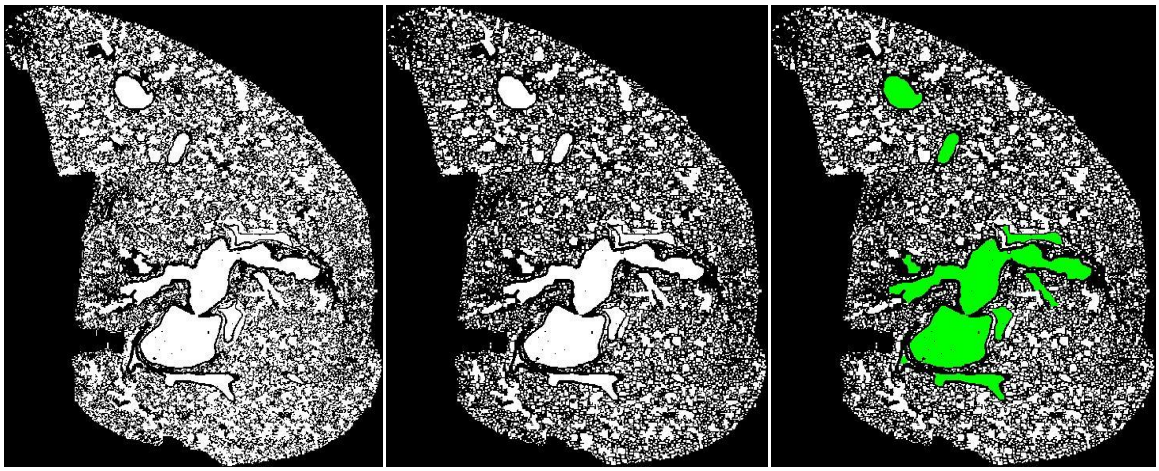

A **B** **C**

FIGURE 2: Airspace isolation and vessel removal. A) ROI applied to binary image. B) Isolation of airspaces. C) Large airways and blood vessels are removed.

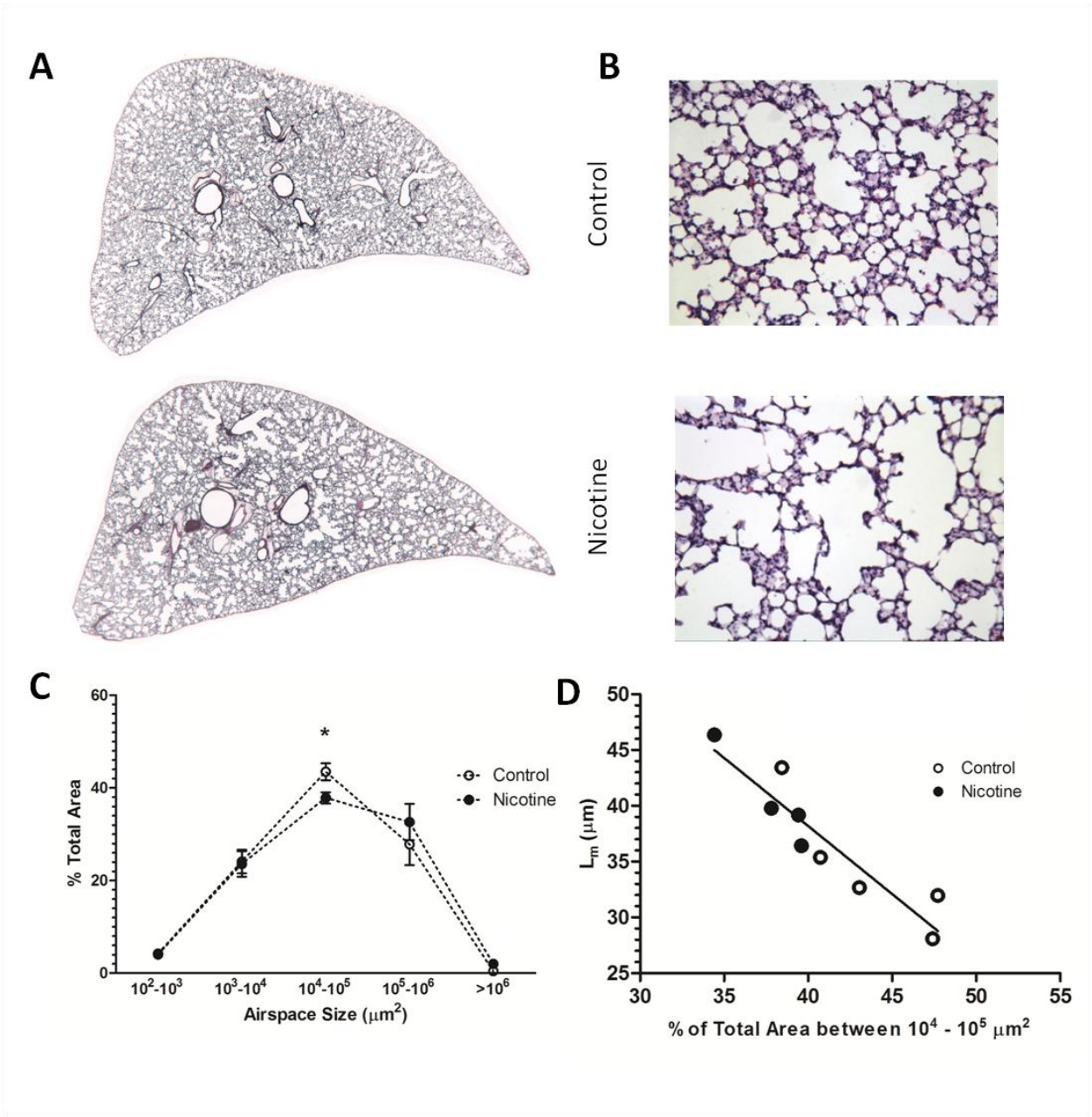

FIGURE 3: Comparison of airspace size from the automated method with linear intercept measurement. A) Representative low magnification slice from a control (top) and nicotine-exposed (bottom) animal. B) Representative high magnification ROI from a control (top) and nicotine-exposed (bottom) animal. C) Distribution of airspace areas determined by our software using low magnification images. D) Correlation between L_m measurement and the percentage of airspace area for airspaces between 10^4 and 10^5 μm^2 ($R= -0.93$, $p=0.0003$, $n=9$). *****$p<0.05$ vs. age-matched control by two-tailed unpaired t-test.

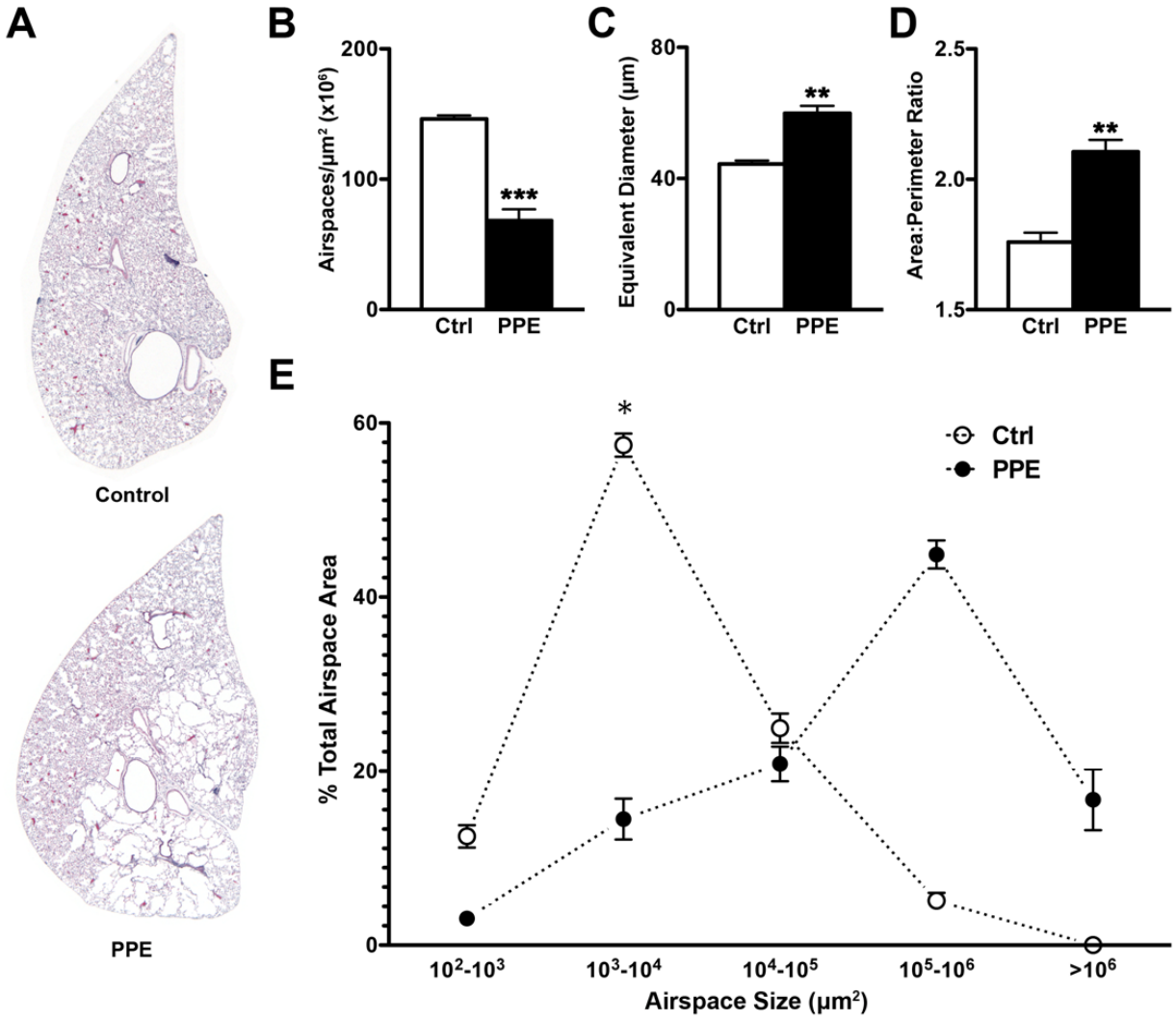

FIGURE 4: Application to porcine pancreatic elastase (PPE) model. A) Representative slice from a control (top) and a PPE-exposed (bottom) animal. B) Number of airspaces per unit area. C) Equivalent diameter. D) Area to perimeter ratio. E) Distribution of airspace area. ***p<0.05, ****p<0.01, *****p<0.005 vs. age-matched control by two-tailed unpaired t-test (PPE: n=6, control: n=3).

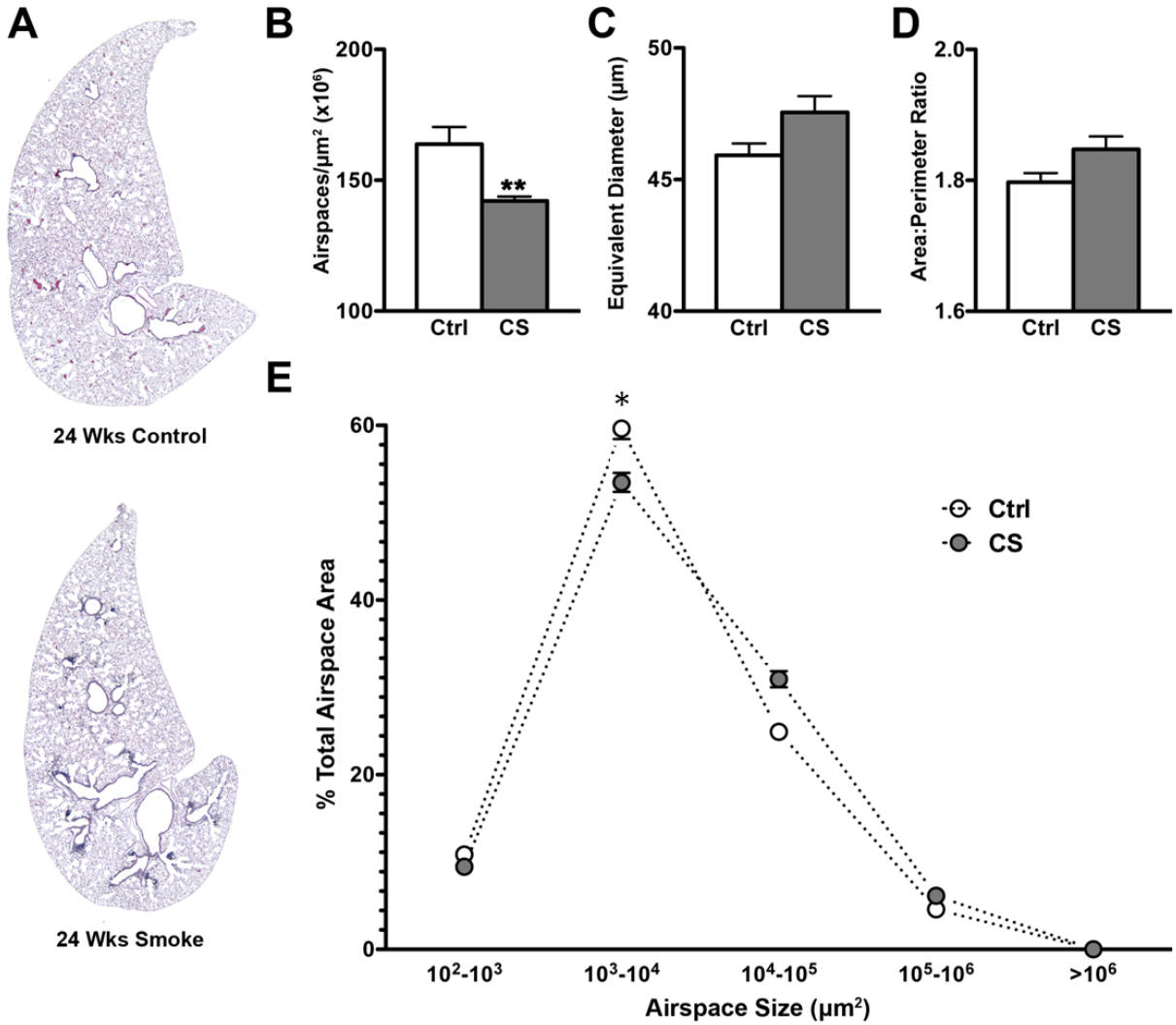

FIGURE 5: Application to cigarette smoke (CS) model. A) Representative slice from a control (top) and a CS-exposed (bottom) animal. B) Number of airspaces per unit area. C) Equivalent diameter. D) Area to perimeter ratio. E) Distribution of airspace area. *p<0.05, **p<0.01 vs. age-matched control by two-tailed unpaired t-test (CS: n=6, control: n=4).

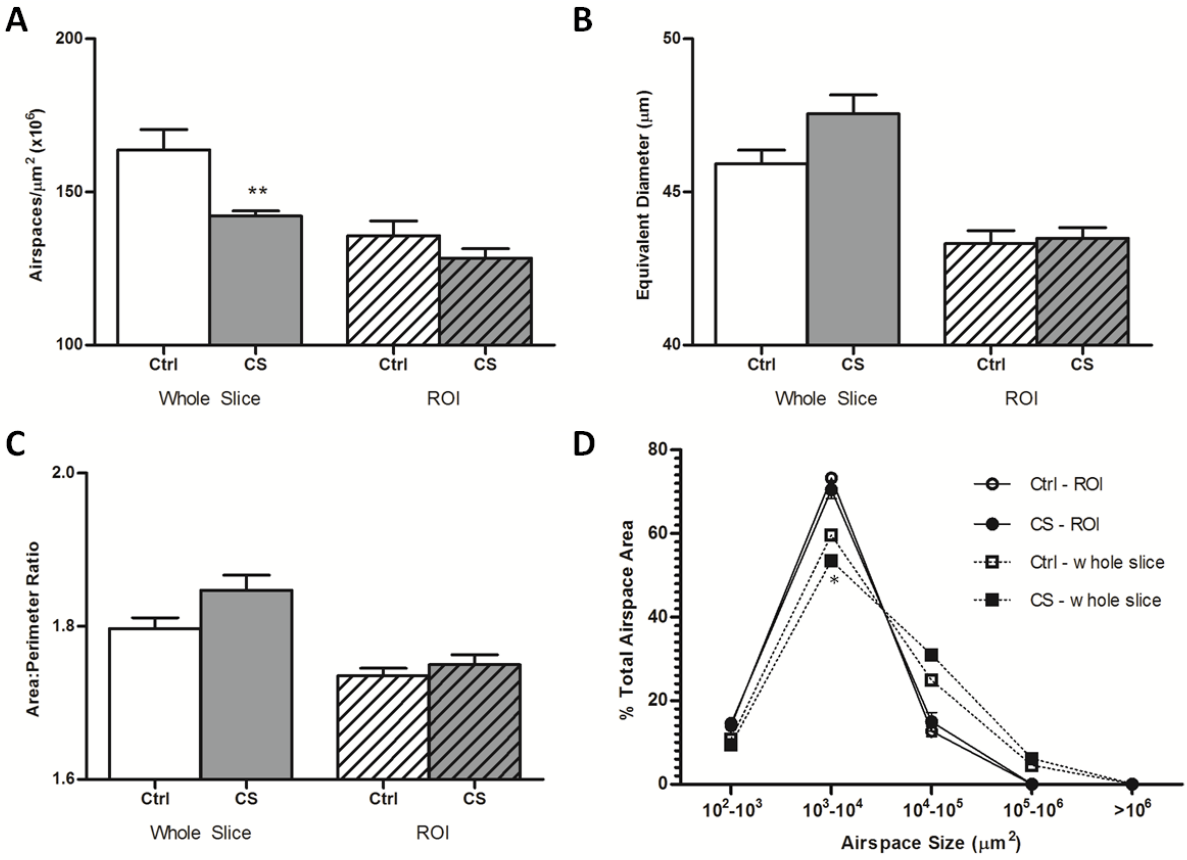

FIGURE 6: Comparison between whole-slice analysis and region of interest (ROI) analysis. A) Number of airspaces per unit area. B) Equivalent diameter. C) Area to perimeter ratio. D) Distribution of airspace area. *p<0.05, **p<0.01 vs. age-matched control by two-tailed unpaired t-test.

6 Simulating Particle Deposition and Bronchoconstriction in a Rodent Lung Model

6.1 Synopsis

The lung model introduced in chapter 3 has been used to simulate particle deposition and bronchoconstriction within the rodent lung. Further, by combining the two, the model has been used to simulate methacholine challenges in rodents. These challenges are used to study the changes in airway resistance following inhalation of methacholine. The technique is used clinically to assess asthma severity. In this work, the effects of different parameters (flow rate, particle size, etc.) on particle deposition and the resulting bronchoconstriction have been investigated. The results from the simulations largely agree with current theory. Validation of these simulations has been left for future work.

6.2 Contribution to Manuscript

As primary author, I, WB Counter, developed the methods for simulating particle deposition and bronchoconstriction. I wrote all the software and wrote the manuscript. TH Farncombe provided imaging expertise; MD Inman provided expertise in lung anatomy/physiology and in bronchoconstriction; NR Labiris provide expertise in lung anatomy/physiology and in particle deposition and edited the manuscript.

6.3 Manuscript

This manuscript has not been submitted for peer review. It has been presented as a poster at the American Thoracic Society Internal Conference 2012 in San Diego. References are listed in the order that they appear within the manuscript.

Simulating Particle Deposition and Bronchoconstriction in a Rodent Lung Model

WB Counter[1,2], TH Farncombe[3,4], MD Inman[1], NR Labiris[1,4]

[1] Department of Medicine, McMaster University; [2] Department of Medical Physics, McMaster University; [3] Department of Radiology, McMaster University; [4] Department of Nuclear Medicine, Hamilton Health Sciences, McMaster University, Hamilton, Ontario, Canada

Author Contributions:
WBC designed the concept and software, and wrote the manuscript; THF provided imaging expertise and editing of the manuscript; MDI provided expertise in lung structure/physiology; NRL provided study concept/design, expertise in lung structure/physiology, aided in data analysis, provided financial support, and editing of manuscript.

Financial Support: N.R. Labiris holds an Internal Department of Medicine Career Award

Running Head: Modelling Particle Deposition and Bronchoconstriction

Word Count: 2843

Correspondence: Name: Dr. Renée Labiris
Mailing Address: 1280 Main St. W., Hamilton, Ontario, L8S 4K1, Health Science Centre, rm. 1V11
Phone: 905 521-2100 ext. 75657
Fax: 905 546-1125
Email Address: labir@mcmaster.ca

Abstract:

Objectives: Asthmatics often show an increased sensitivity to inhaled methacholine resulting in increased levels of bronchoconstriction within the lung. These methacholine challenges are also used in asthma research to study the efficacy of various treatment options. Using a previously developed rodent lung model, we aimed to simulate the deposition of inhaled methacholine, the resulting bronchoconstriction patterns, and the associated increase in total airway resistance.

Materials and Methods: Equations governing the probability of an inhaled particle depositing by impaction, sedimentation, or diffusion were used to predict deposition patterns in a rodent lung model. A dose response curve was used to translate the number of particles deposited per unit area into a decrease in airway calibre for all airways in the lung model. Total resistance was calculated, using Poiseuille's law, at baseline and following increasing doses of methacholine to simulate a methacholine challenge. The effects of particle size on total deposition fraction and on deposition by generation were also investigated. In addition, differing bronchoconstriction patterns were investigated to determine their effect on overall increases in total airway resistance.

Results: Using a model of the rodent lung, we were able to simulate both the deposition of inhaled methacholine and estimate its effects on total airway resistance, effectively simulating a methacholine challenge. According to our results, deposition fractions were highest for both the very small and very large particle sizes, while intermediate sized particles were found to have the lowest deposition fractions. The investigation of differing bronchoconstriction patterns suggested that bronchoconstriction must be widely distributed throughout the lung in order to cause significant increases in total airway resistance and that bronchoconstriction of airways from the intermediate generation numbers contributed the most to increases in total airway resistance.

Conclusions: Simulating particle deposition and bronchoconstriction in small animals will provide insight into asthma research and possibly reduce the number of animals required for certain studies. The simulation is configured in a way that increases in knowledge of various aspects, such as muscarinic receptor density, can easily be accounted for.

Key Words: Pulmonary, Airways, Drug Deposition, Lung, Mathematical Model, Rodent, Bronchoconstriction, Disease simulation

Introduction:

Constrictive airway diseases such as asthma increase airway resistance and make breathing more difficult [1]. Airway resistance is increased by the constriction, or a reduction in diameter, of airways within the lung. It is believed that the smooth-muscle layer surrounding the airways plays a major role in regulating airway tone [2]. Asthma is often characterized clinically by measuring the response to inhaled agonists such as methacholine. An asthmatic will experience a greater degree of airway constriction for a given agonist dose than a normal subject [3]. These methacholine challenges can provide valuable information in assessing varying degrees of asthma severity. In animal models of diseases such as asthma, airway resistance is measured following increasing doses of inhaled methacholine. Although these resistance measurements provide valuable functional information, they do not give researchers any information as to which airways are being constricted and to what degree.

Lung impedance, comprised of both resistance and compliance, represents the force one must overcome to inflate the lung [4]. Airway resistances can be calculated for cylindrical tubes according to Poiseuille's law, where resistance is inversely proportional to the fourth power of diameter. It is also possible to add the resistances of individual airways to calculate total resistance for the entire network of pulmonary airways. Analogous to how resistors add in circuit theory, resistances in series add directly and resistances in parallel add inversely.

A mathematical model of the rodent airways has been developed in our lab based on measurements from contrast-enhanced computed tomography (CT) images [WBC, paper 2]. The model uses a fractal-based volume-filling algorithm to generate branching structures within lobe-divided lung boundaries obtained from CT scans. It models the pulmonary airways as an interconnected network of cylindrical tubes down to the 20^{th} generation. Airway diameters are assigned based on the diameter of the parent airway and the branching angle between the parent and daughter airway.

An inhaled particle can be deposited in the lung via one of three mechanisms: impaction, sedimentation, and diffusion [5-10]. In the larger, more central airways, where air velocities are highest, impaction is the dominant method of deposition; in the peripheral airways, where airflow velocities are lowest, diffusion is the dominant mode of deposition. The probability of a particle moving through a cylindrical tube and depositing by impaction was modelled by Thomas in 1958 [11]. The probability of a particle depositing by sedimentation was modelled by Gormley and Kennedy in 1949 [12]. Finally, the probability of a particle depositing by diffusion was modelled by Zhang et al. in 1997 [13]. The total probability that a particle will be deposited can be

determined by combining the individual probabilities for impaction, sedimentation, and diffusion [14].

Bronchoconstriction of the pulmonary airways is caused by a contraction of the smooth muscle layer surrounding the airways. Muscarinic receptor agonists, such as Methacholine, cause contraction of airway smooth muscle [15]. Inhaled methacholine binds to receptors on the smooth muscle cells causing contraction of the smooth muscle and resulting in bronchoconstriction. Clinically they are used to assess asthma severity in what is known as a methacholine challenge. Increasing doses of methacholine are inhaled and result in increases in airway resistance. Asthmatics often show both a hyper-sensitivity and a hyper-reactivity to the inhaled methacholine. Animal models of lung disease also use inhaled methacholine to study the effect of various treatment options [16]. Resistance is measured by connecting animals to a small animal ventilator. Several research groups have attempted to determine the relative concentrations of muscarinic receptors within various sizes of airways [17-22]. McNamara et al. used high-resolution computed tomography (HRCT) of excised canine lungs to study what size of airways were most contracted following administration of nebulized carbachol [19]; the greatest decrease in luminal areas was seen in the intermediate-sized airways. Bai et al. used phase-contrast microscopy to monitor changes in airway lumen area in mice exposed to methacholine and several other agonists [20]. Airways were grouped by generation number and they observed the greatest degree of airway contraction occurred in the intermediate generations. Kelly et al. administered the bronchodilator salbutimol to adult humans and used HRCT to measure changes in airway diameter [21]. They found the largest increases in luminal diameters to be in the smallest airways. Amirav et al. also used computed tomography to measure changes in airway diameter following an IV injection of methacholine [22]. Airways were grouped by diameter and no significant difference in airway constriction was observed between the different groups. It is entirely possible that the perceived effects of any inhaled agonist reflect the deposition of that agonist within the pulmonary airways and not a difference in muscarinic receptor density.

In this work, we present a method to simulate the deposition of inhaled methacholine within a model of the rodent lung. Airways are then constricted based on the concentration of particles deposited within them. We have used these techniques to simulate methacholine challenges in rodents and have developed software that allows the effects of various parameters involved in the deposition of inhaled particles and the resulting bronchoconstriction to be investigated.

Methods:

Rodent Lung Model

A model of the rodent airways, based on data collected from contrast-enhanced micro-CT images of the Sprague-Dawley rat, was used to model particle deposition and bronchoconstriction [Figure 1]. The rodent airways were modelled as a network of interconnected cylindrical tubes. It contained 20 generations of airways ranging from 2 to 0.02 mm. Airway diameters were assigned based on the relationship between the diameter of the parent airway and the angle between them [WBC, paper 2].

Flow Division

Particles are carried through the airways by the flow of inhaled air (Q). Air flow is conserved at each bifurcation.

$$Q_T = Q_1 + Q_2 \qquad \text{[Equation 1]}$$

The distribution of airflow between daughter segments was determined based on their relative diameters and branching angles [Figure 3A], assuming that two daughter airways with equal cross-sectional areas and branching angles will have equal airflow. The percentage of airflow entering each of the daughter branches was therefore determined using the following equation.

$$Q_i = (1/n)*(1 + Area_i/Area_T - \theta_i/\theta_T) \qquad \text{[Equation 2]}$$

Where n=2 for a bifurcation and n=3 for a trifurcation. $Area_T$ and θ_T represent the sum of cross-sectional areas and branching angles, respectively, for all of the daughter segments.

Particle Deposition

Particle deposition was determined within individual airways based on the probability of particles interacting by impaction (IMP_i), diffusion (DIF_i), or sedimentation (SED_i). These individual probabilities are described in Figure 3. The total probability of interaction was determined by combining the probabilities of each of the three interactions [Schmid et al., 2008].

$$P_i = 1 - (1-SED_i)(1-DIF_i)(1-IMP_i) \qquad \text{[Equation 3]}$$

If the number of particles traveling through an airway and the probability of deposition are known then the number of particles deposited in that airway can be calculated (Figure 3B). Particles that were not deposited continue into the next generation and were divided among the daughter airways according to the division of airflow. Mean airflow velocity was predicted as a function of generation number, and decreased with increasing generation number. Mean residence time was assumed to be related to both the mean airflow velocity and the length of the airway. The probability of particles depositing by impaction, diffusion, or sedimentation depends on both the Stokes number and the Reynolds number. Stokes number, which is the ratio of the stopping distance to the radius of the tube upstream, was calculated for each airway using Equation 4.

$$Stk_i = \rho 0 * da^2 * V_i/(9*\eta*D_i) \quad \text{[Equation 4]}$$

Where $\rho 0$ is the unit particle density, da is the particles aerodynamic diameter, V_i is the mean airflow velocity in that airway, η was the viscosity of air, and D_i is the airway diameter. The Reynolds number, which is the ratio of the inertial force of the gas to the frictional force of the gas moving over the surface, was calculated using equation 5.

$$Re_i = \rho a*D_i*V_i/\eta \quad \text{[Equation 5]}$$

The number of particles deposited in each airway was then determined for an administered dose of methacholine. The total number of particles per unit area was then determined by dividing the total number of deposited particles by the surface area of the open cylinder. The effects of particle size on total deposition fraction as well as on deposition by generation were investigated by varying the particle diameters form 0.001 to 10 μm. The effects of different flow rates on particle deposition were also investigated.

Bronchoconstriction

The total number of particles deposited per unit area was converted into a degree of bronchoconstriction within each airway using a dose response curve. Dose response curves were modelled using equation 6.

$$\text{Degree of Airway Narrowing} = \alpha*(1-\exp(-\beta*[\text{Methacholine}])) \quad \text{[Equation 6]}$$

where α represents the maximum degree of airway closure and β represents the sensitivity to methacholine. The maximum degree of airway closure was set to 50% the original luminal diameter. The effects of differing bronchoconstriction patterns were also investigated by limiting airway narrowing to individual lobes and to individual generation numbers.

Calculating Individual and Total Resistance

The resistance of individual airways were calculated using Poiselle's Equation.

$$\text{Resistance}_i = \Delta P/Q = 128\mu L_i/(\pi D_i^4) \quad \text{[Equation 8]}$$

Where μ is the dynamic viscosity of air and L_i and D_i are the airways length and diameter, respectively. The total resistance was then calculated for the entire airway tree. Similar to how resistances add in electronic circuits, when two airways are in series there resistances add and when two airways are in parallel there inverses are added.

$$\text{In series, } R_T = R_1 + R_2 + ... \quad \text{[Equation 9]}$$

$$\text{In Parallel, } 1/R_T = 1/R_1 + 1/R_2 + ... \quad \text{[Equation 10]}$$

Total resistances at varying levels of airway constriction were expressed relative to the total resistance at baseline luminal diameters.

Results:

A previously developed mathematical lung model was used to investigate the deposition of inhaled methacholine and the resulting decreases in airway diameters. In this study, the lung model was used to simulate a single inhalation.

The effects of particle size (aerodynamic diameter) on total deposition fraction were investigated for varying particle sizes (0.001-10 microns) and for 3 different airflow rates (0.1, 0.15, 0.2 L/min). At all flow rates, deposition fractions were found to be highest for particles less than 0.01 μm in diameter and for those greater than approximately 2 μm in diameter (Figure 4A). Particles within the intermediate size range were found to have the lowest probability of deposition. For the smaller sized particles, total deposition fraction was found to be higher at lower flow rates. The individual

probabilities for impaction, sedimentation, and diffusion were also graphed separately for a flow rate of 0.2 L/min. The dominate modes of deposition were found to be diffusion for the smallest sized particles, sedimentation for intermediate sized particles, and impaction for larger sized particles (Figure 4B).

Particle deposition within individual generations was also examined for varying particle sizes. Deposition within each generation was normalized to the total amount of deposited particles. Larger particles were deposited more centrally while smaller particles were deposited more peripherally. For these smaller particles, maximum deposition was found to be in generations 12 to 16, which represent the most numerous airways in the rodent lung. Only a very small difference in deposition patterns was observed for particle sizes of 0.1 μm and below. Figure 5 shows the deposition by generation for varying particle sizes.

The effects of varying bronchoconstriction patterns were also investigated by limiting changes in airway diameter to certain lobes (Figure 6A) and to certain generation numbers (Figure 6B). When bronchoconstriction was limited to individual lobes it had a much smaller effect on total airway resistance than when it was evenly distributed throughout the entire lung. In order to examine what generation of airways contributed the most to changes in total resistance we limited bronchoconstriction to individual generations of airways. Reduction of intermediate sized airways, generation 5-8, were found to contribute the most to changes in total airway resistance.

Methacholine challenges were simulated by first predicting the amount of inhaled methacholine deposited within each airway of the rodent lung model. The accompanying changes in airway diameter were predicted using a methacholine dose response curve (Figure 7A-B). One curve represented a healthy subject while a second curve represented a more sensitive asthmatic patient. Using this method we were able to simulate methacholine challenges between healthy and hyper-responsive rodents (Figure 7C). Asthma severity can therefore be modelled by increasing the parameter β in equation 6.

In addition, we have developed software which allows us to investigate the effects of numerous parameters on both particle deposition and changes in total airway resistance following an inhaled agonist (Figure 8). These parameters include the airway models orientation with respect to gravity, the particle size and number, the mean airflow velocity /flow rate, and the airway response to a given concentration of deposited particles.

Discussion:

Predicting particle deposition and the resulting changes in airway diameter within a rodent lung model allows us to simulate methacholine challenges in small animals. The fact that methacholine is delivered via a tracheotomy in these animals allowed deposition within the pharynx to be ignored, focusing only on deposition within the tracheobronchial airways.

Our particle deposition results are in good agreement with other published data examining deposition by particle size and generation number [23,24]. Total deposition fraction, which was found to be lowest for intermediate-sized particles, was consistent with the total deposition fractions obtained by other research groups for varying particle sizes [14,26,27]. Schmid et al. [14], Phalen et al. [26], and Hussain et al. [27] all showed total deposition fraction to be highest for particle sizes on both the low and high end, while medium-sized particles had the lowest deposition fraction. This pattern has also been confirmed in [5].

We examined the percent of the total number of deposited particles that were deposited in each generation. Larger particle sizes tended to deposit in lower generations (larger airways) while smaller particle sizes tended to deposit preferentially in higher generation (smaller) airways. Only minor differences in generational deposition were observed for particles ranging from 0.001 to 0.1 μm. These findings are consistent with the currently held notion that larger particles deposit more centrally while smaller particles deposit more peripherally.

To investigate the effects of various bronchoconstriction patterns we first compared airway constriction limited to individual lobes to airway constriction throughout the entire lung. Here we found that when bronchoconstriction was limited to individual lobes the increase in total airway resistance was minimal, regardless of which lobe experienced bronchoconstriction, compared to bronchoconstriction of the entire lung. This makes sense considering an individual with a collapsed lung can still breathe normally under resting conditions.

We also investigated which generations of airways contributed the most to changes in total airway resistance and found that bronchoconstriction of the intermediate generation numbers (5-8) lead to the largest increase in total airway resistance. This is in agreement with the current notion that the intermediate sized airways contribute the most to total airway resistance [28].

This method of simulating a methacholine challenge in small animals contains several parameters which are still not fully understood. It has been set up in a way, however, that future pieces of knowledge can easily be incorporated. We found no conclusive evidence in the literature that suggested that muscarinic receptor density varies

among different sizes or generations of airways. Although several studies showed a dependence on airway calibre or generation number this could reflect only the deposition of the inhaled agonist and not a difference in airway responses to equal concentrations of agonists. As the distribution of these receptors becomes clear, this model can easily be adapted to include the additional values. Another parameter which is not fully understood is the distribution of airflow velocities within the lung [29]. We have modelled mean airflow velocity as an exponentially declining function decreasing from its maximum value within the trachea. Some recent findings, however, have suggested that mean airflow velocity is highest in generation 3 airways before an exponential decline [30]. As our understanding of mean airflow velocity within the pulmonary airways improves it can be integrated into the simulations. As mentioned, the mean residence time of air within an airway was estimated from the mean airflow velocity and the length of the airway. Another parameter in question is the maximum degree of airway closure, α. For our simulations this was set to 50%, implying that all airways can only be constricted to half their initial diameter. Whether this is the true value for all airways or whether differing sizes of airways have different α-values is still unknown.

Our simulation occurs over the course of a single inhalation. Any methacholine that was not deposited would then be exhaled where it again has a chance to be deposited. Also, in our simulation, any molecule that was deposited was permanently attached to its receptor with no chance of influencing bronchoconstriction in other airways. In reality, however, it may be possible for a single particle to influence the calibre of multiple airways.

We have introduced a method for simulating methacholine challenges in small animals. Using a rodent lung model, we predicted the deposition of inhaled methacholine and the resulting decreases in airway calibre. We have based the simulations on current knowledge of airflow velocities and receptor densities but have allowed these parameters to be adjusted with further increases in knowledge. This work represents a considerable increase in our understanding of particle deposition in the rodent airways and how that particle deposition can influence airway calibre. These simulations will allow the effects of various parameters on particle deposition and bronchoconstriction to be investigated.

References:

[1] **Lutchen KR, Gillis H**. Relationship between heterogenous changes in airway morphometry and lung resistance and elastance. *American Physiological Society, 0161-7567/97 (1997)*

[2] **Martin JG, Duguet A, Eidelman DH**. The contribution of airway smooth muscle to airway narrowing and airway hyperresponsiveness in disease. *Eur Respir J 2000; 16: 349-354*

[3] **Politi AZ, Donovan GM, Tawhai MH**. A multiscale, spatially distributed model of asthmatic airway hyper-responsiveness. *Journal of Theoretical Biology 266 (2010) 614-624*

[4] **Bates JHT**. Lung Mechanics: An Inverse Modelling Approach. *Cambridge University Press, 2009*

[5] **Moren F, Dolovich MB, Newhouse MT, Newman SP**. Aerosols in Medicine: Principles, Diagnosis and Therapy. *Elsevier Science Publishers, Amsterdam, 1993*

[6] **Clarke SW, Pavia D**. Aerosols and the Lung: Clinical and Experimental Aspects. *Butterworth & Co., London, 1984*

[7] **Willeke K, Baron PA**. Aerosol Measurement: Principles, Techniques, and Applications. *Van Nostrand Reinhold, New York, 1993*

[8] **Newman SP**. Deposition and effects of inhalation aerosols. *Royal Free Hospital, London, 1983*

[9] **Labiris NR, Dolovich MB**. Pulmonary drug delivery. Part 1: Physiological factors affecting therapeutic effectiveness of aerosolized medications. *J Clin Pharmacol (2003) 56, 588-599*

[10] **Finlay WH, Martin AR**. Recent Advances in Predictive Understanding of Respiratory Tract Deposition. *Journal of Aerosol Medicine and Pulmonary Drug Delivery, Vol.21, No.2, 2008*

[11] **Thomas JW**. Gravity settling of particles in a horizontal tube. J Air Pollut Control Assoc. 1958; 8:32-33

[12] **Gormley PG, Kennedy M**. Diffusion from a stream flowing through a cylindrical tube. Proc R Irish Acad. 1949; 52A: 163-169

[13] **Zhang L, Asgharian B, Anjilvel S**. Inertial Deposition in the Human Upper Airway Bifurcations. *Aerosol Science and Technology 26: 97-110 (1997)*

[14] **Schmid O, Bolle I, Harder V**. Model for the Deposition of Aerosol Particles in the Respiratory Tract of the Rat. I. Nonhygroscopic Particle Deposition. *J Aerosol Medicine and Pulmonary Drug Delivery, Vol.21, No.3, 2008*

[15] **Amin SD, Majumbar A, Frey U, et al**. Modeling the dynamics of airway constriction: effects of agonist transport and binding. *J Appl Physiol 109: 553-563, 2010*

[16] **DiGiovanni FA, Ellis R, Wattie J**. Concurrent dual allergen exposure and its effects on airway hyperresponsiveness, inflammation and remodelling in mice. *Disease Models & Mechanisms 2, 275-282 (2009)*

[17] **Barnes PJ**. Distribution of Receptor Targets in the Lung. *Proc Am Thor Soc, Vol.1, pp.345-351, 2004*

[18] **Ueki J, Rhodes CG, Hughes MB, et al**. In vivo quantification of pulmonary β-adrenoceptor density in humans with (S)-[^{11}C] CGP-12177 and PET. *American Physiological Society, 0161-7567/93 (1993)*

[19] **McNamara AE, Muller NL, Okazawa M, et al**. Airway narrowing in excised canine lungs measured by high-resolution computed tomography. *American Physiological Society, 0161-7567/92 (1992)*

[20] **Bai Y, Zhang M, Sanderson MJ**. Contractility and Ca2+ Signaling of Smooth Muscle Cells in Different Generations of Mouse Airways. *Am J Respir Cell Mol Biol, Vol.36, pp. 122-130, 2007*

[21] **Kelly VJ, Brown NJ, King GG, et al**. The Bronchodilator Response of *In Vivo* Specific Airway Compliance in Adults with Asthma. *Annals of Biomedical Engineering (2010)*

[22] **Amirav I, Kramer SS, Gunstein MM**. Methacholine-Induced Temporal Changes in Airway Geometry and Lung Density by CT. *Chest 2001, 119: 1878-1885*

[23] **Lee Z, Berridge MS, Finlay WH, et al**. Mapping PET-measured triamcinolone acetonide (TAA) aerosol distribution into deposition by airway generation. *International Journal of Pharmaceutics 199 (2000) 7-16*

[24] **Yeh HC, Phalen RF, Raabe OG**. Factors Influencing the Deposition of Inhaled Particles. *Environmental Health Perspectives Vol.15, pp. 147-156, 1976*

[25] **Raabe OG, Al-Bayati MA, Teague SV, Rasolt A**. Regional Deposition of Inhaled Monodisperse Coarse and Fine Aerosol Particles in Small Laboratory Animals. *Ann. Occup. Hyg., Vol.32, pp. 53-63 Supplement 1, 1988*

[26] **Phalen RF, Oldham MJ, Wolff RK**. The Relevance of Animal Models for Aerosol Studies. *J Aerosol Medicine, Vol.21, No.1, 2008*

[27] **Hussain M, Renate WH, Werner H**. Effect of intersubject variability of extrathoracic morphometry, lung airways dimensions and respiratory parameters. *J Thorac Dis 2011; 3:156-170*

[28] **Levitzky MG**. Pulmonary Physiology. *Magraw-Hill,New York, 2007*

[29] **Kabilan S, Lin CL, Hoffman EA**. Characteristics of airflow in a CT-based ovine lung: a numerical study. *J Appl Physiol 102: 1469-1482, 2007*

[30] **Tena AF, Casan P, Marcos A, Barrio R, Blanco E**. Analysis of the fluid dynamic characteristics of the obstructive pulmonary diseases using a three-dimensional cfd model of the upper conducting zone of the lung airways. *Proceedings of the ECCOMAS Thematic International Conference on Simulation and Modeling of Biological Flow, Sept. 2011*

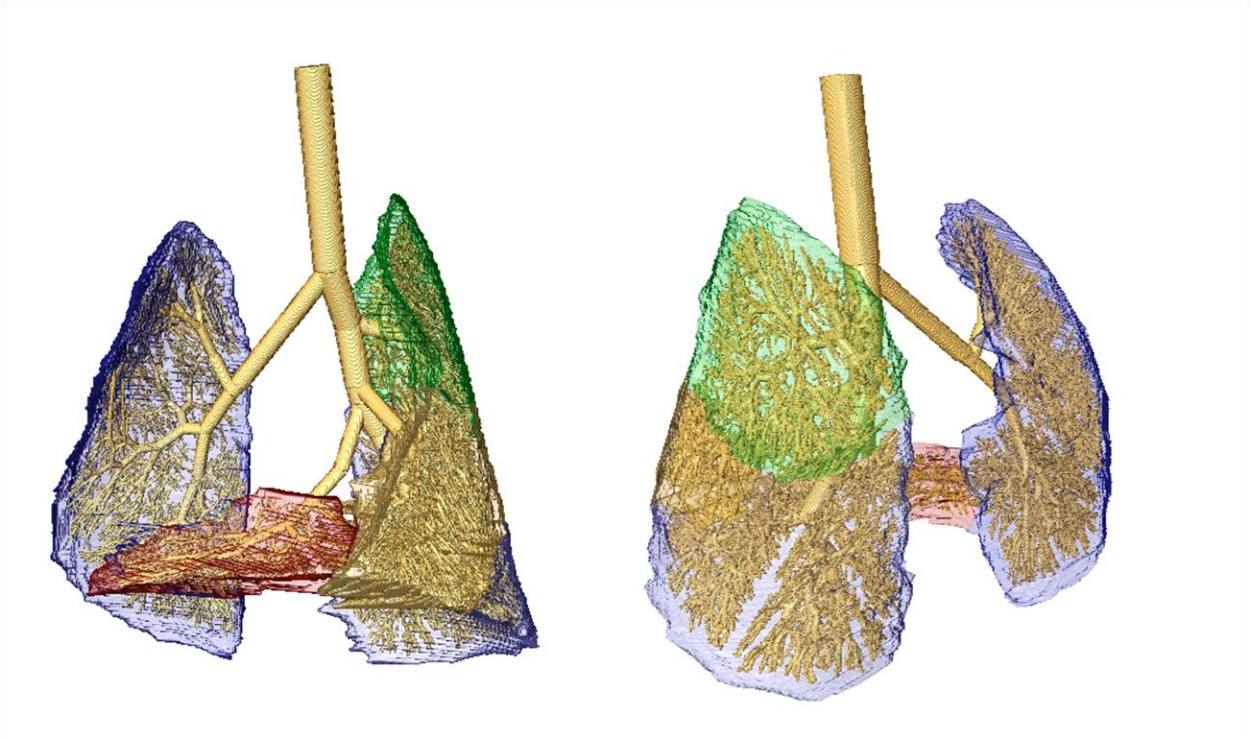

FIGURE 1: Rodent Airway Model. Lung model generated within individual lobe boundaries.

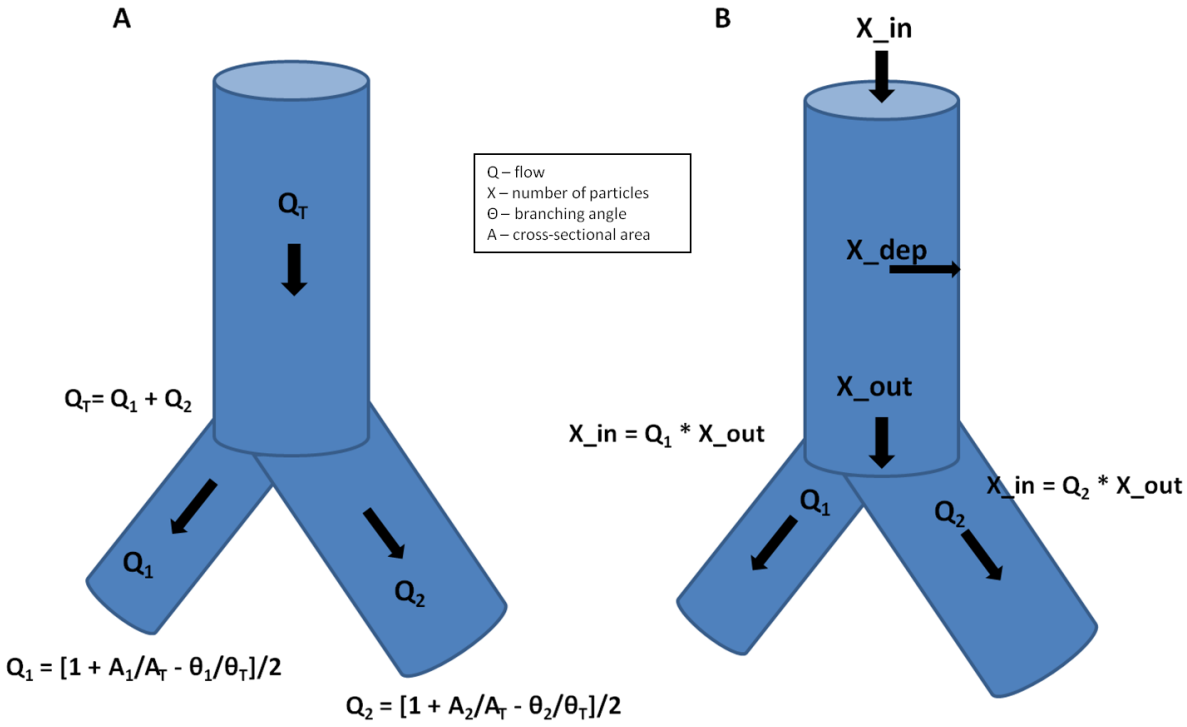

FIGURE 2: Airflow division and Particle Deposition at a Bifurcation. A) Flow division and B) Particle Deposition

Stokes Number, $Stk_i = \frac{\rho_0 \, {d_a}^2 \, v_i}{9 \, \eta \, D_i}$ **Reynolds Number,** $Re_i = \frac{\rho_a \, D_i \, v_i}{\eta}$

Impaction, $IMP_i = \begin{cases} = 0.0000654 \, exp(55.7 \, Stk^{0.954}) Re^{1/3} \sin\theta & for \, Stk < 0.04 \\ = [0.19 - exp(-9.5 Stk^{1.565})] Re^{1/3} \sin\theta & for \, Stk \geq 0.04 \end{cases}$

Sedimentation, $SED_i = \frac{2}{\pi}\left[2\varepsilon\left(1-\varepsilon^{2/3}\right)^{1/2} - \varepsilon^{1/3}\left(1-\varepsilon^{2/3}\right)^{1/2} + \arcsin\left(\varepsilon^{1/3}\right)\right]$

$$\varepsilon = \frac{3 \, v_g \, t_i \, sin\varphi_i}{4 \, D_i} \qquad v_g = \frac{\rho_0 \, {d_a}^2 \, g \, C(d_a)}{18 \, \eta}$$

$$C(d) = 1 + \frac{2\lambda}{d}\{1.207 + 0.440[-0.596 d/(2\lambda)]\}$$

Diffusion, $DIF_i = \begin{cases} = 0 & for \, Stk \geq 0.1, else \\ = 1.526\mu^{2/3} - 0.150\mu - 0.0342\mu^{4/3} & for \, \mu < 0.02, else \\ = 0.81905 \, e^{-3.6568\mu} + 0.09753 \, e^{-22.305\mu} + 0.0325 \, e^{-56.96\mu} + 0.01544 \, e^{-107.2\mu} \end{cases}$

$$\mu = \frac{D_p t_i}{{D_i}^2} \qquad D_p = \frac{kTC(d)}{3\pi\eta d_a}$$

Parameter	Description
D_i	airway diameter
v_i	mean airflow velocity in generation i
t_i	mean residence time of air in generation i
θ	branching angle
ϕ_i	angle between theta and earth's gravity
ρ_0	unit particle density (1 g/cm^3)
d_a	aerodynamic particle diameter
η	viscosity of air (1.833 x 10^{-3} dyn·s/cm^2)
λ	mean free path of air molecules (6.65 x 10^{-6} cm)
g	gravitational acceleration (9.81 m/s^2)
C(d)	Cunningham slip correction factor
D_p	particle diffusion constant
v_g	gravitational settling velocity of a particle
k	Boltzmann constant (1.381x10^{-16} dyn cm/K)
T	absolute temperature (293 K)

FIGURE 3: Equations used to determine portability of impaction, sedimentation, diffusion, and total deposition probability.

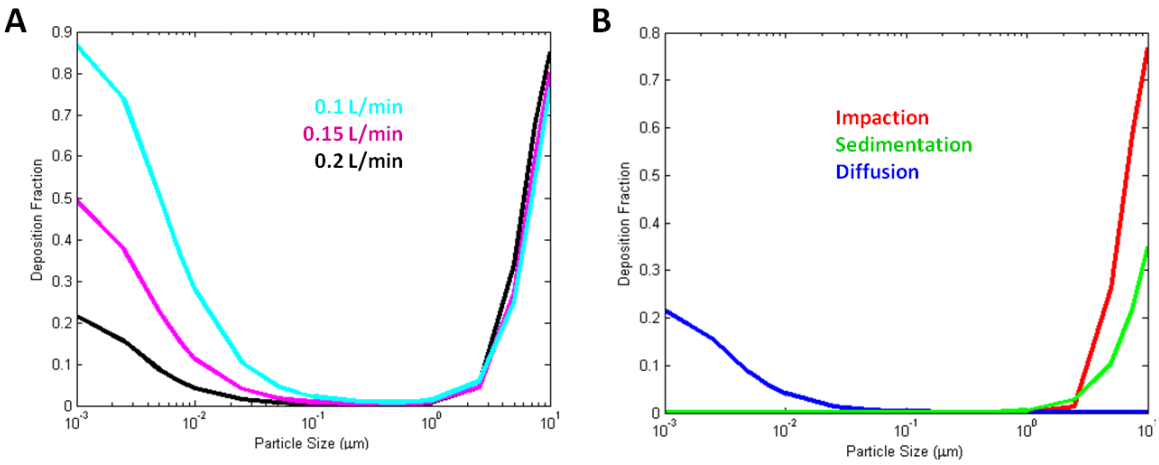

FIGURE 4: Total particle deposition by particle size. A) Deposition fraction for particle sizes from 0.001 micron to 10 microns for 3 different flow rates (0.1, 0.15, 0.2 L/min). B) Deposition fractions for particle sizes from 0.001 micron to 10 microns for impaction, sedimentation, and diffusion at 0.2 L/min.

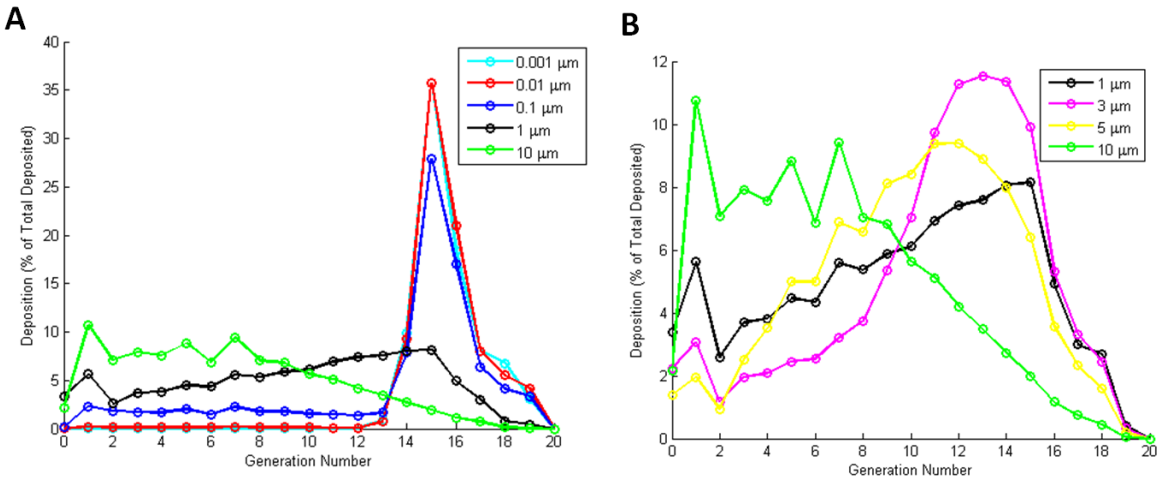

FIGURE 5: Particle deposition by generation for different sizes of mono-disperse particles. A) Deposition fraction by generation for particles sizes of 0.001, 0.01, 0.1, 1, and 10 microns. B) Deposition fraction by generation for particles sizes of 1, 3, 5, and 10 microns.

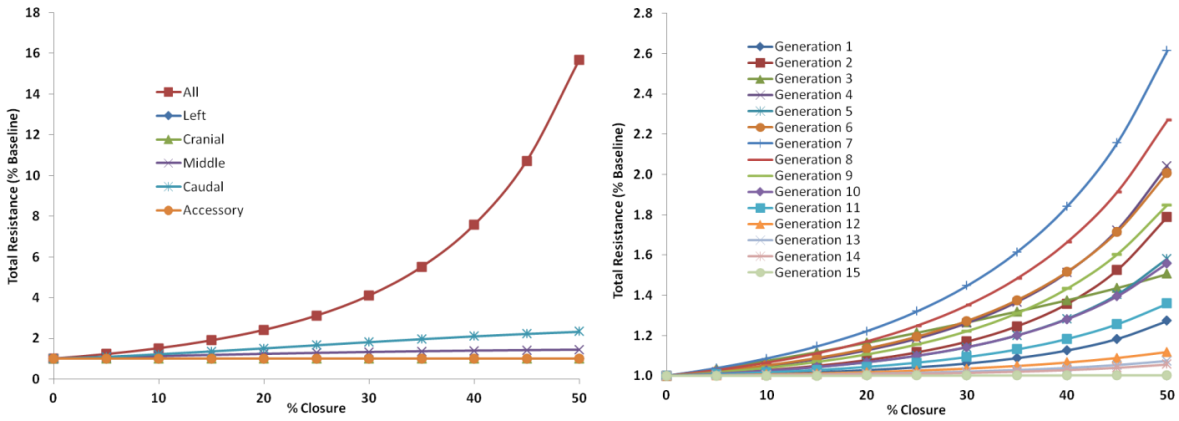

FIGURE 6: Effects of Regionalized Bronchoconstriction. A) Bronchoconstriction by Lobe. Segment diameters reduced from their baseline diameters to 50% of their baseline diameters in individual lobes versus all lobes. B) Bronchoconstriction by Generation. Segment diameters reduced from their baseline diameters to 50% of their baseline diameters for each individual generation number.

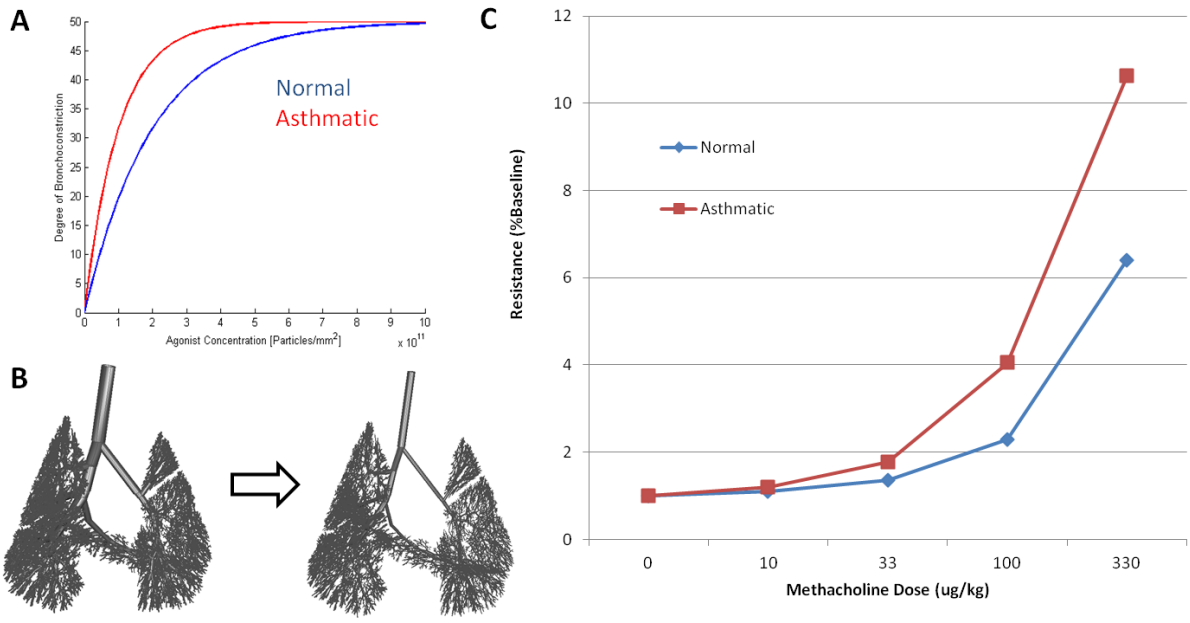

FIGURE 7: Simulated Methacholine challenge. A) Methacholine dose response curve used to convert the number of particles per unit area deposited within an airway into a degree of bronchoconstriction. B) Example airway model pre- and post-bronchoconstriction. C) Simulated methacholine challenge for a healthy versus an asthmatic subject.

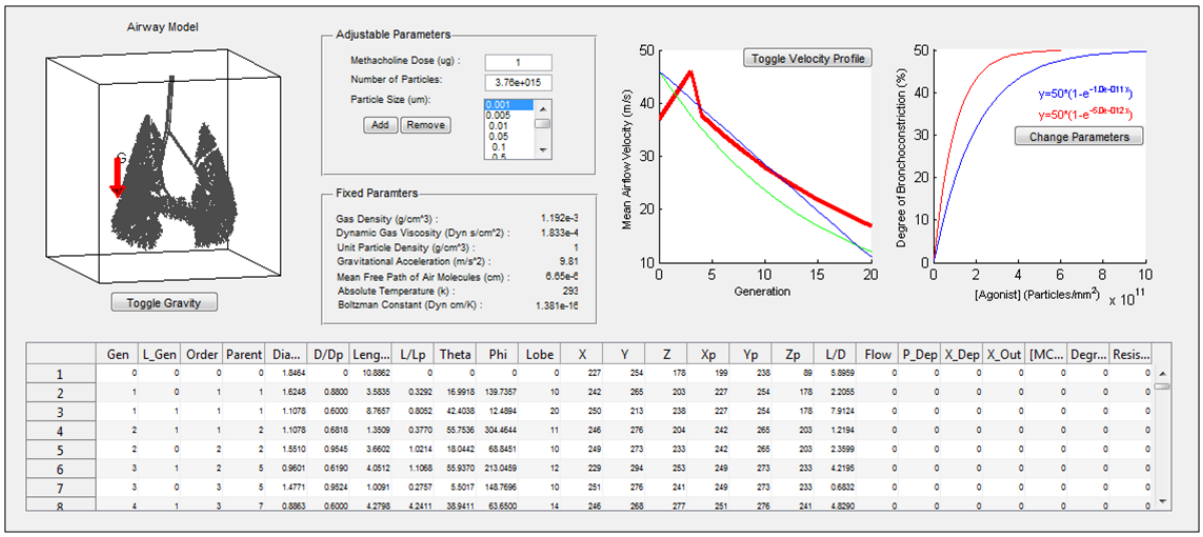

FIGURE 8: Graphical user-interface for investigating the effects of various parameters on particle deposition and bronchoconstriction. The effects of dose, particle size, flow rate and gravity on the deposition of inhaled particles can be investigated. Regional bronchoconstriction patterns and their effect on total airway resistance can also be investigated.

7 Discussion and Summary

7.1 Project Summary

The purpose of this work was to investigate rodent lung structure and thus provide a greater understanding of how structure and function are related in the rodent lung. The airways and vasculature of the rodent lung were first visualized and measured using contrast-enhanced CT. Measurements, including diameters, lengths, and branching angles, from both the Sprague-Dawley rat and the BALB/c mouse were determined and an anatomical rodent database was created. Segments were characterized by lobe, generation, and diameter.

A mathematical lung model, utilizing a fractal-based branching algorithm, was developed to allow its application to standard images of research animals (i.e., no contrast agents administered). The model also utilized anatomical parameters obtained from the contrast-enhanced CTs. As a starting point, the model requires segmentations of the lung volume and main airways, both of which can be obtained from an un-enhanced CT image. Airways, arterial, and venous trees were then generated within the lung boundary in a 1:1:1 ratio, implying that every airway segment has both a corresponding arterial and venous segment. Extensive validation revealed that the model was unable to fully reproduce the rodent lung and that further refinement is necessary [See Chapter 4].

This model contains what is often referred to as the conducting zone of the lung, namely the conducting airways and blood vessels which are responsible for moving both air and blood to and away from the centres of gas exchange, known collectively as the respiratory zone [1]. A valid model could be applied to unenhanced CT images of the lung and their corresponding functional images. Until now, functional imaging data has been analyzed by defining regions corresponding to the lungs and studying how voxel values within the lung change with time. Several studies have divided lung volumes into a series of concentric shells to regionalize functional data [130,131,133,134], but this is not a true reflection of lung anatomy. Using aspects of the model, we can now look at voxel values within individual lobes and around major airways. This should provide a first step to enabling the regionalization of data within medical images of the rodent lung. Additionally, the model can be used to determine the number of airways and blood vessels of a certain diameter or generation which would be expected within specific regions of the lung. The model has also been used to simulate the deposition of inhaled methacholine and the resulting patterns of airway constriction. It will allow others to study the effects of various parameters (particle size, flow rate, etc.) on particle deposition and bronchoconstriction.

The respiratory zone of the lung, where gas exchange actually takes place, is composed largely of alveoli and the surrounding capillary beds. The work done in chapter 5 focuses on quantifying a major component of the respiratory zone, the alveoli. Software (*Pneumometrics*) was developed that was capable of measuring the number, size, and shape of airspaces from complete histological sections. It was validated by re-analyzing histological lung data from a previous study [144]. The software was able to discriminate between healthy and emphysematous airspaces in an animal model of emphysema.

Together, the measurement and modeling of the conducting zone of the lung and measurements from the respiratory zone help to form a more complete picture of the rodent lung. This has increased our knowledge of the underlying lung anatomy which is very useful when examining structural and functional images of the lung. For example, when attempting to understand ventilation and perfusion values in the lung it is helpful to keep in mind the underlying anatomy. This can now be taken into account in future work. The micro-architecture of the lung is also important for understanding the connection between airspace enlargement and the resulting decreases in lung density measured via CT.

Large amounts of research have been dedicated to both the visualization of lung structure and to the creation of mathematical lung models. The work, besides moving away from the more widely studied human lung, represents a significant step in bridging anatomical lung measurements with mathematical lung models.

7.2 Further Applications

Before the applications of a rodent lung model can continue, it is necessary to further refine the proposed model. If development proceeds using a space-filling approach, then combinations of parameters (branching fraction, diameter assignment, etc.) need to be adjusted until a better agreement with the anatomical data is obtained. It is possible that the importance of various parameters change at different levels of the branching process. For example, diameters could be assigned differently to different generation numbers. Alternatively, development of the model could move away from a space-filling design, although this could limit its use in certain applications.

The applications of a valid mathematical rodent lung model are only limited by the imagination. In this work, the proposed model has been applied to the simulation of particle deposition and bronchoconstriction. In the future, a valid model will help to regionalize functional data and allow the simulation of certain respiratory diseases.

Such a mathematical model can be applied to CTs of unenhanced animals as well as the corresponding functional data. This provides a picture of the underlying lung anatomy and allows one to determine the approximate anatomical composition of various regions within the lung. By minimizing the amount of randomness used when generating the model, a user can reproducibly apply it to a group of animals or multiple time points of a single animal to provide reference locations within the image. This will allow users to chart disease progression relative to anatomical positions within the image. The model will also allow for the composition of structural components within given volumes to be predicted.

The ability to simulate various respiratory disorders provides insight into lung disease, and in certain cases, may reduce the number of research animals required for certain studies. So far, the airway component of the model has been used to simulate the deposition of inhaled methacholine, the ensuing changes in luminal diameter, and the resulting increase in total airway resistance. In these simulations, luminal diameter was allowed to decrease to 50% of its baseline diameter. Software has been created to allow others to study the effects of various parameters on particle deposition and bronchoconstriction. The model could also be used to simulate airway occlusions, where an entire airway is blocked and no inhaled material passes beyond the occlusion. The vascular components of the model could also be used to simulate various changes in vascular anatomy such as those caused by pulmonary arterial hypertension (PAH).

7.3 Limitations

Several limitations existed for the airway and vascular visualization. The first limitation involved the fact that airway and vascular measurements were not made simultaneously in the same animals, but instead were obtained from two distinct groups. Although it was found that air-filled airways did not provide enough contrast to visualize the entire airway tree, it was still possible to segment the larger airways in this case. Therefore, in an animal which received vascular contrast (airways were inflated with air) both the complete vasculature and largest airways could be segmented. From this, one can examine the relationship between main airways and vasculature. A second set of limitations resulted from the unavoidable use of contrast agents. To achieve adequate contrast, both the airway and vasculature enhancement required the animal being imaged to be sacrificed. The deposition of contrast agents also varied somewhat, especially during airway enhancement. A small gravity dependence was observed; contrast agents were found to preferentially deposit in regions of lower gravitational potential. In an attempt to eliminate this gravity dependence, we tried rotating the animal during contrast

agent delivery but with only limited success. The small fraction of missing vessels is excusable based on the intentions of this procedure. We did not set out to measure every vessel in the lung, but to get a sense of lung anatomy to form the basis of a mathematical model. Related to this point is another limitation occurring due to the resolution of the micro-CT. This limited the size of vessels that could be resolved and segmented from the image. The smallest vessels that we were able to measure had diameters of two voxels (0.23 mm for the rat, 0.16 mm for the mouse).

For the modeling of airways and pulmonary vasculature, several limitations also existed. The first is that the developed lung model was not specific to a given animal. Following acquisition of a CT image, the lung boundaries and main airways are used to generate a lung model for that image. The location of the airways and vasculature predicted by the model however, do not reflect the exact position of that animal's lung anatomy. Instead the model was meant to provide insight into where these vessels may be positioned and what structures are present within a given volume of the image. A further limitation of this modeling approach is that in certain disease states, such as extreme inflammation, regions corresponding to the lung boundary and major airways are often difficult to obtain. An experienced operator, however, should be able to segment these regions based on anatomical landmarks within the image (such as the ribs) and their knowledge of thoracic anatomy.

In chapter 4, airway models were generated for the rats and mice which had received contrast agents for airway visualization and measurement. The modeled airways were then compared to the anatomical measurements on an animal-by-animal basis. It was found that the model was unable to fully predict airway structure in all cases. This was indicated by a lack of agreement between the modeled data and the anatomical data for several of the animals. Additionally, the model also seemed to slightly overestimate airway diameter in the mouse. Significant and unexpected differences between the number of modeled and measured segments within in the larger diameter categories (D1-D2) also existed. The rather arbitrary nature of the diameter categories, however, probably makes comparison by generation the more robust of the two methods. As discussed, the creation of a more accurate model for the rodent lung could proceed in one of two major directions. The first would be to continue with a space-filling approach and to adjust combinations of parameters (branching fraction, diameter assignment, etc.) until better correlation is achieved. Alternatively, and depending upon the nature of the application, it may be possible to create a model which does not rely on a space-filling approach and as a result utilizes more of the collected anatomical measurements. In this analysis, the vascular component of the model was not compared to the anatomical vascular measurements due to the absence of supernumerary vessels and shunts in the model. This is certainly a major limitation of the lung model but I believe that agreement

between the airway and vascular components of the model is more important than precise agreement with the anatomical measurements.

For the quantification of airspace enlargement, several minor limitations also exist. It was found early that in order for the software to discriminate between subtle forms of airspace enlargement it was necessary for image contrast to be consistent across subjects. A huge part of this involves consistent slide staining. In cases where inconsistencies in slide contrast do exist, it is possible to employ an automatically-determined threshold for each image, which accounts for a large part of the inconsistency. When image contrast is consistent, it is preferable to use a single manually selected threshold and apply it to all slices. The purpose of this is to eliminate as many experimental variables as possible; in other words, to analyze every subject in the same way. It was also found that contrast could be increased post-acquisition in programs such as PhotoShop and that this improved the results, as long as the operation was performed consistently to all images.

7.4 Future Work

Visualization of Lung Structure: As technology relentlessly marches forward, increases in image resolution become inevitable. Although the current work utilized micro-CT to visualize and measure the airways and pulmonary blood vessels, it is more than likely that increases in CT instrumentation and computing speeds will allow even higher magnification images to be obtained. This will likely reduce or eliminate the need for contrast agents and allow animal-specific lung information to be obtained directly from the images. The elimination of contrast agents will make these procedures much less invasive and will allow animals to be studied over long periods of time, without the need to sacrifice.

Further Development and Validation of the Rodent Lung Model: As discussed, the proposed lung model was unable to produce a close agreement with the anatomical measurements in all of the animals tested. If the model development continues using a space-filling approach, then combinations of parameters (branching fraction, diameter assignment, etc.) need to be adjusted until a better agreement with the anatomical measurements is achieved. Perhaps using a set combination of parameters for all generations is not optimal; the branching fraction and diameter assignment, for example, could vary at different stages of the branching process. Alternatively, development could move away from a space-filling approach, although this may limit its ability to be applied in certain situations. Regardless of the direction taken, careful consideration should be

given to the models final purpose, as certain designs may be more or less appropriate for different objectives.

Applications of the Rodent Lung Model: The airway component of the model has already been used to simulate bronchoconstriction. The vascular component of the model still requires further exploration. It could potentially be used to simulate changes in vascular anatomy and to predict the distribution of blood vessels within specific regions of the lung. The potential exists for the lung model to be applied to a wide range of pre-clinical imaging studies. Its exact use in that study, however, will likely prove to be heavily dependent on the nature of the study. Preliminary applications of the model, such as the investigation discussed in chapter 7, demonstrate its ability to help regionalize imaging data. That analysis focused on regions acquired from CT images, but the technique could also be applied to regions acquired from SPECT or PET images. Continued applications of the model to various imaging studies should further refine the regionalization of both anatomical and functional data.

Quantifying Airspace Size: A provisional patent has been filed for the airspace quantification software, named *Pneumometics*. This software has been utilized successfully in our lab and in several others. The software was presented as a poster at the American Thoracic Society (ATS) International Conference 2012 in San Francisco. Full commercialization of the software requires further development.

Validation of Particle Deposition and Bronchoconstriction: Although most of the simulations performed involving particle deposition and bronchoconstriction agree with the current theory, significant work is required for validating many aspects of this work. First, particle deposition simulations must be validated. This would most likely involve radio-labeled methacholine and either a SPECT or PET scan. Many aspects of the bronchoconstriction simulations also require validation. The change in calibre of an airway to a given dose of methacholine can easily be studied ex vivo, but it is still uncertain if this truly reflects the *in vivo* situation. Additionally, the degree of maximum airway closure is still poorly understood. For these simulations airways were only allowed to decrease to 50% of their baseline diameter. Whether this is the true value and whether the value depends on the size or generation of airways is still unknown. It is also believed that at some critical point in its constriction, smaller airways can snap completely shut.

8 Additional References

[1] **Levitzky MG**. Pulmonary Physiology. *McGraw Hill Medical, New York, 2007*

[2] **Goldberger AL, West BJ**. Fractals in Physiology and Medicine. *The Yale Journal of Biology and Medicine 60 (1987), 421-435*

[3] **McNamee JE**, Fractal perspectives in pulmonary physiology. *American Physiological Society, 0161-7567/91*

[4] **Wang PM, Kraman SS**. Fractal branching pattern of the monopodial canine airway. *J Appl Physiol 96: 2194-2199, 2004*

[5] **Kamiya A, Takahashi T**. Quantitative assessments of morphological and functional properties of biological trees based on their fractal nature. *J Appl Physiol 102, 2315-2323, 2007*

[6] **Zamir M**, On Fractal Properties of Arterial Trees. *J Theor. Biol. (1999) 197, 517-526*

[7] **Kassab GS**. Scaling laws of vascular trees: of form and function. *Am J Physiol Circ Physiol 290: H894-H903, 2006*

[8] **Weibel ER**. Morphometry of the Human Lung. Berlin: Springer, 1963

[9] **Bai Y, Zhang M, Sanderson MJ**. Contractility and Ca2+ Signaling of Smooth Muscle Cells in Different Generations of Mouse Airways. *Am J Respir Cell Mol Biol, Vol.36, pp.122-130, 2007*

[10] **Jones NL**. The Ins and Outs of Breathing: How We Learnt about the Body's Most Vital Function. *iUniverse, Bloomington, IL, 2011*

[11] **Walker WF, Homberger DG**. Anatomy & Dissection of the Rat. *W.H. Freeman and Company, New York, 1997*

[12] **Huang W, Yen RT, McLaurine M, Bledsoe G**. Morphometry of the human pulmonary vasculature. American Physiological Society, 0161-7567/96

[13] **Jiang ZL, Kassab GS, Fung YC**. Diameter-defined Srahler system and connectivity matrix of the pulmonary arterial tree. American Physiological Society, 0161-7567/94

[14] **Horsfield K**, Diameters, generations, and orders of branches in the bronchial tree. American Physiological Society, 0161-7567/90

[15] **Paredi P, Barnes PJ**. The airway vasculature: recent advances and clinical implications. *Thorax 2009; 64:444-450*

[16] **Wallau BR, Schmitz A, Perry SF**. Lung Morphology in Rodents (Mammalia, Rodentia) and Its Implications for Systematics. *Journal of Morphology 246:228-248 (2000)*

[17] **Tolnai J, Szabari MV, Albu G, Maar BA, Parameswaren H, Bartolak-Suki E, Suki B Hantos Z**. Functional and morphological assessment of early impairment of airway function in a rat model of emphysema. *J Appl Physiol 112: 1293-1939, 2012*

[18] **Hantos Z, Adamicza A, Janosi TZ, Szabari MV, Tolnai J, Suki B**. Lung volumes and respiratory mechanics in elastase-induced emphysema in mice. *J Appl Physiol 105: 1864-1872, 2008*

[19] **Lai-Fook SJ, Houtz PK, Lai YL**. End-expiratory and tidal volumes measured in conscious mice using single projection x-ray images. *J Appl Physiol 104: 521-533, 2008*

[20] **ATS Board of Directors**. Standards for the Diagnosis and Care of patients with Chronic Obstructive Pulmonary Disease (COPD) and Asthma. Official Statement of the American Thoracic Society, 1986

[21] **Rabe KF, Hurd S, Anzueto A, Barnes PJ, Buist SA, Calverley P, Fukuchi Y, Jenkins C, Rodriguez-Rosin R, van Weel C, Zienlinski J**. Global Strategy for the Diagnosis, Management, and Prevention of Chronic Obstructive Pulmonary Disease: GOLD Executive Summary. *Am J Respir Crit Care Med Vol.176, pp.532-555, 2007*

[22] **Raghu G, Collard HR, Egan JJ, Martinez FJ, Behr J, Brown KK, Colby TV, Cordier JF, Flaherty KR, Lasky JA, Lynch DA, Ryu JH, Swigris JJ, Wells AU, Ancochea J, Bouros D, Carvalho C, Costabel U. Ebina M, Hansell DM, Jonkoh T, Kim DS, King TE, Kondoh Y, Myers J, Muller NL, Nicholson AG, Richeldi L, Selman M, Dudden RF, Griss BS, Protzko SL, Schunemann HJ**. An Official ATS/ERJ/JRS/ALAT Statement: Idiopathic Pulmonary Fibrosis: Evidence-based Guidelines for Diagnosis and Management. Am J Respir Crit Care Med, Vol.183, pp. 788-824, 2011

[23] **Bousquet J**. Global Initiative for Asthma (GINA) and its objectives. *Clinical and Experimental Allergy, 2000, Vol.30, S.1, p.2-5*

[24] **Edwards MR, Bartlett NW, Hussell T, Openshaw P, Johnston SL**. The microbiology of asthma. *Nature Review Microbiology, 2012; doi:10.1038/nrmicro2801*

[25] **Bousquet J, Clark TJH, Hurd S, Khalaev N, Lenfant C, O'Byrne P, Sheffer A**. GINA guidelines on asthma and beyond. *Allergy 2007, 62: 102-112*

[26] **McDonough JE, Yuan R, Suzuki M, Seyednejad N, Elliot WM, Sanchez PG, Wright AC, Gefter WB, Litzky L, Coxson HO, Pare PD, Sin DD, Pierce RA, Woods JC, McWilliams AM, Mayo JR, Lam SC, Cooper JD, Hogg JC.**. Small-Airway Obstruction and Emphysema in Chronic Obstructive Pulmonary Disease. *N Engl J Med 2011; 365: 1567-75*

[27] **Decramer M. Janssens W, Miravitlles M**. Chronic obstructive pulmonary disease. *Lancet, Vol 379, April 7, 2012*

[28] **Kornmann O, Beeh KM, Beier J, Geis UP, Buhl R**. Newly Diagnosed Chronic Obstructive Pulmonary Disease: Clinical Features and Distribution of the Novel Stages of the Global Initiative for Obstructive Lung Disease. *Respiration 2003; 70:67-75*

[29] **Gauldie J, Kolb M, Sime PJ**. A new direction in the pathogenesis of idiopathic pulmonary fibrosis? *Respir Res 2002, 3:1*

[30] **Maharaj SS, Baroke E, Gauldie J, Kolb MRJ**. Fibrocytes in chronic lung disease – Facts and controversies. *Pulmonary Pharmacology & Therapeutics, 2011, 1-5*

[31] **King TE, Pardo A, Selman M**. Idiopathic pulmonary fibrosis. *Lancet, Vol 378, December 3, 2011*

[32] **Hounsfield GN**. Picture Quality of Computed Tomography. *Am J Roentgenol 127: 3-9, 1976*

[33] **Bushberg JT, Seibert JA, Leidholdt EM, Boone JM**. The Essential Physics of Medical Imaging. *Lippincott Williams & Wilkins, Philadelphia, 2012*

[34] **Wesolowski JR, Lev MH**. CT: History, Technology, and Clinical Aspects. *Semin Ultrasound CT MRI 26: 376-379, 2005*

[35] **Hounsfield GN**. Potential Uses of More Accurate CT Absorption Values by Filtering. *Am J Roentgenol 131: 3-9, 1978*

[36] **Launders JH**. The Fundamentals of Computed Tomography. *Biomedical Instrumentation & Technology*

[37] **Madsen MT**. Recent Advances in SPECT Imaging. *J Nuc Med 2007; 48:661-673*

[38] **Brooks RA**. A Quantitative Theory of the Hounsfield Unit and Its Application to Dual Energy Scanning. *J Comput Assist Tomogr. 1977 Oct; 1(4): 487-93*

[39] **Wernick MN, Aarsvold JN**. Emission Tomography: The Fundamentals of PET and SPECT. *Elsevier Academic Press, Amsterdam,2004.*

[40] **Groch MW, Erwin WD**. Single-Photon Emission Computed Tomography in the Year 2001: Instrumentation and Quality Control. *J Nuc Med Technol 2001; 29:9-15*

[41] **Turkington TG**. Introduction to PET Instrumentation. *J Nucl Med Technol 2001: 29:1-8*

[42] **Phelps ME, Hoffman EJ, Mullani NA, Ter-Pogossian MM**. Application of Annihilation Coincidence Detection to Transaxial Reconstruction Tomography. *Journal of Nuclear Medicine, 1995, Volume 16, No.3*

[43] **Hoffman EJ, Phelps ME, Mullani NA, Higgins CS, Ter-Pogossian MM**. Design and Performance of a Whole-Body Positron Transaxial Tomograph. *J Nuc Med 17: 493-502, 1976*

[44] **Levin CS**. Primer on molecular imaging technology. *Eur J Nucl Mol Imaging (2005) 32:S325-S345*

[45] **Karstaedt N, Dixon RL, Wolfman NT, Ekstrand KE**. Nuclear Magnetic Resonance Imaging. *Surg Neurol 1983; 19:206-214*

[46] **Nishimura DG**. Principles of Magnetic Resonance Imaging. Stanford University, 2006

[47] **Ball JB, Pensak ML**. Fundamentals of Magnetic Resonance Imaging. *American Journal of Otology, Vol.8, No.1, January 1986*

[48] **Goldstein A**. Overview of the Physics of US. *RadioGraphics 1993; 13:701-704*

[49] **Dondelinger R**. Diagnostic Ultrasound. *Biomedical Instrumentation & Technology; Jan/Feb 2006; 40, 1, pp.39-44*

[50] **Ritman EL**. Micro-Computed Tomography-Current Status and Developments. *Annu. Rev. Biomed. Eng. 2004, 6: 185-208*

[51] **Franc BL, Acton PD, Mari C, Hasegawa BH**. Small-Animal SPECT and SPECT/CT: Important Tools for Preclinical Investigation. *J Nucl Med 2008; 49:1651-1663*

[52] **Ritman EL**. Current Status of Developments and Applications of Micro-CT. *Annu. Rev. Biomed. Eng. 2011, 13:531-52*

[53] **Vastenhouw B, Beekman F**. Submillimeter Total-Body Murine Imaging with U-SPECT-I. *J Nuc Med 2007; 48:487-493*

[54] **Johnson KA**. Imaging Techniques for Small Animal Models of Pulmonary Disease: Micro-CT. *Toxicologic Pathology, 35:59-64, 2007*

[55] **Ley-Zaporozhan J, Puderbach M, Kauczor HU**. MR for the Evaluation of Obstructive Pulmonary Disease. *Magn Reson Imaging Clin N Am 16 (2008) 291-308*

[56] **Schuster DP, Kovacs A, Garbow J, Piwnica-Worms D**. Recent Advances in Imaging the Lungs of Intact Small Animals. *Am J Respir. Cell Mol. Biol., Vol. 30, pp.129-138, 2004*

[57] **Coxson HO, Mayo J, Lam S, Santyr G, Parraga G, Sin DD**. New and Current Imaging Technologies to Study Chronic Obstructive Pulmonary Disease. *Am J Respir Crit Care Med, Vol.180, pp.588-597, 2009*

[58] **Montaudon M, Berger P, Lederlin M, Marthan R, Tonon-du-Lara JM, Laurent F**. Bronchial morphometry in smokers: comparison with healthy subjects by using 3D CT. *Eur Radiol (2009) 19: 1328-1334*

[59] **Hogg JC, McDonough JE, Sanchez PG, Cooper JD, Coxson HO, Elliot WM, Naiman D, Pochettino M, Horng D, Gefter WB, Wright AC**. Micro-Computed Tomography Measurements of Peripheral Lung Pathology in Chronic Obstructive Pulmonary Disease. *Proc Am Thorac Soc, Vol.6, pp.546-549, 2009*

[60] **Sung A, Swigris J, Saleh A, Raoof S**. High-resolution chest tomography in idiopathic pulmonary fibrosis and nonspecific interstitial pneumonia: utility and challenges. *Current Opinion in Pulmonary Medicine 2007, 13:451-457*

[61] **Farncombe TH**. Software-based respiratory gating for animal conebeam CT. *Med. Phys. 35 (5), May 2008, 1785-1792*

[62] **Namati E, Chon D, Thiesse J, Hoffman EA, Ryk JD, Ross A, McLennan G.** *In vivo* micro-CT imaging via a computer-controlled intermittent iso-pressure breath hold (IIBH) technique. *Phys. Med. Biol. 51 (2006) 6061-6075*

[63] **Thiesse J, Namati E, Sieren JC, Smith AR, Reinhardt JM, Hoffman EA, McLennan G**. Lung structure phenotype variation inbred mouse strains through in vivo micro-CT. J Appl Physiol 109: 1960-1968, 2010

[64] **Ask K, Labiris R, Farkas L, Moeller A, Froese A, Farncombe T, McClelland GB, Inman M, Gauldie J, Kolb MRJ**. Comparison between conventional and "clinical" assessment of experimental lung fibrosis. *Journal of Translational Medicine 2008, 6:16*

[65] **Froese AR, Ask K, Labiris R, Farncombe T, Warburton D, Inman MD, Gauldie J, Kolb M**. Three- dimensional computed tomography imaging in an animal model of emphysema. *Eur Respir J 2007, 30: 1082-1089*

[66] **Jobse BN, Johnson JR, Farncombe TH, Labiris R, Walker TD, Concharova S, Jordana M**. Evaluation of allergic lung inflammation by computed tomography in a rat model *in vivo. Eur Respir J 2009, 33: 1437-1447*

[67] **Lederlin M, Ozier A, Montaudon M, Begueret H, Ousova O, Marthan R, Berger P, Laurent F**. Airway remodeling in a mouse asthma model assessed by in-vivo respiratory gated micro-computed tomography. *Eur Radiol (2010) 20: 128-137*

[68] **Wellman TJ, Winkler T, Costa ELV, Musch G, Harris RS, Venegas JG, Vidal Melo MF**. Measurement of Regional Specific Lung Volume Change Using Respiratory-Gated PET of Inhaled ^{13}N-Nitrogen. *J Nucl Med 2010; 51:646-653*

[69] **Vidal Melo MF, Winkler T, Harris RS, Musch G, Greene RE, Venegas JG**. Spatial Heterogeneity of Lung Perfusion Assessed with ^{13}N PET as a vascular Biomarker in Chronic Obstructive Disease. *J Nucl Med 2010; 51:57-65*

[70] **Musch G, Venegas JG**. Positron Emission Tomography Imaging of Regional Pulmonary Perfusion and Ventilation. *Proc Am Thorac Soc, Vol.2, pp522-527, 2005*

[71] **Senden TJ, Moock KH, FitzGerald J, Burch WM, Browitt RJ, Ling CD**. The Physical and Chemical Nature of Technigas. *J Nucl Med 1997; 38:1327-1333*

[72] **Meignan MA**. Lung Ventilation/Perfusion SPECT: The Right Technique for Hard Times. *J Nucl Med. Vol.43, No.5, May 2002*

[73] **Lam WW, Holdsworth DW, Du LY, Drangova M, McMormack DG, Santyr GE**. Micro-CT imaging of rat lung ventilation using continuous image acquisition during xenon gas contrast enhancement. *J Appl Physiol 103: 1848-1856, 2007*

[74] **Parraga G, Mathew L, Rezai RE, McCormack DG. Santyr GE**. Hyperpolarized ^{3}He Magnetic Resonance Imaging of Defects in Healthy Elderly Volunteers: Initial Findings at 3.0 Tesla. *Acad Radiol 2008; 15:776-785*

[75] **Shukla Y, Wheatly A, Kirby M, Svenningsen S, Farag A, Santyr GE, Paterson NA, McCormack DG, Parraga G**. Hyperpolarized 129Xe Magnetic Resonance Imaging: Tolerability in Healthy Volunteers and Subjects with Pulmonary Disease. *Acad Radiol 2012; 19:941-951*

[76] **Kirby M, Mathew L, Wheatly A, Santyr G, McCormack MD, Parraga G**. Chronic Obstructive Pulmonary Disease: Longitudinal Hyperpolarized 3HE MR Imaging. *Radiology, Vol.256, No.1, July 2010*

[77] **Harris RS, Venegas JG, Wongviriyawong G, Winkler T, Kone M, Musch G, Videl Melo MF, deProst N, Hamilos DL, Afshar R, Cho J, Luster AD, Medoff BD**. 18G-FDG Uptake Rate Is a Biomarker of Eosinophilic Inflammation and Airway Response in Asthma. *J Nucl Med 2011; 52: 1713-1720*

[78] **Schroeder T, Videl Melo MF, Venegas JG**. Analysis of 2-[Fluorine-18]-Fluoro-2-deoxy-D-glucose Uptake Kinetics in PET Studies of Pulmonary Inflammation. *Acad Radiol 2011; 18:418-423*

[79] **Wallace WE, Gupta NC, Hubbs AF, Mazza SM, Bishop HA, Keane MJ, Battelli LA, Ma J, Schleiff P**. Cis-4-[^{18}F]Fluoro-L-Proline PET Imaging of Pulmonary Fibrosis in a Rabbit Model. *J Nucl Med 2002; 43:413-420*

[80] **Foster WM, Walters DM, Longphre M, Macri K, Miller LM**. Methodology for the measurement of mucociliary function in the mouse by scintigraphy. *J Appl Physiol (2001) 90: 1111-1118*

[81] **Hislop A, Reid L**. Normal structure and dimensions of the pulmonary arteries in the rat. *J. Anat. (1978), 125, 1 pp.71-83*

[82] **Pannu HK, Thompson RE, Phelps J, Magee CA, Fishman EK**. Optimal Contrast Agents for Vascular Imaging on Computed Tomography: Iodixanol Versus Iohexol. *Acad Radiol 2005; 12:576-584*

[83] **Grabherr S, Hess A, Karolczak M, Thali MJ, Friess SD, Kalender WA, Dirnhoffer R, Djonov V**. Angiofil-Mediated Visualization of the Vascular System by Microcomputed Tomography: A Feasibility Study. *Microscopy Research and Technique 71:551-556 (2008)*

[84] **Mukundan S, Ghaghada KB, Badea CT, Kao CY, Hedlund LW, Provenzale JM, Johnson GA, Chen E, Bellamkonda RV, Annapragada A**. A Liposomal Nanoscale Contrast Agent for Precinical CT in Mice. *AJR 2006, 186, 300-307*

[85] **Ritman EL**. Micro-Computed Tomography of the Lungs and Pulmonary-Vascular System. *Proc Am Thorac Soc, Vol.2, pp.477-480, 2005*

[86] **Razavi H, Dusch MN, Zarafshar SY, Taylor CA, Feinstein JA**. A method for quantitative characterization of growth in the 3-D structure of rat pulmonary arteries. *Microvascular Research 83 (2012) 146-153*

[87] **Zhou YQ, Davidson L, Henkelman M, Nieman BJ, Foster S**. Ultrasound-guided left-ventricular catheterization: a novel method of whole mouse perfusion for microimaging. *Laboratory Investigation (2004) 84, 385-389*

[88] **Karau KL, Molthen RC, Dhyani A, Haworth ST, Hanger CC, Roerrig DL, Johnson RH, Dawson CA**. Pulmonary arterial morphometry from microfocal X-ray computed tomography. *Am J Physiol Heart Circ Physiol 281: H2747-H2756, 2001*

[89] **Molthen RC, Karau KL, Dawson CA**. Quantitative models of the rat pulmonary arterial tree morphometry applied to hypoxia-induced arterial remodeling. *J Appl Physiol 97: 2372-2384, 2004*

[90] **Shingrani R, Krenz G, Molthrn RC**. Automation process for morphometric analysis of volumetric CT data from pulmonary vasculature in rats. *Computer Methods and Programs in Biomedicine (Article in Press)*

[91] **Gierada DS, Bae KT**. Gadolineum as a CT Contrast Agent: Assessment in a Porcine Model. *Radiology 1999; 829-834*

[92] **Ritman EL**. Molecular Imaging in Small Animals-Roles for Micro-CT. *J. Cell. Biochem. Suppl. 39: 116-124, 2002*

[93] **Hsia CCW, Hyde DM, Ochs M, Weibel ER**. An Official Research Policy Statement of the American Thoracic Society/European Respiratory Society: Standards for Quantitative Assessment of Lung Structure. *Am J Respir Crit Care Med Vol 181. pp. 394-418, 2010*

[94] **Hu S, Hoffman EA, Reinhardt JM**. Automatic Lung Segmenation for Accurate Quantitation of Volumetric X-Ray CT Images. *IEEE Transactions on Medical Imaging, Vol.20, No.6, June 2001*

[95] **Sun X, Zhang H, Duan H**. 3D Computerized Segmentation of Lung Volume With Computed Tomography. *Acad Radiol 2006, 13:670-677*

[96] **Wei Q, Hu Y, Gelfand G, MacGregor JH**. Segmentation of Lung Lobes in Isotropic CT Images Using Wavelet Transformation. *Proceedings of the 29th Annual International Conference of the IEEE EMBS, August 23-26, 2007*

[97] **Prasad MN, Brown MS, Ahmad S, Abtin F, Allen J, Costa I, Kim HJ, McNitt MF, Goldin G**. Automatic Segmentation of Lung Parenchyma in the Presence of Diseases Based on Curvature of Ribs. *Acad Radiol 2008, 15:1173-1180*

[98] **Aykac D, Hoffman EA, McLennan G, Reinhardt JM**. Segmentation and Analysis of the Human Airway Tree From Three-Dimensional X-Ray CT Images. *IEEE Transactions on Medical Imaging, Vol.22, No.8, August 2003*

[99] **Fetita CI, Preteux F, Beigelman-Aubry C, Grenier P**. Pulmonary Airways: 3-D Reconstruction From Multislice CT and Clinical Investigation. *IEEE Transactions on Medical Imaging, Vol.23, No.10, November 2004*

[100] **Tschirren J, Hoffman EA, McLennan G, Sonka M**. Segmentation and Quantitative Analysis of Intrathoracic Airway Trees from Computed Tomography Images. *Proc Am Thorac Soc Vol.2, pp.484-487, 2005*

[101] **Tschirren J, Hoffman EA, McLennan G, Sonka M**. Intrathoracic Airway Trees: Segmentation and Airway Morphology Analysis from Low-Dose CT Scans. *IEEE Trans Med Imaging, 2005 December; 24(12): 1529-1539*

[102] **Shi L, Thiesse J, McLennan G, Hoffman EA, Reinhardt JM**. Three-Dimensional Murine Airway Segmentation in Micro-CT. *Proc. Of SPIE Vol. 6511, 651105, (2007)*

[103] **Cheng I, Nilufar S, Flores-Mir C, Basu A**. Airway Segmentation and Measurement in CT Images. *Proceedings of the 29th Annual International Conference of the IEEE EMBS, August 23-26, 2007*

[104] **Zheng B, Leader JK, McMurray JM, Park SC, Fuhram CR, Gur D, Sciurba FC**. Automated detection and quantitative assessment of pulmonary airways depicted on CT images. *Med. Phys. 34 (7), July 2007*

[105] **Lesage D, Angelini ED, Bloch I, Funka-Lea G**. A review of 3D vessel lumen segmentation techniques: Models, features and extraction schemes. *Medical Image Analysis 13 (2009) 819-845*

[106] **Rizi FY, Ahmadian A, Fatemizadeh E, Alirezaie J**. An Optimization Based Approach Embedded in a Fuzzy Connectivity Algorithm for Airway Tree Segmentation. *30th Annual International IEEE EMBS Conference, August 20-24, 2008*

[107] **Artaechevarria X, Perez-Martin D, Ceresa M, Biurrun G, Blanco D, Montuenga LM, Ginneken B, Ortiz-de-Solorzano C, Munoz-Barrutia A**. Airway segmentation and analysis for the study of mouse models of lung disease using micro-CT. *Phys. Med. Biol. 54 (2009) 7009-7024*

[108] **Fabijanska A**. Two-pass region growing algorithm for segmenting airway tree from MDCT chest scans. *Computerized Medical Imaging and Graphics 33 (2009) 537-546*

[109] **Pu J, Fuhrman C, Good WF, Sciurba FC, Gur D**. A Differential Geometric Approach to Automated Segmentation of Human Airway Tree. *IEEE Transactions on Medical Imaging, Vol.30, No.2, February 2011*

[110] **Palagyi K, Tschirren J, Hoffman EA, Sonka M**. Quantitative analysis of pulmonary airway tree structures. *Computers in Biology and Medicine 36 (2006) 974-996*

[111] **Yi D, Hayward V**. Skeletonization of Volumetric Angiograms for Displays. *Computer Methods in Biomechanics and Biomedical Engineering, 2002 Vol.5, (5) pp.329-341*

[112] **Al-Kofahi Y, Dowell-Mesfin N, Pace C, Slain W, Turner JN, Roysam B**. Improved Detection of Branching Points in Algorithms for Automated Neuron Tracing from 3D Confocal Images. *Cytometry Part A, 73A: 36-43, 2008*

[113] **Maddah M, Soltanian-Zadeh H, Afzali-Kusha A**. Snake modeling and distance transform approach to vascular centerline extraction and quantification. *Computerized Medical Imaging and Graphics 27 (2003) 503-512*

[114] **Sorantin E, Halmai C, Erdohelyi B, Palagyi K, Nyul LG, Olle K, Geiger B, Lindbichler F, Friedrich G, Kiesler K**. Spiral-CT-Based Assessment of Tracheal Stenoses Using 3-D-Skeleetonization. *IEEE Transactions on Medical Imaging, Vol.21, No.3, March 2002*

[115] **Jiang H, Alperin N**. A New Automatic Skeltonization Algorithm for 3D Vascular Volumes. *Proceedings of the 26th Annual International Conference of the IEEE EMBS, September 2004*

[116] **Jiang G, Gu L**. An Automatic and Fast Centerline Extraction Algorithm for Virtual Colonoscopy. *Proceedings of the 2005 IEEE Engineering and Medicine and Biology Conference, 2005*

[117] **Bates, JHT**. Lung Mechanics: An Inverse Modeling Approach. *Cambridge University Press, New York, 2009*

[118] **Weibel ER, Gomez DM**. Architecture of the Human Lung. *Science, 24 August 1963, Vol.137, No. 3530*

[119] **Phalen RF, Yeh HC, Schum GM, Raabe OG**. Application of an Idealized Model to Morphometry of the Mammalian Tracheobronchial Tree. *Anat. Rec. (1978) 190: 167-176*

[120] **Ishaq M**. A morphological study of the lungs and bronchial tree of the dog: with a suggested system of nomenclature for bronchi. *J. Anat (1980) 131, 4, 589-610*

[121] **Einstein DR, Neradilak B, Pollisar N, Minard KR, Wallis C, Fannuchi M, Carson JP, Kuprat AP, Kabilan S, Jacob RE. Corley RA**. An Automated Self-Similarity Analysis of the Pulmonary Tree of the Sprague-Dawley Rat. *Anat. Rec. (2008) 291: 1628-1648*

[122] **Lee D, Fannuchi MV, Plopper CG, Fung J, Wexler AS**. Pulmonary Architecture in the Conducting Regions of Six Rats. *Anat. Rec. (2008) 291: 916-926*

[123] **Ertbruggen CV, Hirsch C, Paiva M**. Anatomically based three-dimensional model of airways to simulate flow and particle transport using computational fluid dynamics. *J Appl Phys 98: 970-980, 2005*

[124] **Schmidt A, Zidowitz S, Kriete A, Denhard T, Krass S, Peitgen HO**. A digital reference model of the human bronchial tree. *Computerized Medical Imaging and Graphics 28 (2004) 203-211*

[125] **Gemci T, Ponyavin V, Chen Y, Chen H, Collins R**. Computational model of airflow in upper 17 generations of human respiratory tract. *Journal of Biomechanics 41 (2008) 2047-2054*

[126] **Tawhai MH, Hunter P, Tschirren J, Reinhardt J, McLennan G, Hoffman EA**. CT-based geometry analysis and finite element models of the human and ovine bronchial tree. *J Appl Physiol 97: 2310-2321, 2004*

[127] **Bates JHT**. Stochastic model of the pulmonary airway tree and its implications for bronchial responsiveness. *American Physiological Society (1993) 0161-7567/93*

[128] **Glenny RW, Robertson HT**. A computer simulation of pulmonary perfusion in three dimensions. *J Appl Physiol 79 (1): 357-369, 1995*

[129] **Venegas JG, Winkler T, Musch G, Vidal Melo MF, Layfield D, Tgavalekos N, Fischman AJ, Callahan RJ, Bellani G, Harris RS**. Self-organized patchiness in asthma as a prelude to catastrophic shifts. *Nature; April7, 2005,434,7034; pg.777*

[130] **Martonen TB, Yang Y, Dolovich M**. Definition of Airway Composition Within Gamma Camera Images. *Journal of Thoracic Imaging, 9:188-197, 1995*

[131] **Martonen TB , Yang Y, Dolovich M, Guan X**. Computer simulations of lung morphologies within planer gamma camera images. *Nuclear Medicine Communications, 1997, 18, 861-869*

[132] **Canals M, Novoa FF, Rosenmann M**. A Simple Geometrical Pattern for the Branching Distribution of the Bronchial Tree, Useful to Estimate Optimality Principles. *Acta Biotheoretica 52, 1-16, 2004*

[133] **Martonen TB, Schroeter JD, Fleming JS**. 3D In Silico Modeling of the Human Respiratory System for Inhaled Drug Delivery and Imaging Analysis. *Journal of Pharmaceutical Sciences, Vol.96, No.3, March 2007*

[134] **Schroeter JD, Pritchard JN, Hwang D, Martonen TB**. Airway Identification Within Planer Gamma Camera Images Using Computer Models of Lung Morphology. *Pharmaceuticals Research, Vol. 22, No.10, October 2005*

[135] **Tawhai MH, Burrows KS.** Developing Integrative Computational Models of Pulmonary Structure. *The Anatomical Record (Part B: New Anat.) 275B:207-218, 2003*

[136] **Burrows KS, Swan AJ, Warren NJ, Tawhai MH**. Towards a virtual lung: multi-scale, multi-physics modeling of the pulmonary system. *Phil. Trans. R. Soc. A 2008 366, 3247-3263*

[137] **Burrows KS, Hunter PJ, Tawhai MH**. Anatomically based finite element models of the human pulmonary arterial and venous tress including supernumerary vessels. *J Appl Physiol 99: 731-738, 2005*

[138] **Tawhai MH, Clark AR, Burrows KS**. Computational models of the pulmonary circulation: Insights and the move towards clinically directed studies. *Pulm Circ 2011; 1:224-38*

[139] **Tgavalekos NT, Tawhai M, Harris RS, Mush G, Vidal-Melo M, Venegas JG, Lutchen KR**. Identifying airways responsible for heterogeneous ventilation and mechanical dysfunction in asthma: an image functional modeling approach. *J Appl Physiol 99: 2388-2397, 2005*

[140] **Kitaoka H, Takaki R, Suki M**. A three-dimensional model of the human airway tree. *American Physiological Society 1999, 8750-7587/99*

[141] **Kitaoka H**. Computational morphology of the lung and its virtual imaging. *European Journal of Radiology 55 (2002) 164-171*

[142] **Garrity JM, Segars WP, Knisley SB, Tsui BMW**. Development of a Dynamic Model for the Lung Lobes and Airway Tree in the NCAT Phantom. *IEEE Transactions on Nuclear Science, Vol.50, No.3, June 2003*

[143] **Lee D, Park SS, Ban-Weiss GA, Fanucchi MV, Plopper CG, Wexler AS**. Bifurcation Model for Characterization of Pulmonary Architecture. *Anatomical Record 291:379-389*

[144] **Petre MA, Petrik J, Ellis R, Inman MD, Holloway AC, Labiris NR**. Fetal and Neonatal Exposure to Nicotine Disrupts Postnatal Lung Development in Rats: Role of VEGF and Its Receptors. *International Journal of Toxicology 30(2) 244-252, 2011*